Estimating the Short Term Variability of the Migrating Diurnal Tide through Satellite Observations

by

Vu Nguyen

A thesis submitted to the

Faculty of the Graduate School of the

University of Colorado in partial fulfillment

of the requirements for the degree of

Bachelor of Science/Master of Science

Department of Aerospace Engineering Sciences

2011

This thesis entitled:
Estimating the Short Term Variability of the Migrating Diurnal Tide through Satellite Observations
written by Vu Nguyen
has been approved for the Department of Aerospace Engineering Sciences

_____
Scott E. Palo

_____
Lynn Harvey

_____
Han-Li Liu

Date_____

The final copy of this thesis has been examined by the signatories, and we
Find that both the content and the form meet acceptable presentation standards
Of scholarly work in the above mentioned discipline.

Nguyen, Vu (B.S./M.S., Aerospace Engineering Sciences)

Estimating the Short Term Variability of the Migrating Diurnal Tide through Satellite Observations

Thesis directed by Professor Scott E. Palo

A method to explicitly estimate the short term variability of the migrating diurnal tide on a global scale is presented and analyzed. The method employs temperature data from two satellite instruments: the MLS (Microwave Limb Sounder) instrument on the EOS (Earth Observing System) Aura spacecraft and the SABER (Sounding of the Atmosphere using Broadband Emission Radiometry) instrument on the TIMED (Thermosphere Ionosphere Mesosphere Energetics and Dynamics) spacecraft. By taking advantage of the four daily solar local time measurements inherent from the two instruments, a least squares fit representing the migrating diurnal tide is constructed. Consequently, the daily zonal mean, migrating diurnal amplitude and migrating diurnal phase are all estimated on a daily basis.

The main objective of the study is to analyze the feasibility of this estimation method. A comparative analysis was first conducted that reveals biases between the two instrument data sets that are as large as 10 K. These instrument biases are removed to reduce potential error. Other error sources include the presence of other tides and waves. The effects of non-migrating tides and waves are attenuated by zonal averaging at constant solar local times. Effects of migrating tides are not attenuated by zonal averaging. The effect of the migrating semidiurnal tide, in particular, is significantly reduced by the least squares approach if the solar local time is evenly sampled. The sampling of solar local time, which changes over time due to orbit of the TIMED

satellite, displays a large influence on the results as poor sampling causes nearly linearly-dependent solutions.

The quality of the results for the diurnal amplitude and phase varies over time and geographic location. Comparisons to theory and past observation indicate that estimates are sufficient for scientific analysis near the equatorial-mesosphere where the solar local time sampling is well-spaced, the amplitude of the migrating diurnal tide is large, and the amplitudes of other tides and waves are small. A wavelet analysis for the equatorial mesosphere is performed to illustrate both the long term and short term variations of the tide.

Acknowledgments

I would like to thank my advisor, Dr. Scott Palo, for not only guiding me throughout the thesis process, but also introducing me to the wonders of research. I also wish to acknowledge the numerous professors and friends who have made my past five and a half years at CU-Boulder an unforgettable one. Finally, I am grateful for my parents for allowing me to pursue my dreams and fulfill my potential as both a student and a person.

Contents

Tables

Figures

Chapter 1

INTRODUCTION

This thesis will introduce and analyze the feasibility and scientific validity of a method originally implemented by *Palo et al.* [2008] to estimate the migrating diurnal tide from daily satellite observations. If deemed practicable, the method could be applied to explicitly estimate the short term variability of the migrating diurnal tide on a global scale for the first time.

1.1 Atmospheric Tides

Periodic responses by the atmosphere to various forcing mechanisms occur on a comprehensive range of spatial and temporal scales. Atmospheric tides are one type of response. They are mainly forced by solar absorption, but also by latent heat release due to deep convection in the tropics, nonlinear interactions between global-scale waves, and interaction between gravity waves and tides [*Hagan et al.*, 2002]. These responses are observed as global scale oscillations of atmospheric field variables (temperature, wind, pressure, density, etc.) with periods that are harmonics of a solar day. Atmospheric tides originate in the lower parts of the atmosphere where solar energy absorption takes place. Some of these tides propagate upward through the atmosphere transferring energy along the way. As the density of the atmosphere decreases with height, energy is conserved and the tidal amplitude increases as a result**.** The amplitudes reach a maximum in the lower thermosphere where they are damped by turbulent

diffusion from breaking gravity waves, increasing molecular diffusion and other wave-mean flow interactions [*Hagan et al.*, 1995; *Tsuda et al.*, 1999].

Although tides and other waves can travel upward through the atmosphere, they are most easily classified based on how they propagate through horizontal space and time. The quantity of an atmospheric field variable, f, can be decomposed into a zonal mean (average across all longitudes) and a perturbation where λ is longitude, ϕ is latitude, z is altitude and t is time:

$$f(\lambda, \phi, z, t) = \bar{f}(\phi, z, t) + f'(\lambda, \phi, z, t) \quad 1.1$$

The perturbation variable, f', is described as a sum of oscillatory waves that propagate through time in the zonal direction with frequency (σ) and wave number (s). In this context, wave number can be defined as the number of crests along a latitude circle. Oscillations with frequencies that are harmonics of a solar day are denoted tides while other large scale oscillations are generally classified as planetary waves [*Forbes*, 1995]. The perturbation about a zonal mean can be viewed as a summation of all tides and planetary waves with various wave numbers and frequencies. It can be written in the form displayed in equation 1.2 where A(ϕ,z) is the tidal amplitude and θ(ϕ,z) is the tidal phase.

$$f'(\lambda, \phi, z, t) = \sum_k \sum_i A_{s,\sigma}(\phi, z) \cos\left(s_k \lambda - \sigma t + \theta_{s,\sigma}(\phi, z)\right) \quad 1.2$$

As shown in the equation, atmospheric tides and planetary waves can propagate to the west ($\sigma < 0$), east ($\sigma > 0$) or remain standing ($s = 0$) with frequencies expressed as fractions of a solar day and wave numbers. The amplitude and phase of tides and planetary waves are only dependent on altitude and latitude in this form and hence, have a vertical and horizontal structure.

Migrating tides are those components that propagate with the apparent westward motion of the sun and have periods that are harmonics of a solar day. Normalized frequency is often

utilized to simplify analysis and is defined as σ/Ω where Ω is the rotation rate of the earth. Thus, migrating tides possess a normalized frequency that is negative and a magnitude that is equal to the wave number ($|\sigma/\Omega| = s$). All other tides are labeled as non-migrating. The largest tidal component below the thermosphere is the migrating diurnal tide (MDT), which has a wave number equal to one, a period of 24 hours ($\sigma/\Omega = -1$) and is primarily forced by solar absorption by water vapor in the troposphere. It is also the most dominant feature of the mesosphere-lower thermosphere (MLT) region at low to mid-latitudes [*Burrage et al.*, 1995]

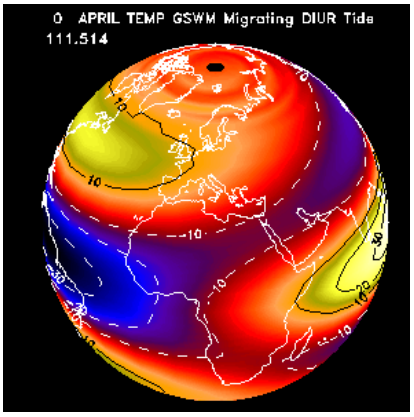

Figure 1.1: Global structure of the migrating diurnal tide at 110 km taken from the Global Scale Wave Model [*Hagan et al.*, 1993]. It is observed that, for a given latitude circle, there is one perturbation crest and one perturbation trough with respect to the zonal mean.

Because of its persistence and dominance, the MDT assumes an important role in governing the dynamics of the poorly understood MLT region. The MLT region lies at an altitude range where in-situ measurements are difficult to perform; it is too high for weather balloons and aircraft to reach and below the minimum altitude for most earth-orbiting spacecraft. Most analyses of the MLT region instead rely on ground-based radar systems or satellite remote sensing instruments, which makes observations slightly more difficult. The MLT region serves as a transition region between the lower atmosphere where ideal gas dynamics dominate and the

upper atmosphere governed by molecular diffusion. Studies of the MLT are therefore crucial to discerning the coupling between two fundamentally different layers of the atmosphere. In order to enhance our understanding of the MLT region, the most dominant feature of the region, the MDT, must be properly characterized.

The MDT has been studied extensively from ground-based systems and satellite-based instruments. There are benefits and drawbacks for both observation techniques. Ground-based systems such as radar and lidar can monitor a particular region of the atmosphere for long continuous intervals, which leads to tidal and wave estimates of high time resolution. The main disadvantage of ground-based systems is the lack of spatial coverage. As a result, the latitudinal and longitudinal dependencies cannot be determined. Coordinated studies between radar systems placed around globe have been performed in the past to provide more information on the spatial structure.

In contrast, satellite-based instruments observe the atmosphere over a wide range of latitude and longitude, which yields detailed information on the spatial structure of the tides. The main weakness of analyzing atmospheric tides through satellite instrument data is the inability to view the entire global structure over a continuous time interval. In order to distinguish tides and waves from each other and explicitly estimate the features of each, the spatial structure must be observed over a sufficient range of solar local times. Satellites such as TIMED are in orbits that cover a diurnal range of solar local time in a fixed amount of universal time, which allows for the temporal characteristics of the tides to be extracted. However, due to the amount of time required for full diurnal coverage (60 days for TIMED), the time resolution of the estimates is very low.

Past observational studies have shown that the features of the MDT exhibit variation on a manifold of time scales. Ground-based observations have been utilized to study the short term and long term trends of the MDT at particular locations on the globe. More recently, satellite-

borne instruments have been used to determine the long term variations of the MDT. However, explicit estimations of the short term variability on a global scale have been nonexistent because of the limitations of full solar local time coverage inherent from using data from one satellite instrument.

1.2 Objectives

A new method for explicitly estimating the short term variability of the MDT is presented in this paper. It is proposed that the features of the MDT can be determined on a daily basis by utilizing one instrument on a satellite that precesses through a full diurnal range of solar local time and another instrument on a satellite that is placed in a sun-synchronous orbit [*Palo et al.*, 2008]. The two chosen satellite instruments are SABER (Sounding of the Atmosphere using Broadband Emission Radiometry) on the TIMED (Thermosphere Ionosphere Mesosphere Energetics and Dynamics) satellite and MLS (Microwave Limb Sounder) on the EOS (Earth Observing System) Aura satellite. Both instruments measure temperature profiles of the atmosphere from the lower stratosphere to the lower thermosphere. By combining data from instruments in different orbits, the temporal limitations of analyzing tides from satellite platform can be reduced.

The main objective of this study is to analyze the effectiveness and feasibility of using measurements from the TIMED-SABER and EOS Aura-MLS satellite instruments to estimate the short term variation of the MDT. The study strives to answer the following questions:

(1) Can this method reliably determine features of the MDT on a daily basis?

(2) What factors dictate the effectiveness of this method and what are its limitations?

Although a discussion on the short term variability of the MDT is provided, the objective of this paper is not to analyze the variability and the possible processes involved. A more detailed analysis on this subject is a long term objective of this research and will hopefully be provided in the future. This thesis will focus primarily on the analysis technique.

Chapter 2

BACKGROUND

The following chapter will first provide an overview of classical tidal theory and the results that pertain to the MDT. The second portion of the chapter will summarize past observations of the MDT including its features and the methods for estimation. Overall, the chapter will present the necessary background to understand the theoretical and observed features of the MDT and how it is estimated from various data sources.

2.1 Tidal Theory

2.1.1 Governing Equations and Assumptions

The theory behind large scale atmospheric motion has been presented numerous times throughout the past century. One of the more often-cited works is *Chapman and Lindzen* [1970], which provides an overview of the history of tides and comprehensively describes the classical theory. For this paper, however, the derivation of the linearized governing equations explained by *Palo* [1994] (based on *Holton* [1975]) and the classical theory presented by *Forbes* [1995] will be summarized because the theoretical concepts and results most closely pertain to the interests of this paper.

Atmospheric motion is governed by the fundamental principles of momentum, mass and energy conservation. These principles in a rotating Cartesian coordinate system can be expressed in its most primitive form by the following equations:

$$\frac{D}{Dt}\boldsymbol{U} = -2\Omega\, x\, \boldsymbol{U} - \frac{1}{\rho}\nabla p + g + F_r = 0 \tag{2.1}$$

$$\frac{D}{Dt}e = J - \frac{p}{\rho}(\nabla \cdot \boldsymbol{U}) \tag{2.2}$$

$$\frac{\partial}{\partial t}\rho + \frac{\partial}{\partial x}(\rho u) + \frac{\partial}{\partial y}(\rho v) + \frac{\partial}{\partial x}(\rho w) = 0 \tag{2.3}$$

Equation 2.1 describes the conservation of momentum where **U** denotes the velocity in the x, y, and z directions. The conservation of momentum is merely another form of Newton's second law for a unit mass. In this case, it states that for a unit mass in a rotating frame, the acceleration is equal to the sum of the apparent Coriolis force ($-2\Omega \times \mathbf{U}$), pressure gradient force ($-\nabla p/\rho$), effective gravitational force (g), and frictional force (F_r). The second equation is an expression of the conservation of energy, which states that the change in internal energy (De/Dt) is equal to the heat rate entering the system (J) minus the work rate done by the system ($p/\rho(\nabla\cdot\mathbf{U})$). The conservation of mass is described by the third equation, which is commonly known as the continuity equation. It states that the density convergence into a system must equal the time rate of change of density.

The equations representing the conservation principles must be placed into a form that can be used to evaluate the behavior of perturbations on an atmospheric zonal mean. The following description is a brief summary of the process presented by *Palo* [1994]. Equations 2.1-2.3 are first placed into a spherical coordinate system by assuming the atmosphere is an ideal gas that behaves like a thin fluid on the surface of the earth. Additionally, frictional forces are assumed to be negligible. The resulting equations are then transformed into an isobaric

coordinate system with pressure replacing geometric height as the vertical coordinate by assuming the atmosphere is in hydrostatic equilibrium. The hydrostatic assumption introduces geopotential, Φ, which is defined as the amount of work needed to raise a mass of 1 kg from the surface to an arbitrary height. The isobaric system is then converted to a log-pressure coordinate system where the new vertical height is defined by:

$$z = \frac{R_d T}{g} ln\left(\frac{p}{p_s}\right) = \frac{\Phi}{g} \tag{2.4}$$

Equation 2.4 is the hypsometric equation, which assumes a dry, isothermal atmosphere with a temperature (T) of 256 K, a surface pressure (p_s) of 1013 mb and a constant acceleration due to gravity. The set of equations in spherical, log-pressure coordinates can be separated into one set of equations describing zonally averaged motions and a second set of equations describing perturbations. To perform this step, each atmospheric field variable (u, v, w, Φ, J) is decomposed into a zonal mean term and a perturbation term (equation 1.1). Once the sets of equations describing the zonal mean and perturbation are obtained, two final assumptions are made: the mean zonal flow is zero for the perturbation equations and the perturbation quantities are small. The assumptions allow for the linearized, equations governing the dynamics of the perturbation quantities (denoted by tick marks) to be established as:

$$\frac{\partial u'}{\partial t} - 2\Omega sin\theta v' + \frac{1}{acos\theta}\frac{\partial \Phi'}{\partial \lambda} = 0 \tag{2.5}$$

$$\frac{\partial v'}{\partial t} + 2\Omega sin\theta u' + \frac{1}{a}\frac{\partial \Phi'}{\partial \theta} = 0 \tag{2.6}$$

$$\frac{\partial}{\partial t}\left(\frac{\partial \Phi'}{\partial z}\right) + N^2 w' = \frac{\kappa J'}{H} \tag{2.7}$$

$$\frac{1}{acos\theta}\left[\frac{\partial u'}{\partial \lambda} + \frac{\partial}{\partial \theta}(v' cos\theta)\right] + \frac{1}{\rho}\frac{\partial}{\partial z}(\rho w') = 0 \tag{2.8}$$

To summarize, these equations are derived from the principles of mass, energy and momentum conservation. The atmosphere is assumed to be a thin layer of inviscid fluid on top of the earth and approximated by the ideal gas and hydrostatic laws. It is also assumed to be dry, isothermal, windless (no mean flow) and perturbed by small quantities.

2.1.2 Solving the Governing Equations

The process for solving the linearized governing equations (equations 2.5-2.8) is presented here. Details are provided in Appendix C.

Solutions to the linearized equations governing the perturbation quantities are assumed to be periodic in longitude and time. The assumption is established because the linearized equations are driven by heating from solar radiation. Since heating from solar radiation is periodic in time and longitude, the solutions should also be expected to behave in the same manner. The solutions are assumed to take following form:

$$u'(t,\lambda,\theta,z) = \sum_{s}\sum_{\sigma} \hat{u}_{\sigma,s}\, e^{[i(s\lambda-\sigma t)]} \tag{2.9}$$

$$v'(t,\lambda,\theta,z) = \sum_{s}\sum_{\sigma} \hat{v}_{\sigma,s}\, e^{[i(s\lambda-\sigma t)]} \tag{2.10}$$

$$w'(t,\lambda,\theta,z) = \sum_{s}\sum_{\sigma} \hat{w}_{\sigma,s}\, e^{[i(s\lambda-\sigma t)]} \tag{2.11}$$

$$\Phi'(t,\lambda,\theta,z) = \sum_{s}\sum_{\sigma} \hat{\Phi}_{\sigma,s}\, e^{[i(s\lambda-\sigma t)]} \tag{2.12}$$

$$J'(t,\lambda,\theta,z) = \sum_{s}\sum_{\sigma} \hat{J}_{\sigma,s}\, e^{[i(s\lambda-\sigma t)]} \tag{2.13}$$

Although the linearized system of equations can be used to solve for other perturbation quantities, temperature and consequently, Φ', is the variable of interest. Geopotential, Φ, is related to temperature by the hypsometric equation (equation 2.4). A single, independent

expression relating Φ' to the forcing function, J', can be derived from the system of equations because it contains four equations and four unknown perturbation variables. The expression for Φ' is a second-order partial differential equation with respect to latitude (θ) and height (z). In order to solve the equation for Φ' for a given s and σ, method of separation of variables is utilized. The solution for Φ' is assumed to be separable in latitude and height and in the form shown in equation 2.14.

$$\Phi' = \widehat{\Phi}_{\sigma,s} e^{[i(s\lambda-\sigma t)]} = \left[\sum_n \Theta_n(\theta) G_n(z)\right] e^{[i(s\lambda-\sigma t)]} \quad 2.14$$

The heating per unit mass, J, that appears in the second-order differential equation is also a function of θ and z and must also be separable in order to proceed. Fortunately, the Hough functions ($\Theta_n(\theta)$) form a complete orthogonal set of eigenfunctions and are used to separate J. An expression for J' is shown in equation 2.15.

$$J' = \hat{J} e^{[i(s\lambda-\sigma t)]} = \left[\sum_n \Theta_n(\theta) J_n(z)\right] e^{[i(s\lambda-\sigma t)]} \quad 2.15$$

By substituting the assumed solutions for J' and Φ' into the second-order partial differential equation and establishing a separation constant of $-i\sigma\kappa/h_n$, two differential equations are obtained as shown in equations 2.16 and 2.17. Equation 2.16 is known as the vertical structure equation while equation 2.17 is Laplace's tidal equation.

$$\frac{d^2 G'_n}{dx^2} + \left[\frac{\kappa H}{h_n} - \frac{1}{4}\right] G'_n = -\frac{\rho^{-1/2}}{i\sigma N}\frac{d}{dx}(\rho J_n) \quad 2.16$$

$$\frac{d}{d\mu}\left[\frac{(1-\mu^2}{(f^2-\mu^2)}\frac{d\Theta_n}{d\mu}\right] - \frac{1}{f^2-\mu^2}\left[-\frac{s}{f}\frac{(f^2+\mu^2)}{(f^2-\mu^2)} + \frac{s^2}{1-\mu^2}\right]\Theta_n + \epsilon\Theta_n = 0 \quad 2.17$$

where $G = \frac{G_n \rho^{1/2}}{N}$, $x = \frac{z}{H}$, $f = 2\Omega sin\theta$, and $\mu = sin\theta$

Each solution to Laplace's tidal equation describing the latitudinal dependencies of each perturbation quantity will be an eigenvalue (ϵ_n)-eigenvector (θ_n) pair. The eigenvectors that satisfy Laplace's tidal equation are known as Hough functions and form a complete orthogonal set of solutions. Hence, the exhaustive solution to Laplace's tidal equation for a given s and σ is the superposition of all Hough functions. Solutions to the vertical-dependent part of Φ' are determined by solving for the density weighted function of G'(z) in the vertical structure equation. The vertical structure equation is related to Laplace's tidal equation by the separation constant. Consequently, each eigenvalue-eigenvector pair obtained by solving Laplace's tidal equation is associated with a G'_n solution from the vertical structure equation. The full solution for the perturbation quantity, Φ', is the summation of the product of all (θ_n, G_n') pairs as shown in equation 2.14.

To solve the second-order, ordinary differential equations, certain boundary conditions must be established. For the vertical structure equation, the solution must be bounded at the upper boundary of the atmosphere and the vertical velocity is zero at the surface. Solutions to Laplace's equation are also bounded at the poles.

$$\lim_{x\to\infty} G'_n < \infty \tag{2.18}$$

$$w = \frac{\partial}{\partial t}\left(\frac{\partial}{\partial x}\Phi - \frac{N^2}{g}\Phi\right) = 0 \tag{2.19}$$

$$\lim_{\mu\to -1\ or\ 1} \Theta_n < \infty \tag{2.20}$$

2.1.3 Tidal Solutions

The vertical structure equation may be rewritten in terms of a forcing function, F(x), containing the heating term, J', by the following equation.

$$\frac{d^2G'_n}{dx^2} + \alpha^2 G'_n = F(x) \qquad 2.21$$

where $\alpha^2 = \frac{\kappa H}{h_n} - \frac{1}{4}$

Solutions to the equation can either be free (F(x) = 0) or forced (F(x) ≠ 0). By applying the aforementioned boundary conditions and setting F(x) to zero, the free solutions describing the resonant response of the model atmosphere can be determined. These free solutions are often denoted as normal modes and yield the following form:

$$G'_n \sim e^{\left(\kappa - \frac{1}{2}\right)x} \qquad 2.22$$

Since $\kappa < ½$, the normal modes will decay as the wave propagates upward. Furthermore, the form of the solution and the definition of α^2 imply that h_n contained in the separation constant is equal to 10.5 km for these unforced modes.

The behavior of the forced solutions to the vertical structure equation is dependent on the sign of α^2. If $\alpha^2 < 0$ ($h_n < 0$ or $h_n > 4\kappa H$), then the solution yields the following form:

$$G'_n \sim e^{-|\alpha|x} \qquad 2.23$$

The form indicates a bounded solution, which means the mode will not propagate far from the region of excitation. If $\alpha^2 > 0$ ($0 < h_n < 4\kappa H$), then the solution will propagate away from the region of excitation with vertical wavelength, $2\pi/\alpha$, and have the form:

$$G'_n \sim e^{i\alpha x} \qquad 2.24$$

Furthermore, from the vertical boundary conditions and the assumed form of the horizontal propagating solutions, it is shown in *Forbes* [1995] that these propagating waves have a downward phase velocity and upward energy propagation.

As explained previously, for a chosen s and σ, there are pairs of ϵ_n and Θ_n that form solutions to Laplace's tidal equation and its boundary conditions. The index (n) is referred to as a mode of the solution for given wave number (s) and frequency (σ). Therefore, there is an eigenvalue-eigenvector dependence on wave frequency, wave number, and mode. Figure 2.1 shows the dependence of the eigenvalues on wave period and mode for wave number, s = 1.

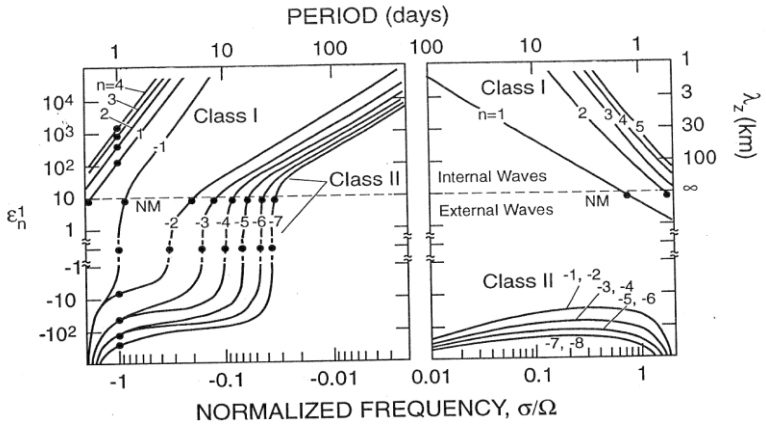

Figure 2.1: Eigenvalues (ε_n) of wave modes vs. normalized frequency for s = 1 [*Forbes*, 1995]. The vertical series of dots at σ/Ω=-1 corresponds to the eigenvalues of each mode for the migrating diurnal tide. The vertical wavelength (λ_z) of each wave mode is displayed on the right vertical axis.

The eigenvalues for each mode of the diurnal tide are denoted by the vertical string of dots from the 1-day wave period in the figure. Modes with eigenvalues less than about 8.5 km are trapped within the region of excitation and do not propagate since $\alpha^2 < 0$. If the eigenvalues are greater than 8.5 km ($\alpha^2 > 0$), then the respective modes will propagate upwards through the atmosphere. As a result, all positive modes of the MDT propagate through the atmosphere while all negative modes are trapped. Out of all the propagating modes, the first mode is the most dominant in the middle and upper atmosphere due to the forcing nature of troposphere absorption and the dissipation of shorter wavelength modes [*Forbes*, 1995]. The vertical wavelength of each

mode is derived from the eigenvalue because it is only dependent on the value of α. A table containing the vertical wavelengths of the first three modes of the MDT is shown in Table 2.1. As in *Forbes* [1995], the mode of a migrating or non-migrating tide of a given frequency is often denoted by wave number and mode index, (s, n).

Mode (s,n)	**Vertical Wavelength (λ_n)**
(1,1)	27.9 km
(1,2)	15.9 km
(1,3)	11.2 km

Table 2.1: Vertical wavelengths of first 3 modes of the MDT

Each eigenvalue and thus, each mode are associated with a specific Hough function (Θ_n), which describes the latitudinal dependency of the tidal solution. The Θ_n functions for the (1,1), (1,2), (1,-1), (1,-2) and (1,-2) modes are displayed in Figure 2.2.

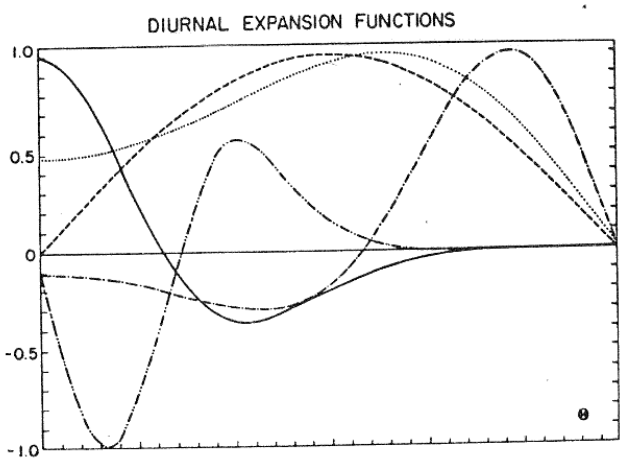

Figure 2.2: Hough functions for several modes of the MDT [*Forbes*, 1995]. The expansion functions are normalized to 1 and displayed on the y-axis. Latitude is on the x-axis. The first two propagating modes are represented as solid (1,1) and dashed-double-dot lines (1,2). The trapped modes are seen as dashed (1,-1), dot (1,-2) and dashed-dot (1,-4).

As shown in the figure, the first propagating mode (1,1) is concentrated near the low latitudes, displaying a large peak at the equator and a smaller peak at about 30°. The second propagating mode and other trapped modes are concentrated at higher latitudes. Since the (1,1) is most dominant, the MDT should display large amplitudes at the equator given a sufficiently high altitudes.

2.1.4 Classical Theory Limitations

Because of the assumptions involved in the classical tidal theory, the obtained solutions are approximations to the tides observed in reality. In the real atmosphere, the effects of mean winds, temperature and dissipation processes are relevant [*Andrews*, 1987]. Dissipation processes such as Newtonian cooling, molecular viscosity, thermal conductivity and ion drag are important because they serve to damp the tides, particularly in the MLT region. The effects of nonlinear interactions with other atmospheric waves, which are inherent through the nonlinear terms in the momentum equations are also ignored in classical theory, but must be accounted for in a real atmosphere. Further characterization of the wave forcing mechanisms such as solar absorption, latent heat release, and localized excitation sources is also necessary to improving theory.

Numerical models such as the Global Scale Wave Model (GWSM) have extended the classical theory by implementing many of these real atmospheric processes [*Hagan et al.*, 1993]. The inclusion of real atmospheric parameters have improved models to a point where they agree with observations fairly well. However, there are a countless number of atmospheric processes that are not fully understood and can affect atmospheric tides in unknown ways. Observations of the tides and other waves are therefore instrumental in improving the theoretical results and our general understanding of atmospheric dynamics.

2.2 Tidal Observations

2.2.1 Past Observations of the Migrating Diurnal Tide

The MDT has been extensively studied from both ground and space, resulting in many discoveries. One feature of the MDT that differs from classical tidal theory is hemispheric asymmetry. Classical tidal theory predicts that the (1,1) mode dominates the features of the migrating diurnal tide. Tidal theory predicts large amplitudes at the equator and slightly smaller amplitudes at around ±30° latitude. The (1,1) mode is also symmetric in latitude although coordinated ground-based observations have revealed larger amplitudes in the southern hemisphere [*Vincent et al.,* 1988]. One possible explanation for the hemispheric asymmetry is the difference in turbulent dissipation [*Tsuda et al.,* 1999].

Observations of the MDT vertical structure have been performed and features such as the vertical wavelength have been estimated. Various studies from the ground and space have measured the vertical wavelength to be ~20-25 km at the equatorial mesosphere [*Oberheide and Gusev*, 2002; *Deepa et al.*, 2006; *Zhang et al.,* 2006; *Mukhtarov et al.*, 2009; *Xu et al.*, 2009]. The observed vertical wavelengths are smaller than the vertical wavelength of 27.9 km predicted by the (1,1) Hough mode. Several factors can explain the differences between the observed vertical wavelengths and theory. Other propagating modes of the MDT that are characterized by shorter wavelengths than the (1,1) Hough mode can be present to affect the estimates. Additionally, theoretical assumptions such as zero mean winds and an isothermal atmosphere are not valid in a real atmosphere. The presence of mean winds can cause the migrating diurnal tide to assume shorter or longer vertical wavelengths through Doppler shifting [*Forbes and Hagan*, 1988]. For a non-isothermal atmosphere, the α^2 term in the vertical structure equation (equation 2.21) becomes the following [*Lindzen and Blake*, 1972]:

$$\alpha^2 = \frac{\kappa H + \frac{dH}{dx}}{h_n} - \frac{1}{4} \quad 2.25$$

The additional dH/dx term in equation 2.25 that accounts for the change in scale height with altitude. Since the vertical wavelength is equal to $2\pi/\alpha$, the vertical wavelength also has a dependence on altitude.

Observations have also shown that the amplitudes of the migrating diurnal tide vary on timescales ranging from days to years [*Lieberman et al.*, 2007]. The most notable long term variations of the diurnal tide are the semiannual, annual and quasi-biennial periodicities. The semiannual variation of the diurnal tide has been observed to exhibit maxima during the equinoxes and minima at the solstices [*Burrage et al.*, 1995]. Seasonal variations in solar heating may explain the seasonal oscillation [*McLandress*, 2002]. Possible sources of the semiannual periodicity include variations in eddy viscosity and seasonal variations of the zonal mean winds [*Mayr et al.*, 2005]. The annual and quasi-biennial variations in the diurnal tide have been extensively studied recently through satellite data [*Huang et al.*, 2009; *Muktharov et al.*, 2009; *Xu et al.*, 2009] although the sources of the periodicities have not been successfully explained. Numerical studies have suggested that annual and interannual oscillations in the background wind may modulate the diurnal tide through advection, particularly in the MLT region [*Hagan et al.*, 1999; *McLandress*, 2002].

Short term variations of the MDT have been estimated and studied from a variety of sources. *Pancheva et al.* [2002] observed through a coordinated radar experiment that tides displayed specific short term periodicities. This suggested that the tides were interacting with planetary waves through nonlinear advection of energy and were being modulated by the planetary wave period. Numerical studies have backed this claim, but have also concluded that tidal amplitude modulation can also occur due to interaction with the background winds and

gravity waves [*Lieberman et al*., 2007]. Daily estimates of the MDT have also been produced from satellite instrument data. However, the results were not determined explicitly and instead assumed a (1,1) Hough mode latitudinal structure and an amplitude growth envelope [*Burrage et al.,* 1995; *Hays et al.,* 1994]. Estimates for the (1,1) component of the MDT obtained from a Hough mode analysis on satellite wind data [*Burrage et al.,* 1995] are displayed Figure 2.3. The results provide evidence that both short term and long term variations in the MDT exist.

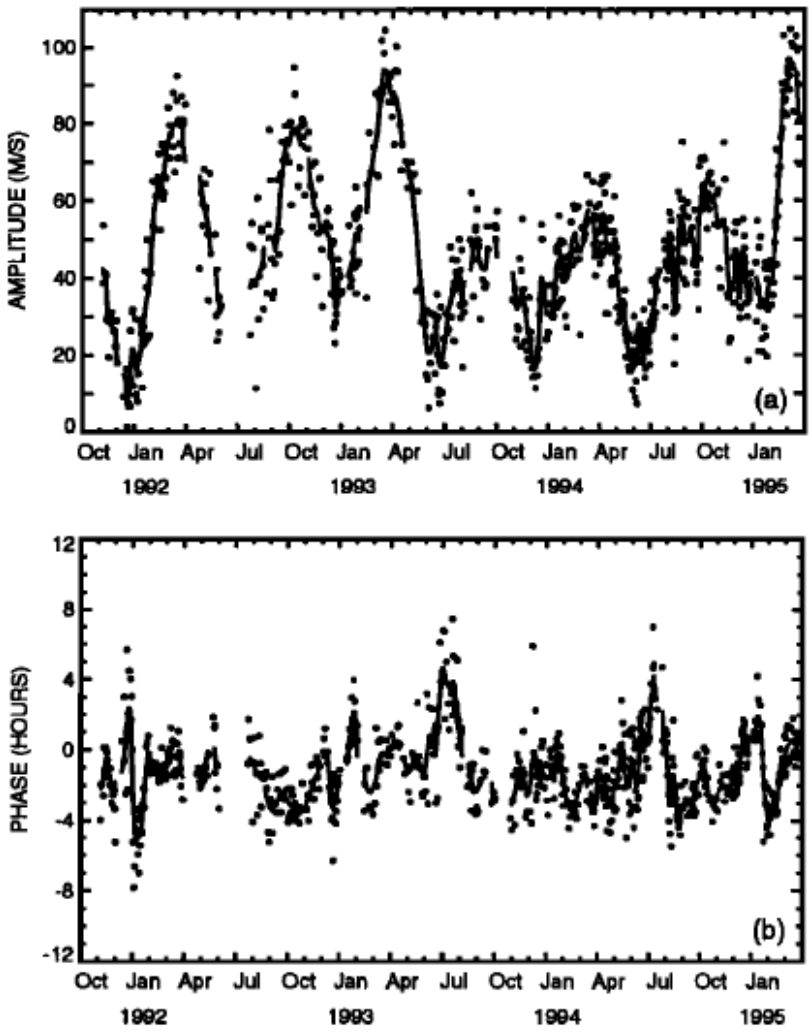

Figure 2.3: Daily estimates of the (1, 1) component of the MDT at 20° latitude and 95 km from Hough mode analysis [*Burrage et al.,* 1995]. Estimates were derived from wind observations from the HRDI instrument on the UARS satellite.

2.2.2 Methods of Observing Atmospheric Tides

Atmospheric tides and planetary waves are observed primarily by monitoring temperature or wind velocity over a range of altitude, latitude, longitude and time. Although tidal estimates have been accommodated by in-situ rocket measurements in the past [*Reed et. al*., 1969], more recent techniques have relied on ground-based or satellite instrument observations. Ground-based atmospheric monitoring has been achieved by a diverse group of instrumentation. Each system has its own set of advantages and drawbacks. Continuous horizontal wind measurements between 70 km and 100 km are often made by medium frequency radar and meteor wind radars [*Tsuda et al.*, 1999]. Incoherent scatter radars have the capability of providing temperature and wind measurements at higher altitudes, but do not provide data over long term continuous intervals and are only available at specific sites around the globe [*Zhang et al.*, 2006]. Increasingly more common are lidars, which are wielded to measure wind and temperature over a larger altitude range and higher vertical resolution, but are limited in location [*Zhang et al*., 2006; *Chang*, 2010]. Passive optical methods are also employed to measure temperature, but are limited to a small altitude range and night time observations.

One of the foremost benefits of ground-based methods is the ability to produce data at a specific location over a 24 hour interval. Consequently, waves with varying frequency can easily be distinguished from another. Furthermore, the variability of the tides can be characterized over short time intervals. Ground-based techniques, however, are limited in spatial coverage and do not have the ability to distinguish between waves with identical frequency, but different wave number [*Chang*, 2010]. These disadvantages have been ameliorated over the years by coordinating radar systems at different locations around the globe [*Vincent et al.*, 1988; *Tsuda et*

al., 1999; *Pancheva et al.*, 2002], though the spatial resolution of the wave measurements is still coarse.

In recent years, temperature and wind measurements from satellite instruments have been utilized to measure atmospheric tides and waves. The Upper Atmosphere Research Satellite (UARS) was launched in 1991 and provided one of the earliest opportunities to accurately and explicitly estimate tides and waves from orbit. Instruments such as the Microwave Limb Sounder (MLS) and the High Resolution Doppler Imager (HRDI) measured temperature and wind velocity over a wide range of altitude, latitude and longitude and hence, provided superior spatial coverage when compared to ground-based methods. The main disadvantage of utilizing satellite-derived data is the limited local time coverage. In order to explicitly estimate the features of atmospheric tides, data over a full range of solar local time at a particular location on the earth must be obtained. The reasons for this are presented in the next section. The UARS satellite needed 36 days to cover 24 hours of solar local time, which meant the derived tidal estimates only represented 36-day averages.

With the end of the UARS mission in 2005, more scientists studying atmospheric tides and waves turned to the TIMED satellite for upper atmospheric data. Similar to UARS, TIMED slowly covers a diurnal solar local time range (60 day period) to allow for adequate atmospheric wave estimates. Over the past decade, a variety of techniques have been utilized to explicitly extract tide and wave information from temperatures specifically measured by the SABER instrument on TIMED. Some of these methods are briefly summarized and discussed in the following section.

2.2.3 Extracting Tides and Waves from Satellite Data

Because atmospheric tides and planetary waves propagate along latitude circles with time, both the spatial and temporal characteristics of the tides must be characterized. Satellite-borne instruments in low earth orbit cover a full longitudinal range in a solar day, which provides information on the global structure of tides and waves. However, the satellite instruments cannot observe the entire global structure at a single point in time and thus the temporal characteristics must be inferred indirectly. To estimate the amplitude and phase of a particular wave, enough wave points (phases) must be sampled. Additionally, the evolution of the phases with respect to longitude and time must be known to a certain degree for waves with differing wave numbers and frequencies to be distinguished from one another.

Because atmospheric tides originate from thermal heating from the Sun, the concept of solar local time is introduced to describe the time dependence of the tides and waves. Furthermore, solar local time can be utilized to extract tidal information from observations. The solar local time at a location is defined by the angle between the vector from the center of the earth to the given location and the vector from the center of the earth to the Sun. Its relation to universal time is:

$$t_{LT} = t + \frac{\lambda}{\Omega} \tag{2.26}$$

Thus, a perturbation quantity consisting of a summation of tides and waves may be re-written in terms of solar local time as the time coordinate:

$$\mathrm{f}'(\lambda, \phi, \mathrm{z}, \mathrm{t}) = \sum_k \sum_i A_{s,\sigma}(\phi, z)\cos\left(s_k\lambda - \sigma_i t + \theta_{s,\sigma}(\phi, z)\right) \tag{2.27}$$

$$\mathrm{f}'(\lambda, \phi, \mathrm{z}, \mathrm{t}) = \sum_k \sum_i A_{s,\sigma}(\phi, z)\cos\left((s_k + \frac{\sigma}{\Omega})\lambda - \sigma_i t_{LT} + \theta_{s,\sigma}(\phi, z)\right) \tag{2.28}$$

The entire global structure of the temperature field can now be viewed over a continuous temporal range by sampling over a full range of longitude and solar local time. As a result, it is possible to extract both the temporal and spatial characteristics of the perturbation field. Features of particular tides and waves can now be extracted.

Sun-synchronous orbits observe the atmosphere at two local times per day at a given latitude, which is not enough to accurately estimate the features of migrating tides. It should be noted that instruments in sun-synchronous orbits have been used to estimate planetary waves with periods longer than a solar day by incorporating data over a long time interval to minimize aliasing [*McDonald et al.*, 2010]. These techniques take advantage of the fact the wave phase is not constant at a given solar local time. Enough information about the planetary wave structure is extracted by sampling over multiple orbits at two solar local times. In contrast, the wave phase is constant for a given solar local time for migrating waves ($s = -|\sigma/\Omega|$) because the tides travel at the apparent motion of the Sun. Sampling at two solar local times per day at a given latitude does not provide enough information to extract migrating tides because measurements are essentially provided at only two wave phases.

The sampling of the MDT by a satellite in a sun-synchronous orbit is illustrated in Figure 2.4. Lines of constant color indicate constant phase points. It is shown that the same wave phase is sampled every orbit because the ground track moves at the same rate as the apparent motion of the Sun. The benefit of utilizing instruments in orbits that cover a diurnal range of solar local times in a short time span is that all phases of the migrating tides sampled, which allows for wave extraction.

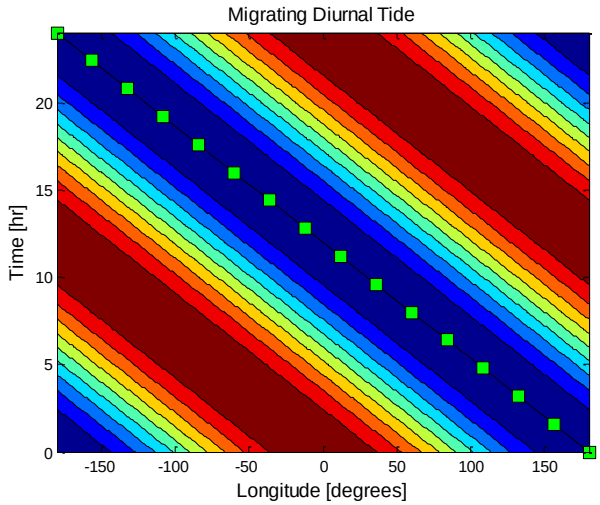

Figure 2.4: Sampling of the MDT from a satellite in sun-synchronous orbit. Colors represent the phase of the migrating diurnal tide. The green dots represent the sampling of the tide over 15 orbits.

The TIMED satellite is placed in an orbit that allows it to cover a diurnal range of solar local times at a given location on the earth in 60 days, which is slow compared to ground observations. Although this orbit allows for the extraction of atmospheric tides, there are several potential difficulties that arise from the slow precession rate. One issue is that the estimates of the tidal components from the data only represent averages over 60 days and do not exhibit short term variability. Another problem is the potential for the zonal mean to alias into the tides. Any changes in the zonal mean with time during the 60 day period will be perceived as a change due to local time change and will affect the tidal and wave estimates [*Forbes et al.*, 1997]. The latter problem is perhaps the more serious issue and must be taken into account when extracting tidal and wave components.

Many methods have been developed over the past two decades to accurately extract tides and waves from data obtained from a precessing orbital platform. The methods employed by *Xu et al.* [2007], *Mukhtarov et al.* [2009] and *Oberheide et al.* [2006] are briefly summarized in the rest of this section because they contain concepts that are relevant to this thesis.

The method of *Oberheide et al.* [2002] estimates migrating and non-migrating diurnal tides from temperatures measured by the CRISTA (CRyogenic Infrared Spectrometers and Telescopes for the Atmosphere) satellite instrument. The method focuses on removing the effects of semidiurnal tides by utilizing measurements on the ascending and descending portions of the orbit. Since the measurements on opposite segments of the orbit are about 12 hours apart at low latitudes, the diurnal tides will be sampled at opposite phases. In contrast, the semidiurnal tides are sampled at the same phase. By differencing the ascending and descending measurements, the effects of semidiurnal components are effectively removed. A least squares technique is then implemented to estimate the various zonal wave numbers of the diurnal tides.

In contrast, the method of *Xu et al.* [2007] estimates several migrating components by eliminating the effects of non-migrating components. The objective is to estimate the average zonal mean, the variation of the zonal mean, and the average amplitudes and phases of migrating tides over a 70-day period from TIMED-SABER observations. The fundamental equation for *Xu's* least squares technique is:

$$\frac{1}{2\pi}\int_0^{2\pi} T(t,\lambda)d\lambda = \bar{T}_0(t_0) + \eta(t-t_0) + \sum_{j=1}^{J} T_j^{mig}\cos\left[j\omega_0(t-t_{0,j})\right] + \sum_{l=1}^{L} T_l^{pw}\cos\left[\left(\frac{\omega_0}{D(l)}\right)(t-\alpha_l)\right] \quad (2.29)$$

where t is solar local time, ω_0 is $2\pi/24$, t_0 is the center day of a 70 day window, η describes the linear variation of the zonal mean, j denotes the migrating tide, l denotes the planetary wave, and D(l) is the planetary wave period. Equation 2.29 breaks down the zonal mean temperature for each day and local time into a sum of the average zonal mean for a 70-day window, the zonal mean linear variation, migrating tides and non-stationary planetary waves.

The method of *Xu et al.* begins by sorting 70 days of TIMED-SABER data into bins classified by altitude, latitude, ascending/descending segment, longitude and day. The data for each day, altitude, ascending/descending segment and latitude are essentially at a constant local time due the slow orbital precession rate. To obtain the zonal mean temperature for each day and local time (term on the left-hand side of equation 2.29), the data for each bin are interpolated onto 36 longitude grids and then averaged longitudinally. Averaging with respect to longitude removes the effects of non-migrating and stationary waves because, unlike for migrating tides, different phases of the waves are sampled. By employing this technique over each day in the 70-day window, 140 equations are obtained (two equations per day) for each altitude and latitude. The least squares methods is then employed to estimate the average zonal mean temperature over 70 days, the linear variation of the average zonal mean, and the amplitudes and phases of migrating tides (diurnal, semidiurnal, terdiurnal and 6-h). Although the effects of well-known planetary waves (quasi 2-day, 10-day, 16-day, 23-day) are included in the model, the results are not considered significant because the amplitudes are attenuated during the averaging process from different phase sampling. The 70-day window is then stepped through the next day and the process is repeated.

Mukhtarov et al. [2009] proceeds in a similar way to *Xu et al.* [2007] by assuming that the temperature at a given latitude and altitude can be decomposed into a summation of the average zonal mean, the variation of the zonal mean and the effects of tides and waves. The method differs from *Xu et al.* [2007] in that it does not calculate the zonal mean for each day and constant solar local time to eliminate the effects of non-migrating tides. *Mukhtarov et al.* [2009] instead includes the effects of non-migrating tides in his least squares equation. The least squares solution for the zonal mean and tidal components is then found over a 60-day interval.

Other recent methods that have been applied to TIMED-SABER data to extract tides and waves include *Zhang et al.* [2006] and *Huang et al.* [2009]. Like the methods employed by *Xu et al.* [2007] and *Mukhtarov et al.* [2009], these methods both require at least 60 days of data to provide the necessary solar local time coverage. Hence, the results derived from all of these methods reflect long term variations in the tides and waves, but not shorter term variations of less than 60 days.

Chapter 3

DATA VALIDATION AND COMPARISON

The main goals of this chapter are to establish the validity of the data measured from EOS Aura-MLS and SABER-TIMED and to quantify the differences between the two data sets based on past studies and the analysis to be presented. The two goals are crucial for assessing the accuracy of the least squares model of the MDT presented in Chapter 4 and for interpreting the final results presented in Chapter 5.

3.1 Aura-MLS Data

The Microwave Limb Sounder (MLS) instrument was launched aboard the Earth Observing System (EOS) Aura Spacecraft on July 15, 2004 with the objective of improving the understanding of global change in the earth's stratosphere, mesosphere and upper troposphere [*Jiang*, 2004]. The instrument measures microwave thermal emission from the limb of the earth's atmosphere using radiometers to create vertical profiles of atmospheric gases, pressure, cloud ice and most importantly in this paper, temperature. MLS consists of an antenna assembly to collect radiances and a optical multiplexer to separate and transfer the signal to radiometers in five different spectral regions from 115 GHz to 2.5 THz. Temperature, geopotential height, and tangent pressure are derived from radiances measured by the 118-GHz and 234-GHz radiometers.

Retrieval algorithms convert the remote measurements of radiation into estimates for temperature and other geophysical parameters. The MLS retrieval algorithm is initialized by an initial state vector that contains aspects describing the current state of the atmosphere obtained from climatological data sets. It also contains additional information about the state of the measurement system [*Livesey et al.*, 2004]. A forward model predicts the radiances that the instrument would observe if it were in the state described by the state vector. The predicted radiances are compared then to the actual observed values in order to adjust the state vector parameters accordingly. This process is iterated until a final state vector containing vertical profiles of various geophysical parameters is obtained. The MLS retrieval algorithm is further detailed by *Livesey et al.* [2004].

The Aura spacecraft is one of nine currently active satellites in the NASA Earth Observing System. It follows a sun-synchronous orbit with an altitude of 705 km, an inclination of 98.2° and an ascending node crossing local time of 13:45. The orbital altitude translates to Aura traveling 14 orbit revolutions per day. The MLS instrument is located in the front of the Aura spacecraft where it faces in the along-track direction and tangential to the earth's atmosphere for limb viewing. MLS takes measurements at latitudes between -82° and 82°. About every 24.7 seconds, the MLS instrument performs a limb scan to make radiance measurements. During a limb scan, the instrument scans upward from the tangential surface of the earth to a height above 110 km in about 20 seconds *[Waters,* 2004*]*. The limb scan frequency equates to a 1.5° along-track spacing between each scan. The exception is observed at latitudes above 80° or below -80° where the along-track spacing between each scan is much smaller. Daily global coverage of the MLS instrument is shown in Figure 3.1.

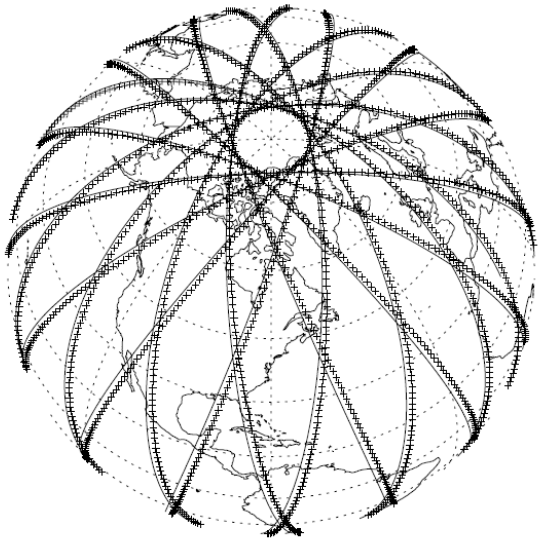

Figure 3.1: MLS measurement locations for a 24 hour period [*Jiang*, 2004]. There is about a 1.5° latitude spacing between measurements.

Since the orbit of Aura is sun-synchronous, MLS observations occur at two solar local times for a particular latitude (one on the ascending half and on the descending half). For latitudes between ±70°, the solar local times of the measurement locations are between 12:00 and 16:00 for the ascending segment, and between 0:00 and 4:00 for the descending segment. The change in solar local time with respect to latitude is much larger at high latitudes. For example, the solar local time change from 70° to 80° is greater than 2 hours. The large change with respect to latitude is expected due to the small distance between longitudes and consequently, solar local times near the poles.

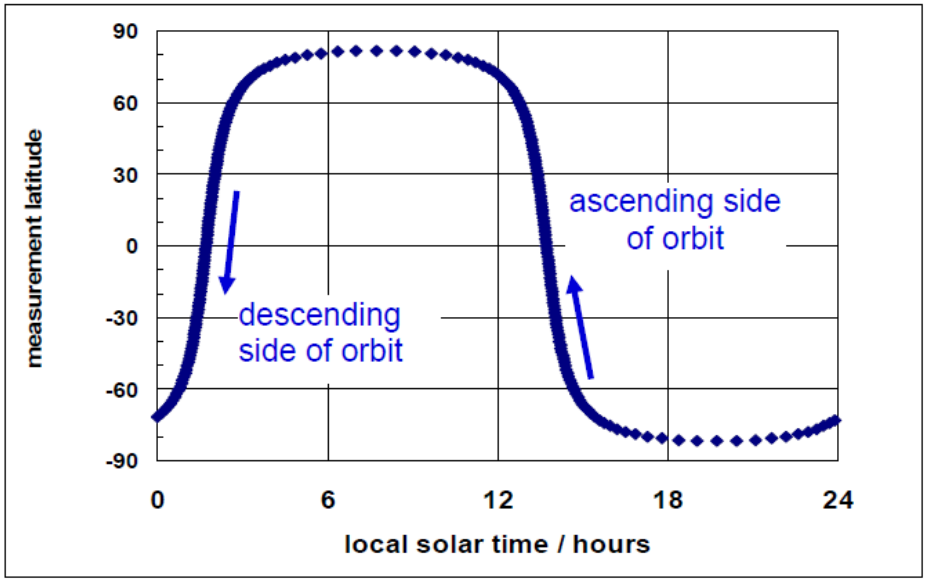

Figure 3.2: MLS solar local time at each measurement latitude [*Waters*, 2004].

MLS data is processed to various levels from raw radiance measurements to daily zonal mean estimates. In this analysis, Version 3.3 (v3.3) "Level 2" temperature data are used, which contain vertical temperature profiles for each day. For the "Level 2" data set, temperature retrieval algorithms place the data on the same vertical grid at specific pressure levels by assuming the radiances and temperatures between each pressure level is a piecewise linear function. Thus, the temperatures at a given pressure level might not actually represent the temperatures observed and instead exhibit the linearly interpolated values. Only temperature data between 261-0.001 hPa are considered useful for v3.3 data [*Livesey et al., 2011*]. As shown in Table 3.1, the vertical resolution of the data is generally highest in the stratosphere and degrades in the mesosphere and thermosphere.

Pressure Range	261 hPa to 100 hPa	56.2 hPa to 3.16 hPa	1 hPa to 0.316 hPa	0.1 to 0.001 hPa
Vertical Resolution	~5 km	~4 km	~7.2 km	~10 km

Table 3.1: Vertical resolution of MLS data

The MLS "Level 2" data files also contain parameters associated with the temperature measurements including latitude, longitude, solar local time, universal time, pressure, and data quality metrics. The three metrics that are used to determine the quality of each temperature profile are *quality*, *status*, and *convergence*. The *quality* and *convergence* values depict how well the radiance measurements fit the predicted radiance measurements from the retrieval algorithm for a given data set. *Status values* flag any questionable data that should not be used in scientific studies. In this analysis, any data containing a *quality* value of less than 0.65, a *convergence* value of more than 1.2 and a *status* value that is odd numbered were not used.

3.2 TIMED-SABER Data

The SABER instrument onboard the TIMED spacecraft was launched on December 7, 2001 with the purpose of observing the atmospheric processes in the mesosphere and lower thermosphere. SABER is a passive multispectral radiometer that measures infrared emissions (1.27 μm-16.9 μm) from the limb of the earth's atmosphere. Temperature, pressure and altitude are derived by inverting the radiances observed in the 4.3 μm and 15 μm CO_2 bands [*Remsberg et al.,* 2008].

TIMED is located in a low earth orbit with an altitude of 625 km and an inclination of 74.1°. The orbit is considered to be quasi sun-synchronous because the solar local time at a given location directly beneath the spacecraft decreases by about 12 minutes per day. It takes about 60 days for the spacecraft to cover 24 hours in solar local time at a given latitude and 120 days for the ascending node of the orbit to repeat a solar local time. SABER is located on the side of the TIMED spacecraft and takes measurements perpendicular to the along-track direction. Limited by the orbital altitude, SABER provides a maximum of 15 orbits of data per day. The TIMED yaw cycle determines the latitude coverage of the SABER measurements. For one, 60-day

portion of the yaw cycle, SABER provides measurements between -52° and 84° latitude. A 180° spacecraft yaw transitions the instrument to the other portion of the yaw cycle. For the second, 60-day portion, observations are viewed between -84° and 52° latitude.

Like the MLS instrument, SABER measures atmospheric emissions by scanning the limb of the earth's atmosphere. The SABER scan process is slightly more involved than the MLS scan. It consists of a calibration scan, an acquisition scan, and a baffle scan in addition to two up/down scans when the actual radiance measurements are made [*Remsberg et al.*, 2008]. During an up/down scan, the instrument scans upward to about 400 km tangential height and then downward to near the surface of the earth. One up/down scan takes about 90 seconds to complete.

Vertical profiles of observed radiances are placed onto the SABER vertical grid by a multiple interleave approach [*Remsberg et al.*, 2008]. One benefit of the interleave approach is the minimal smoothing of the profile that results, which is an advantage for tidal extraction. The method begins by creating a new radiance sub-profile that is based on every fifth point of the original radiance profile. The spacing between every fifth point is about 1.9 km, which is about the vertical resolution of the measurement. Four more profiles are similarly obtained by selecting a different starting point and taking every fifth point. The five profiles are then interpolated onto an equally spaced vertical grid of 0.375 km spacing and then averaged together. The result is a final radiance profile with 1.9 km vertical spacing. The pressure and temperature values for each vertical level are obtained from the final radiance profiles by the retrieval algorithm, explained in further detail by *Remsberg et al.*, [2008].

The newest version of SABER data (Version 1.07) is used in this analysis. In addition to temperature data, each data file contains measurement information on latitude, longitude, pressure, universal time and height. Unlike the MLS data sets, the SABER data sets are screened

for questionable temperature and pressure profiles before being released to the public. For instance, all measurements made above 140 km and below 11 km were not included in the data file. Consequently, the implementation of quality thresholds is not needed in the analysis.

One observation concerning the SABER data that should be noted is the dependence of latitudinal spacing on the portion of the yaw cycle. For the southern hemisphere portion of the yaw cycle, latitudinal resolution is better in the northern hemisphere, which is displayed in Figure 3.3. While almost all latitudes provide measurements on every orbit in the high northern hemisphere, there are many latitudes in the southern hemisphere where measurements are not made. Latitude coverage is very good at high latitudes in the northern hemisphere because latitudes are overlapped between successive limb scans. The gaps in latitude coverage at lower latitudes and southern latitudes can be partially explained by the fact that measurements above 140 km and below 11 km are not included in the data file. The trend is reversed when TIMED transitions to the northern hemisphere portion of the yaw cycle. Latitude coverage is better in the southern hemisphere during this portion. The impact of these trends on data processing and results will be explained in the next chapter.

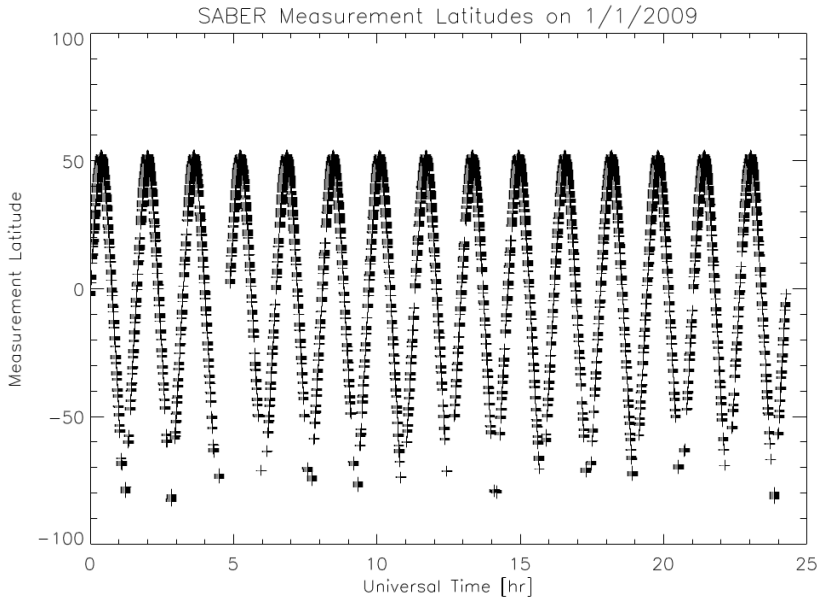

Figure 3.3: SABER measurement latitudes on 1/1/2009. The latitude coverage for this portion of the yaw cycle spans from about -84° to 52°.

3.3 Prior Validation

Data validation is necessary to identify any issues that might impact the results obtained from the method presented in this study. In this section, prior validation for both the MLS and SABER data and past comparisons between the two data sets are summarized and presented.

3.3.1 MLS Data Validation

Although a validation paper has not yet been written for the MLS Version 3.3 temperature data set, validation studies have been conducted for past data sets. The most recent validation paper was written by *Schwartz et al.* [2008] regarding the MLS Version 2.2 data set. The most important conclusion from the paper is that only temperature profiles obtained at pressures between 316 hPa and 0.001 hPa can be considered scientifically useful. Temperature precision based on the propagation of radiance measurement uncertainty through the retrieval algorithm is also quantified at each altitude. The precision ranges from 0.6 K in the lower

stratosphere to 2.5 K in the mesosphere. In order to quantify temperature biases, comparisons between the MLS data set and other correlative data sets are performed. The biases concluded from the comparisons are within ±3 K in the stratosphere, but increases to about ±9 K near the mesopause.

Since the retrieval algorithms associated with the Version 2.2 and Version 3.3 data sets are almost identical, the products are very similar [*Livesey et al.*, 2011]. Therefore, many of the conclusions presented in *Schwartz et al.* [2008] can also be inferred for the Version 3.3 data set. The main difference between the Version 3.3 and Version 2.2 MLS temperature data sets is the change in vertical grid. Version 3.3 data is placed on a vertical grid that has better resolution in the upper stratosphere and mesosphere at the expense of precision. Another difference between the data set versions concerns the 316 hPa pressure level for the Version 3.3 data set, which has been found to contain larger biases and should not be considered for scientific use.

3.3.2 SABER Data Validation

Validation of the SABER Version 1.07 temperature data set is presented by *Remsberg et al.* [2008]. The data set is essentially unchanged from the previous version (Version 1.06) for altitudes below 70 km where a local thermodynamic equilibrium (LTE) retrieval algorithm is employed. The primary sources of systematic error noted by *Remsberg et al.* [2008] for this region are errors in the measured radiances, biases in the forward model, uncertainties in ozone correction, uncertainties in the determination of the reference pressure for the retrieved profiles and not accounting for horizontal temperature gradients at high latitudes. The propagation of these systematic errors results in uncertainties of ±1.4 K in the lower stratosphere, ±1 K in the middle stratosphere, and ±2 K in the upper stratosphere and lower mesosphere. A non-LTE algorithm is used for altitudes above 70 km because non-LTE effects cannot be ignored when the

temperature is below ~170K. Since the non-LTE algorithm depends on knowledge of carbon dioxide decrease and monatomic oxygen increase with altitude, the respective knowledge uncertainties constitutes the main sources of error. Uncertainties in the temperature estimates range from ±2.3 K at 80 km to ±8.4 K at 100 km at middle latitudes. The uncertainties are much higher during the polar summer due to the limited knowledge of atmospheric gas profiles and processes during the period.

Remsberg et al. [2008] also compare the Version 1.07 SABER data set to various ground-based and space-based instruments. The comparisons reveal SABER biases that range from ±1 to ±3 K in the stratosphere and lower mesosphere, similar to the stated SABER measurement uncertainty. Comparisons at higher altitudes indicate that the SABER non-LTE retrieval algorithms are of good quality. Biases between SABER and other instruments in this region are within ±5 K.

3.3.3 Past SABER/MLS Comparisons

The most recent comparison between SABER and MLS data sets was reported by *Schwartz et al.* [2008]. Although the versions of the compared data sets are Version 2.2 for MLS and Version 1.06 for SABER, the older sets are similar enough to the data sets used in this paper for the results to be relevant. A summary of the comparison is presented here.

Schwartz et al. [2008] compare the data sets by finding MLS and SABER profiles within 220 km and 3 hours in universal time from September 2004 to January 2007. Since the SABER data is placed on a higher vertical resolution grid, the data is degraded to the MLS vertical grid through interpolation using a least squares approach. The mean differences between the profiles for each latitude and seasonal bin are shown in the top five plots of Figure 3.4. The bottom five plots display the standard deviation of the differences.

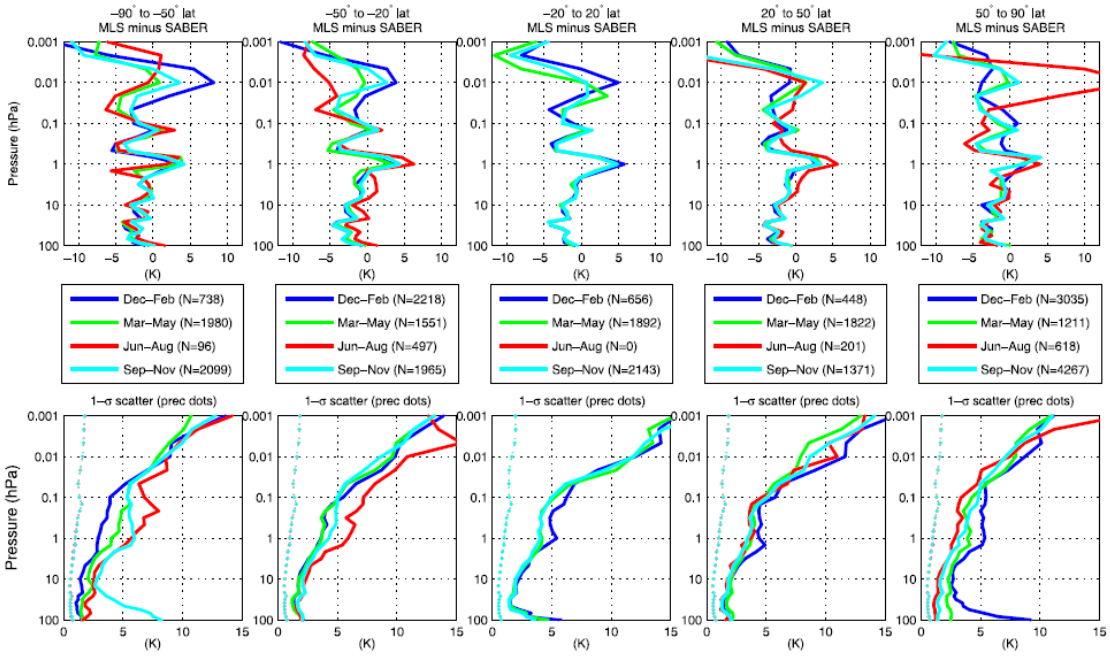

Figure 3.4: MLS v2.2/SABER v1.06 temperature comparison [*Schwartz et al.*, 2008]. The average temperature differences between the two instruments are shown in the top five plots for each month and latitude range. The 1-σ scatter is shown in the bottom five plots.

The plots show the MLS data containing a cold bias with respect to the SABER data throughout most of the pressure levels. The major exception occurs at the 1 hPa pressure level where MLS has a 3-5 K warm bias. The MLS-SABER bias stays within ± 5 K throughout most of the middle atmosphere until about the 0.01 hPa pressure level. In the upper mesosphere region, the bias exceeds the ± 10 K range in several seasonal and latitudinal bins. The standard deviation plots show that the bias is well characterized in the stratosphere, but the scatter of the biases increases in the upper levels of the atmosphere. The scatter of the MLS-SABER differences result from the combined precision and accuracy of the MLS and SABER measurements as well as imperfect coincidences.

3.4 Comparative Analysis of SABER and MLS Data Sets

The method of determining the MDT that is presented in this thesis requires temperature data from both MLS and SABER. The temperatures observed by the two instruments at similar locations in the earth's atmosphere should be in agreement to mitigate systematic error in the MDT estimation. Since there has been limited prior validation between the newest MLS and SABER temperature datasets, a comparison is performed and presented in the remainder of this chapter. An analysis of the systematic differences between MLS and SABER is conducted by comparing similar or "common" profiles between the two instruments.

3.4.1 Data Processing

In order to compare MLS and SABER temperature profiles, both data sets must be placed on a similar grid. To accomplish this task, every temperature point in a daily data set is binned according to ascending or descending segment, orbital number, latitude and pressure level. The latitudinal grid is chosen to consist of 33, 5° bins between -82.5° and 82.5°. To solve the problem of different vertical grids, *Schwartz et al.* [2008] used a linear interpolation technique to degrade the higher resolution SABER data to the lower resolution MLS data. The technique is also suggested by the Aura-MLS science team [*Livesey et al.*, 2011] for accurate comparisons between different instruments, but is not applied in this study. The main reason for not employing this technique is that the approach may smooth out the SABER profiles and cause some tidal information to be lost. SABER data are instead binned according to the closest MLS pressure level within 2 km. However, any SABER data that is not within 2 km from the nearest pressure level is not included in the study in order to keep a relatively uniform temperature

distribution at each pressure level. After the data have been placed in the appropriate bin, the data in each bin are averaged.

3.4.2 Comparison Results

In this analysis, common profiles are defined as MLS and SABER temperature profiles that are located within identical 5° latitude bins, measured on the same day, and observed within 20 minutes of solar local time. The existence of common profiles between the two instruments is possible due to TIMED's full solar local time coverage. SABER measurements made at specific latitudes between -52° and 52° covers a diurnal range of solar local time except between 11:00 and 13:00 in 120 days. It is subsequently expected that there are two common profiles (one for each Aura orbital segment) per TIMED orbital segment for these latitudes during the 120 day cycle. Common profiles beyond the -52° and 52° range are less frequent due to TIMED yaw maneuvers. Furthermore, the yaw adds slight complexity in predicting the common profiles at low latitudes by backtracking solar local times during a cycle. The dates of common profiles for various latitudes are displayed in Figure 3.5.

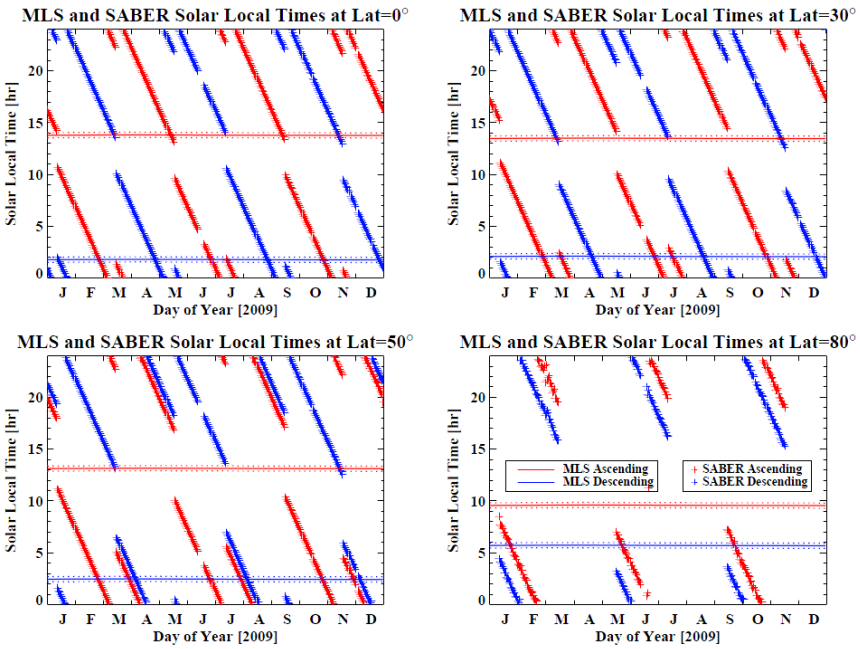

Figure 3.5: Solar local time coverage for MLS and SABER for 2009 at various latitudes. The coverage for each orbital segment is shown. TIMED precesses through a diurnal range of solar local time, which allows for common profiles.

For each common occurrence date, the orbital profiles for the day and latitude are averaged to create one average profile for each instrument. The temperatures for each instrument and orbit for the 2/25/09 common occurrence date at the equator are shown in Figure 3.6 for example. The resulting zonally averaged profile can be seen in Figure 3.7.

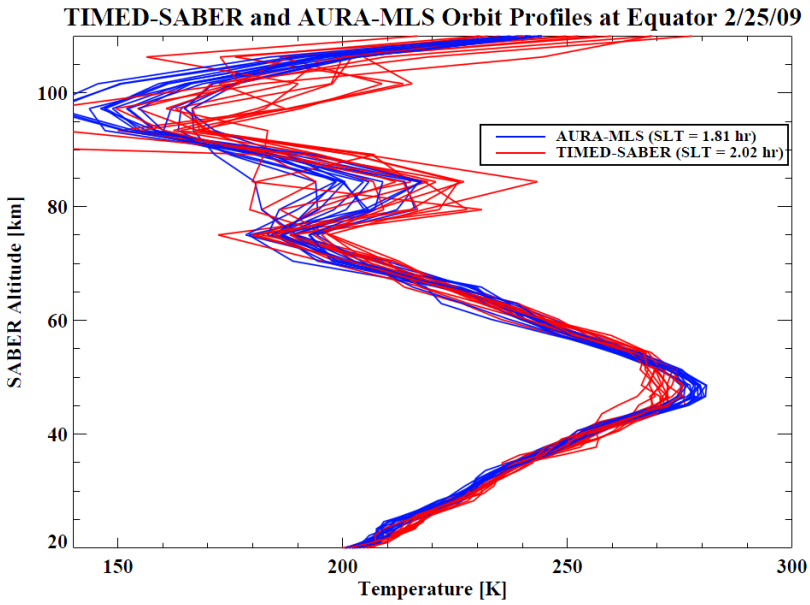

Figure 3.6: Temperature profiles for each orbit on a common profile day. Each profile is measured within 20 minutes in solar local time of each other.

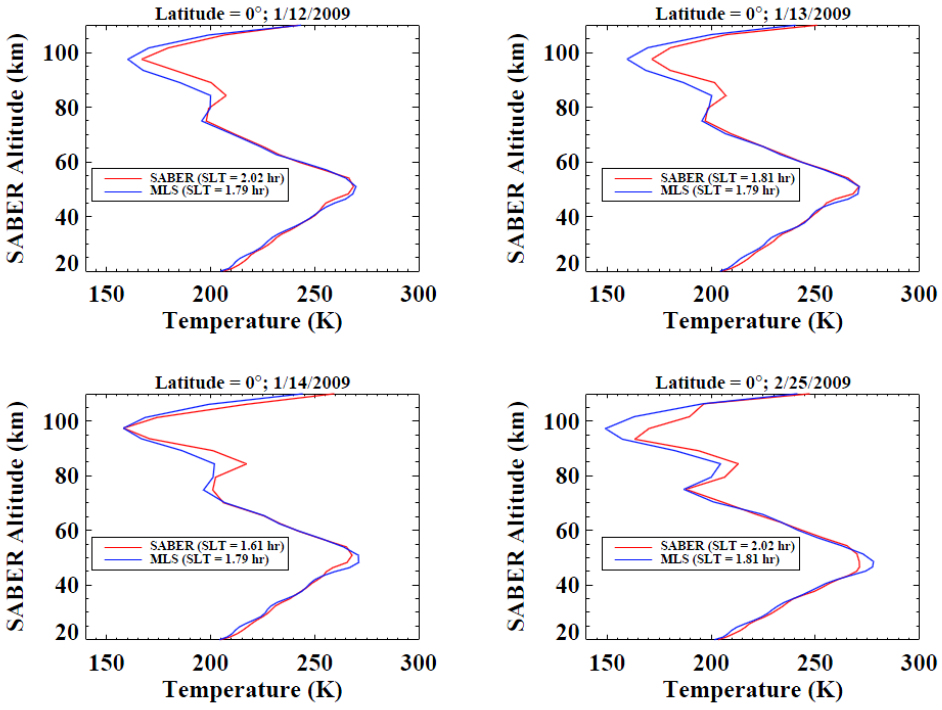

Figure 3.7: Average temperature profiles for selected common profile days. The plots display evidence of tidal effects above 75 km.

The common SABER and MLS profiles are then differenced to analyze the differences between the two datasets. The average differences at each latitude and pressure level for 2009 are displayed in the next three figures.

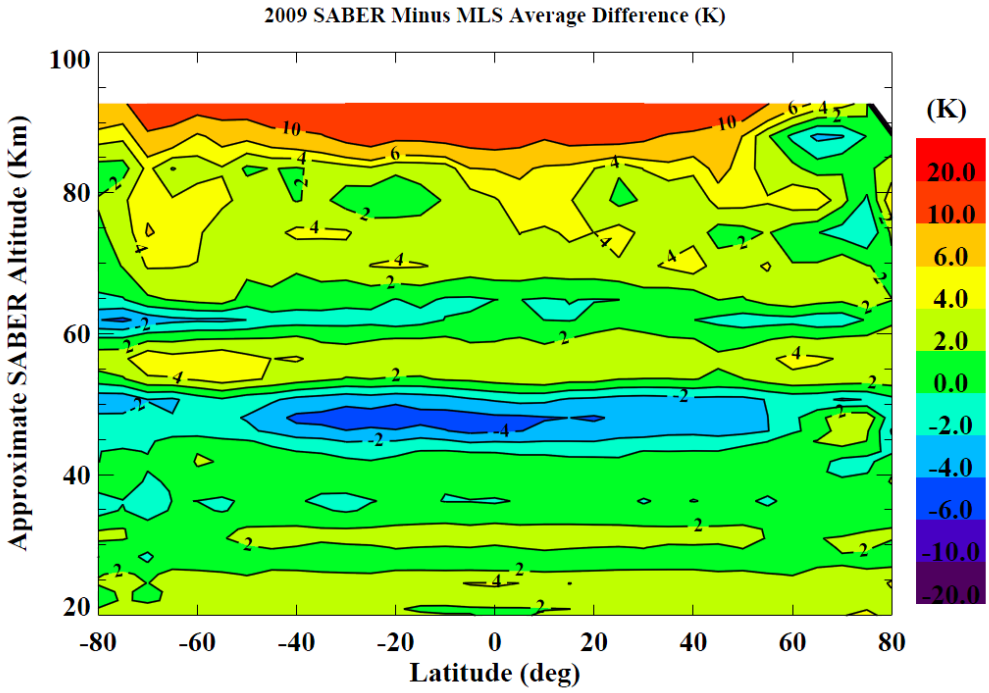

Figure 3.8: 2009 SABER/MLS average difference. The differences are a function of altitude and latitude. Contour spacing is 2 K.

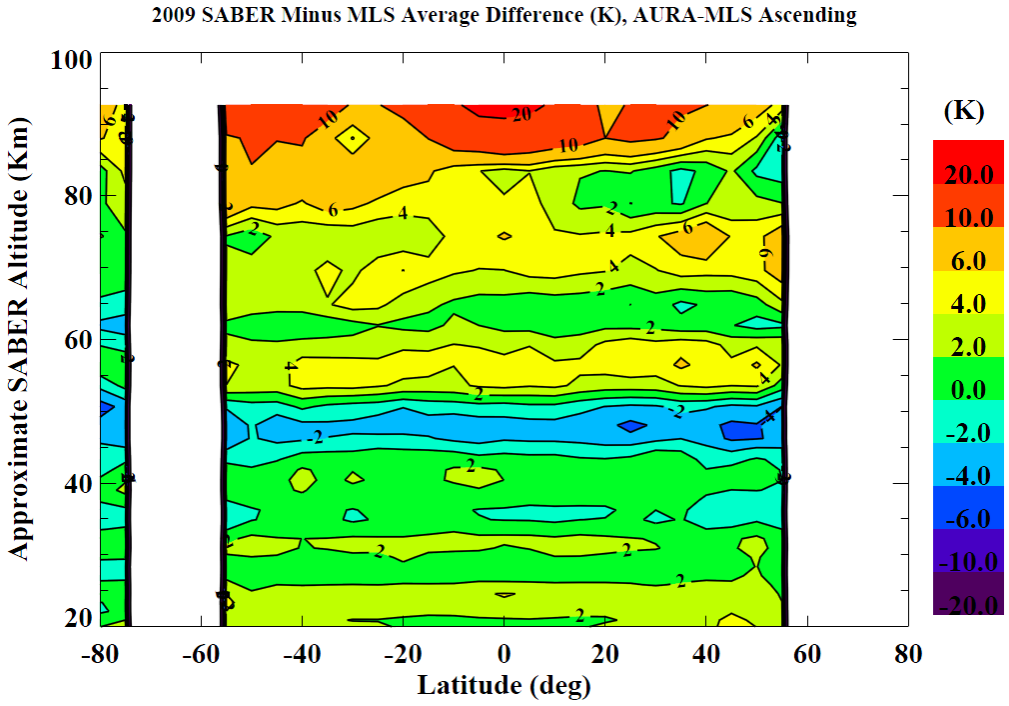

Figure 3.9: 2009 SABER/MLS average difference for the MLS ascending segment.

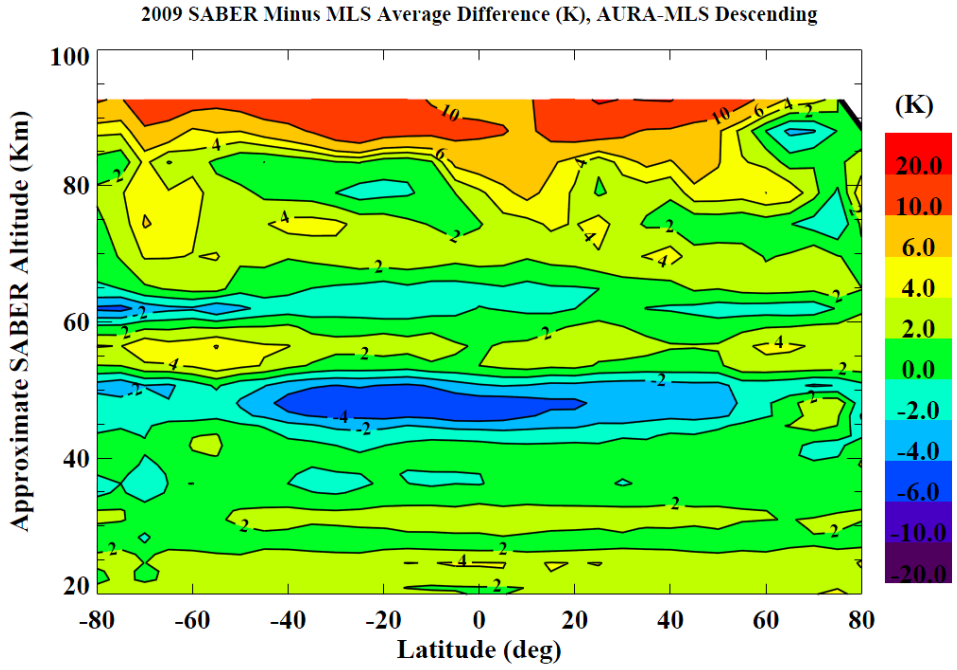

Figure 3.10: 2009 SABER/MLS average difference for the MLS descending segment.

The results displayed here are similar to the *Schwartz et al.* [2008] comparison, which is comforting since a different technique was applied to place the SABER and MLS data on the same vertical grid. The bias between the two instruments is mainly altitude-dependent although there is a weak latitudinal relationship. SABER is warmer throughout most altitudes by about 0-6 K except near the 1 hPa pressure level where MLS contains a 2-6 K warm bias at most latitudes. The bias is significantly larger in the upper mesosphere region where some biases are larger than 10 K. These large biases were also observed by *Schwartz et al*. [2008]. The comparison stops at about 95 km (~0.001 hPa) because the data above this level should not be considered for scientific use as denoted by the MLS scientists. From Figure 3.9 and Figure 3.10, it can be seen that the bias also depends on the MLS ascending and descending segments. These observations are important for the tidal results processing, which is explained in the next chapters.

Chapter 4

WAVE FITS AND FILTERING

In the following chapter, the least squares method for determining the daily zonal mean, amplitude and phase of the MDT is presented. Figures of merit are established to determine where the solutions may be impacted by data sampling or data quality and to provide ways to interpret the final results.

4.1 Least Squares Method

As explained in Chapter 2, the fundamental problem with estimating the features of migrating tides from instruments in sun-synchronous orbits is that, in the best case, measurements only available at two solar local times and hence, two phases of the MDT. The method presented here avoids that problem by introducing a second satellite instrument to increase solar local time coverage, and allows the MDT to be estimated with daily resolution.

The amplitude and phase of the MDT and the daily zonal mean at a given altitude and latitude are estimated on a daily basis by fitting a sinusoid to the temperatures measured at four different solar local times. Four solar local times are necessary for fitting to the three parameters with one degree of freedom and are made available at a given altitude and latitude through the use of two essentially, sun-synchronous satellites if viewed on a daily time frame. Although

TIMED-SABER is in a quasi synchronous orbit, the solar local time only changes by about 12 minutes per day, which allows it to be considered sun-synchronous over a daily time interval.

For each day, the temperature at each solar local time is calculated by zonally averaging data at a given altitude and latitude. In addition to the simplicity of fitting a wave through four data points, the purpose of orbital averaging is to eliminate effects that are not sun-synchronous including non-migrating tides and planetary waves. In contrast, the same phase of the MDT will be measured on every sun-synchronous orbit at a given latitude and altitude because it moves with the apparent motion of the sun. This concept is illustrated in the following figure.

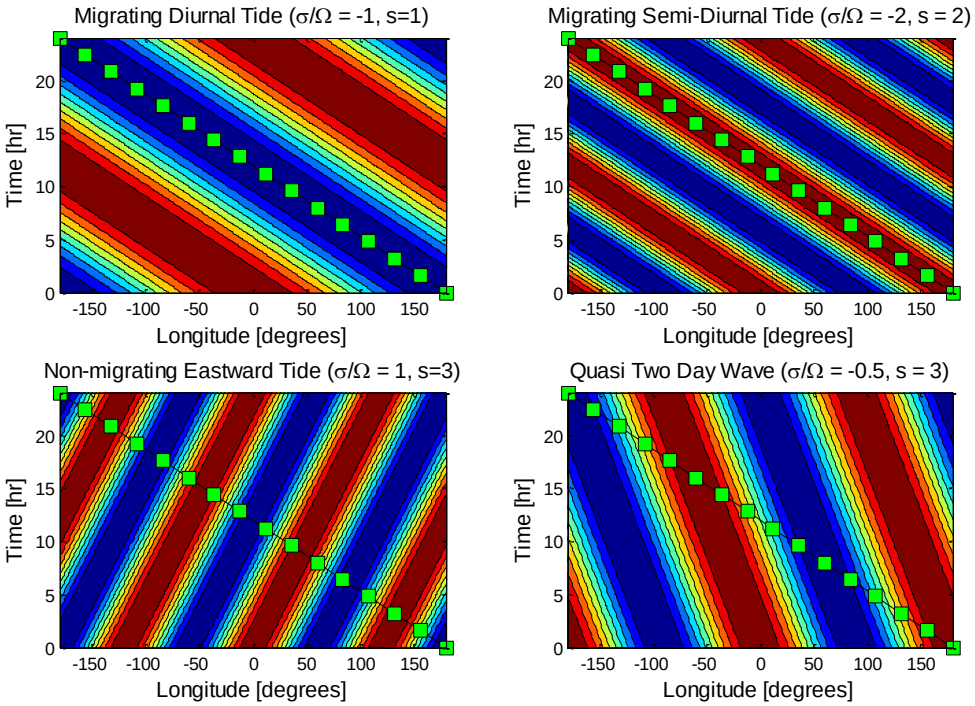

Figure 4.1: Wave phase as a function of time and longitude. Green dots correspond to sampling of an instrument in sun-synchronous orbit. Colors represent the phase of the featured wave. Plots for the diurnal tide, semidiurnal tide, a non-migrating eastward tide and the quasi two-day wave are shown.

As shown in the top-left plot, the same phase of the MDT is sampled every orbit. A point on the wave travels 24° longitude in 90 minutes, equal to the longitudinal rate of change of a sun-synchronous ground track at a given latitude. The semidiurnal tide (top-right plot), the terdiurnal tide and other migrating tides also are sampled at the same phase for each sun-synchronous orbit because they propagate at the same rate and direction as the sun. Other tides such as non-migrating tides and planetary waves are not sampled at constant phase as shown in the figure. Hence, the temperature oscillations due to these waves are eliminated or attenuated by the averaging process. This process was also illustrated by *Xu et al.* [2007] as explained in Chapter 2. The degree of attenuation depends on the number of samples and if the samples are well-spaced. A large number of evenly-spaced samples allows for more phases of non-sun synchronous effects to be sampled. Averaging over many phases results in a more likely attenuation of non-sun synchronous effects.

Sun-synchronous effects (semidiurnal, terdiurnal, etc.) are not eliminated by the orbital averaging process because they are also sampled at constant phase. Migrating tides have the potential to impact the MDT estimates especially if they have large tidal amplitudes. Although the MDT is the most dominant tide below the thermosphere, the semidiurnal tide can be significant at higher altitudes and certain latitudes. A recent study was conducted by *Friedman et al.* [2009] to estimate the semidiurnal tide from two ground-based lidars and TIMED-SABER data. Semidiurnal amplitudes at about 20° latitude and 85 km ranged from ~0-10 K over an annual time span. The semidiurnal tidal amplitudes grow exponentially with altitude and become significant at altitudes greater than 85 km. The results of the study provide evidence that the semidiurnal tide can achieve large enough amplitudes to influence the estimation of the MDT in the MLT region if it is not attenuated. The terdiurnal tide and higher harmonics are much smaller

than the MDT and semidiurnal tide so those respective tides are not of great concern [*Aso et al.*, 2003].

The impact of the semidiurnal tide on the results is reduced by employing the least squares method with one degree of freedom to estimate the MDT. If the samples are properly spaced in solar local time, the semidiurnal tidal effects should only appear as residual errors. An illustration of the effects of the semidiurnal tide on the MDT estimates when the solar local time is evenly-sampled is shown in Figure 4.2.

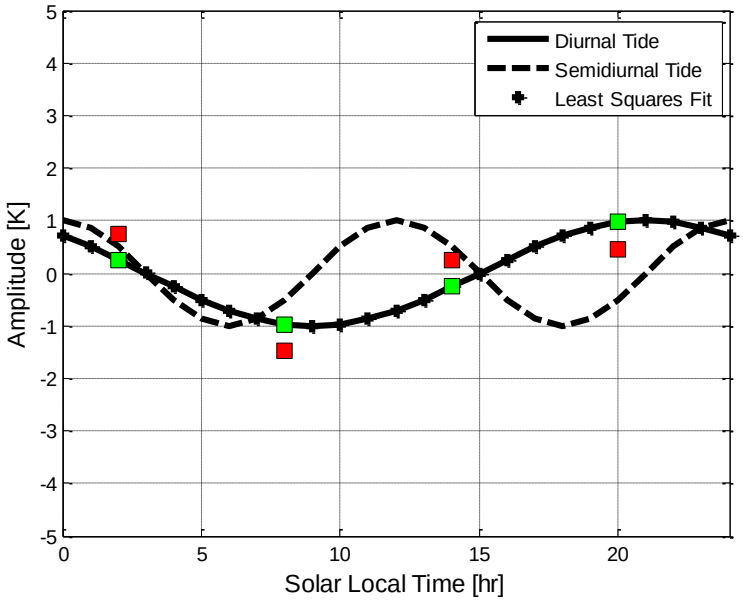

Figure 4.2: Effect of the migrating semidiurnal tide (dashed) during good sampling of MDT (solid) example.. The green markers represent the temperature perturbation solely due to the MDT. The red markers represent the temperature perturbation due to the MDT and the semidiurnal tide. The '+' symbols represent the least squares fit to the red markers.

It can be seen in the figure that the semidiurnal tidal amplitude is identical to the MDT amplitude and has an impact on the zonally averaged temperatures. However, the least squares method will minimize the residual errors caused by semidiurnal tide and will produce a solution

that still resembles the actual MDT as shown in the figure. Consequently, the effects of the semidiurnal tide will only appear as residual errors.

For comparison, the effect of the semidiurnal tide on the least squares estimate from a poor sampling is illustrated in Figure 4.3. In this case, samples of the MDT are taken at essentially three phases. Therefore, the least squares method will produce estimates with almost zero degrees of freedom. It can be seen from the figure that fitting to essentially three points denoted in red will produce a solution that is significantly different from the actual MDT. It is concluded that the semidiurnal tide can have a large impact on the MDT estimates if the semidiurnal tidal amplitude is large and the solar local time sampling is poor.

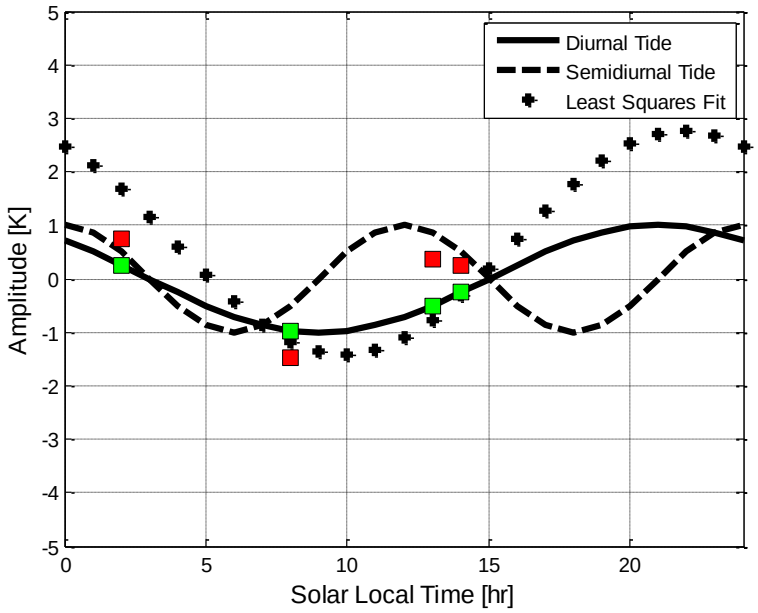

Figure 4.3: Effect of the migrating semidiurnal tide (dashed) during poor sampling of MDT (solid) example. The green markers represent the temperature perturbation solely due to the MDT. The red markers represent the temperature perturbation due to the MDT and the semidiurnal tide. The '+' symbols represent the least squares fit to the red markers.

With the effects of other tidal harmonics removed or significantly reduced, the least squares method is applied to fit a sinusoid to the zonal temperature averages at four solar local

times. Although the MDT is a collection of trapped and propagating wave modes, the (1,1) mode is easily the most dominant in the stratosphere and mesosphere. Therefore, the MDT is assumed to behave as a single perturbation sinusoid about a daily zonal mean. Consequently, the atmospheric temperature due to the sole influence of the MDT can be decomposed by the following:

$$T(t_{SLT}) = A_0 + A_1 \cos\left(\frac{2\pi t_{SLT}}{24}\right) + A_2 \sin\left(\frac{2\pi t_{SLT}}{24}\right) \tag{4.1}$$

Four temperatures at four solar local times throughout the day forms a system with four equations with three unknowns (A_0, A_1, and A_2) as shown in equation 4.2.

$$\begin{bmatrix} T_1 \\ T_2 \\ T_3 \\ T_4 \end{bmatrix} = \begin{bmatrix} 1 & \cos\left(\frac{2\pi t_{SLT,1}}{24}\right) & \sin\left(\frac{2\pi t_{SLT,1}}{24}\right) \\ 1 & \cos\left(\frac{2\pi t_{SLT,2}}{24}\right) & \sin\left(\frac{2\pi t_{SLT,2}}{24}\right) \\ 1 & \cos\left(\frac{2\pi t_{SLT,3}}{24}\right) & \sin\left(\frac{2\pi t_{SLT,3}}{24}\right) \\ 1 & \cos\left(\frac{2\pi t_{SLT,4}}{24}\right) & \sin\left(\frac{2\pi t_{SLT,4}}{24}\right) \end{bmatrix} \begin{bmatrix} A_0 \\ A_1 \\ A_2 \end{bmatrix} \tag{4.2}$$

A least squares solution can be found by solving equation 4.3 where **Y** denotes the [4x1] vector containing the zonal temperature, **B** is the [4 x 3] matrix describing the linear operator, and $\widehat{\mathbf{X}}$ is the [3x1] coefficient vector. The least squares solution, the one that minimizes the square of the residuals, is displayed in equation 4.4.

$$\boldsymbol{Y} = \boldsymbol{B}\widehat{\boldsymbol{X}} \tag{4.3}$$

$$\widehat{\boldsymbol{X}} = (\boldsymbol{B}^T\boldsymbol{B})^{-1}\boldsymbol{B}^T\boldsymbol{Y} \tag{4.4}$$

It should be noted that a unique solution can be determined from three temperatures at three solar local times. However, a unique solution does not contain any information about error. A system of four equations is hence constructed to solve for a least squares solution to quantitatively assess the fit of the model.

The first term of the least squares solution, A_0, represents the daily zonal mean or daily average temperature. The last two terms, A_1 and A_2, convey information about the amplitude and phase of the MDT. Amplitude is a measure of the temperature perturbation, while phase gives information on the position of the tide with respect to the solar local time when the maximum amplitude occurs. Since the sine and cosine portions are orthogonal components of the wave, the amplitude and phase of the wave are calculated by equations 4.5 and 4.6.

$$Amplitude = \sqrt{{A_1}^2 + {A_2}^2} \quad [K] \tag{4.5}$$

$$Phase = \frac{24}{2\pi} tan^{-1}\left(\frac{A_2}{A_1}\right) \quad [hr] \tag{4.6}$$

4.2 Chi-Square Value

4.2.1 Introduction

The motivation for using four solar local time measurements to solve for three unknown variables (A_0, A_1, A_2) is to obtain information on the quality of the solution. The diagnostic that determines the degree of fit is the chi-square value, χ^2, which is defined by:

$$\chi^2 = \frac{1}{\nu}\sum_{i=1}^{4}(y_{observed} - y_{fit})^2 \tag{4.7}$$

The number of degrees of freedom, ν, is equal to one in this case. Thus, the chi-square value is the sum of the squares of the residual errors. Examples of good and bad chi-square values are shown in Figure 4.4. The plots on the left are cases where the least squares solution does not fit the measurements well, which results in a large chi-square value. In contrast, the wave solutions displayed on the right of the figure have low chi-square values and residual errors.

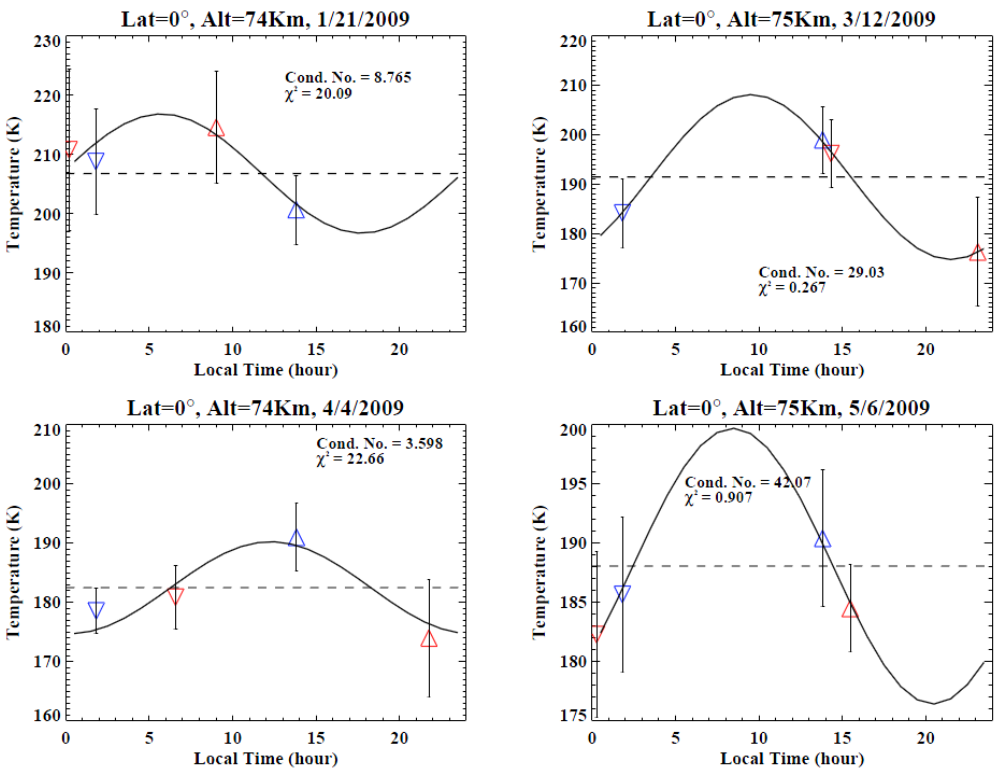

Figure 4.4: Examples of wave fits. The blue symbols represent zonal average temperatures derived from the MLS instrument. The red symbols represent zonal averages from the SABER instrument. Error bars represent 1-σ scatter of the temperatures for each zonal average. A wave is fitted to the four zonal averages in order to represent the MDT.

The magnitude of the chi-square value is determined by the degree of fit, which is subsequently dictated by how well the model and associated assumptions fit the actual observations. For the solution method, it is assumed that the effects of non-migrating tides and planetary waves are at least reduced by zonal averaging. Failure to effectively eliminate the non-migrating tides and planetary waves could result in a higher chi-square value. Although the effect of the migrating semidiurnal tide is mitigated by fitting to one degree of freedom, the semidiurnal tide can still impact the estimates when it is large and the MDT is poorly sampled. Finally, instrument measurement errors can also affect the degree of fit. If the values measured

by the instrument do not represent the true atmospheric value then the obtained solutions will not effectively model the actual atmosphere.

4.2.2 Number of Orbits Averaged

The degree of effectively eliminating or attenuating the effects of non-migrating tides and planetary waves mainly depends on the number of samples used in the averaging process. Failing to reduce the effects could result in a high chi-square value because one of the assumptions of the model is invalidated. An important parameter that determines the effectiveness of filtering out other tides is the number of data orbits used in the zonal averaging process. The number of orbits where data is provided at a given latitude and day vary especially at high latitudes due to SABER's sampling as shown in Figure 3.3 (Chapter 3). The wide range of data orbits at a given latitude on a certain day allows for interpretation of its impact on filtering out non-migrating components. The following figure displays the correlation between the chi-square value and the minimum number of orbits averaged.

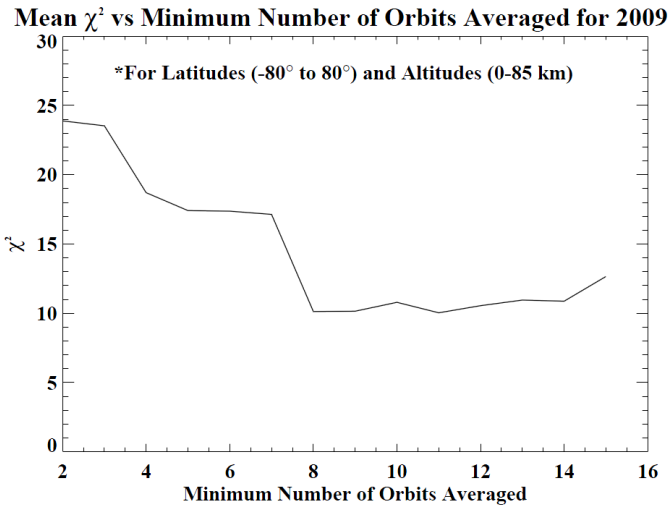

Figure 4.5: Mean chi-square value vs. minimum number of orbits averaged for 2009. Data for latitudes between -80° and 80° and altitudes up to 85 km were used.

There is a clear improvement in the quality of the results as the number of orbits averaged increases from two to eight. In the area of decrease, it is concluded that the zonally averaged temperatures derived from small sample sizes does not effectively reduce non-sun synchronous effects. An increased number of samples in the zonal average allows for effects from tides with higher wave numbers to be eliminated. The mean chi-square value of the fits is about the same from eight orbits averaged and higher, signifying an effective cutoff. For the final analysis, it is required that all fits are computed on data where a minimum of eight profiles are available to compute the zonal average.

4.2.3 Removal of Bias

The measurement differences between the instruments can also impact the accuracy of the model and least squares fit results. Existing measurement biases as shown in Figure 3.8-Figure 3.10 result in temperature measurements that are systematically different. These biases introduce additional errors in the least squares fit and are revealed through the chi-square values. Figure 4.6 shows the average chi-square values for 2009 as a function of altitude and latitude. Comparing Figure 4.6 to Figure 3.8, it is evident that large chi-squared values are strongly correlated with the observed instrument biases. This indicates that the temperature bias between the measurements is systematically impacting the quality of the fit.

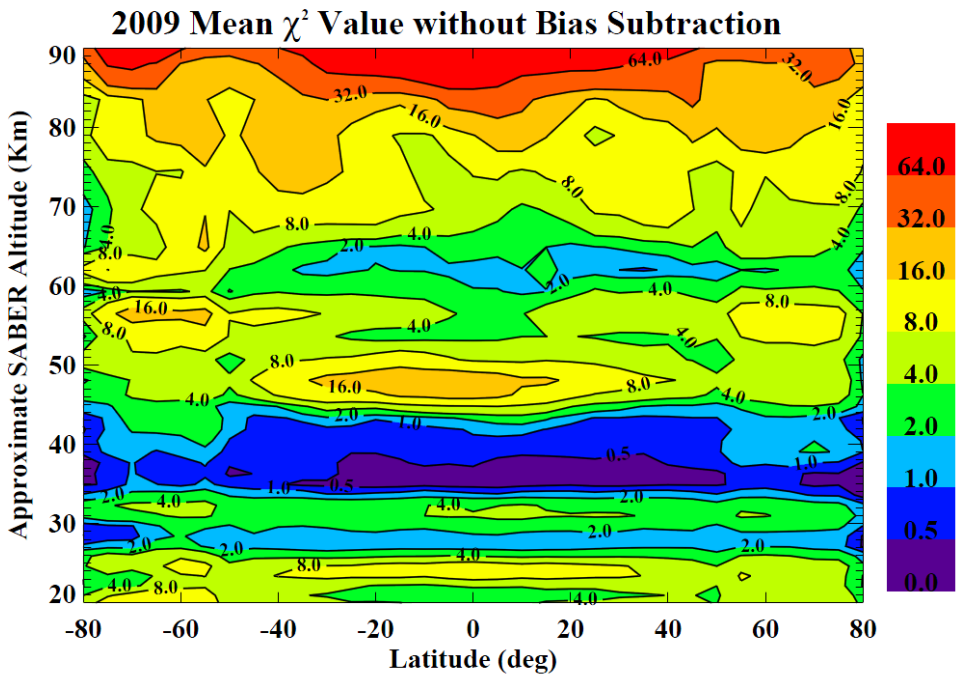

Figure 4.6: Mean chi-square value before bias subtraction as a function of altitude and latitude. The results show average chi-square values for 2009.

The errors introduced by the measurement biases can be reduced by removing the biases from the data. Studies from *Schwartz et al.* [2008] have shown that the MLS temperature data set exhibits a similar cold bias with respect to most other instruments. In contrast, SABER data validation studies [*Remsberg et al., 2008*] have concluded smaller and more diverse biases with other instruments Based on these considerations, the SABER temperatures are used as the reference value for this study.

As explained in the previous chapter, the average measurement differences between MLS and SABER for 2009 were computed by differencing zonally averaged profiles at common locations and local times. The average measurements differences were then sorted as a function of altitude, latitude and the MLS orbit half (ascending or descending). In order to remove the measurement biases, the yearly averaged differences are used to correct the MLS data set. As a

result of the adjustment, the average annual differences between the SABER and MLS data sets are equal to zero.

The effect of the bias correction to the MLS data set on the chi-square value of the least squares fits is prominent in Figure 4.7. The chi-square values are reduced at all altitudes and latitudes, indicating a better fit to our model of a daily zonal mean and MDT. However, large chi-square values are still present at high altitudes in the upper mesosphere region. The large values are partially caused by measurement differences that vary greatly from the average difference. Biases ranged from ±20 K at altitudes above 90 km, which are significantly larger than the biases at lower altitudes. A larger bias range decreases the chance of applying the correct bias and increases the probability of obtaining fits with larger chi-square values.

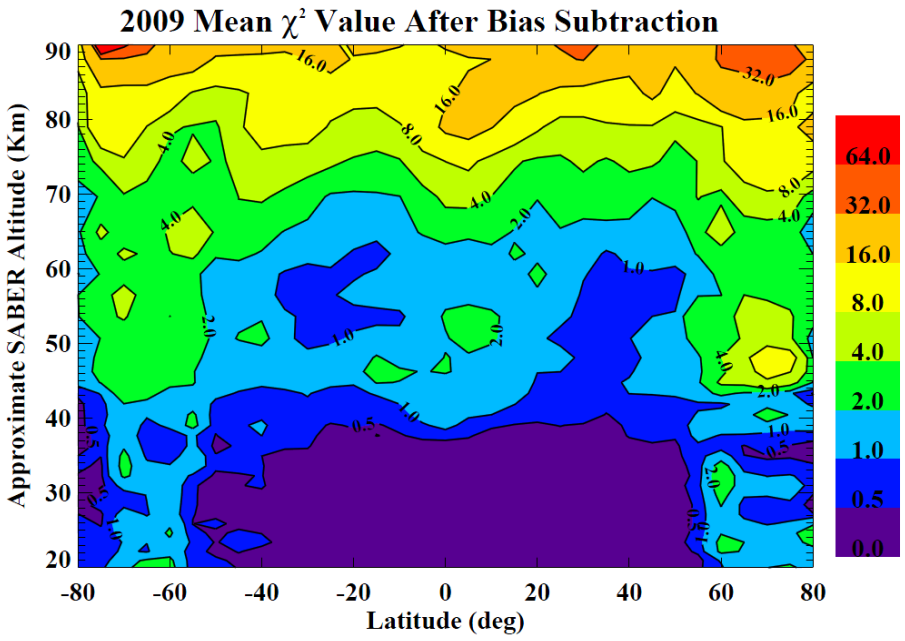

Figure 4.7: Mean chi-square value after bias subtraction as a function of altitude and latitude. The values have been reduced at all latitudes and altitudes.

In addition to measurement error, large chi-square values at high altitudes are likely caused by the effects of other tidal components and dynamics in the atmosphere that are not modeled. Like the MDT, the amplitudes of planetary waves and tides grow with increasing altitude and decreasing density. Any tides that are not filtered by zonal averaging or the solar local time sampling can introduce error in the fit if the tides are also sufficiently large and the sampling is poor. It is observed in Figure 4.7 that the inability to eliminate instrument biases and the errors introduced by larger tides at higher altitudes correlate with larger chi-square values. Moreover, it can be seen that the chi-square value begins to increase rapidly with altitude at around 85 km, which is about the altitude where the MLS data quality decreases rapidly. It is concluded that for altitudes above 85 km, the measurement errors and the effects of other tides are too great to achieve meaningful least squares fits for the MDT. Thus, the final results of this analysis are limited to altitudes below 85 km.

4.3 Condition Number

The condition number of a nonsingular matrix is defined as the ratio between the largest and smallest singular value. A matrix with a large condition number is labeled as ill-conditioned. The condition number is calculated from the system matrix (of size [4x3] in this study) and is solely dependent on the sampling in solar local time. Fits that are determined from evenly-spaced samples in solar local time will have a low condition number while high condition numbers arise when the solar local times are poorly sampled. Figure 4.8 displays some examples of poorly sampled least squares fits.

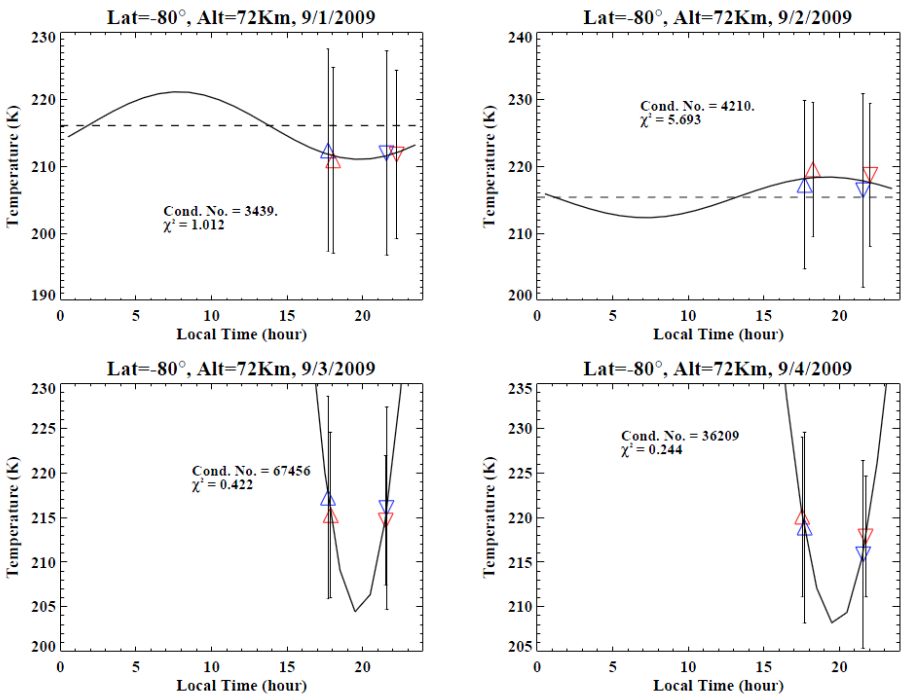

Figure 4.8: Examples of ill-conditioned least squares fits. Poorly spaced samples in solar local time can result in erroneous results for the MDT.

Since the condition number is only dependent on solar local time sampling, it is directly related to the precession of orbit of the TIMED satellite. The condition number will vary over the course of a yaw cycle as the orbit precesses through all solar local times. The effect of the orbital precession is exhibited in Figure 4.9.

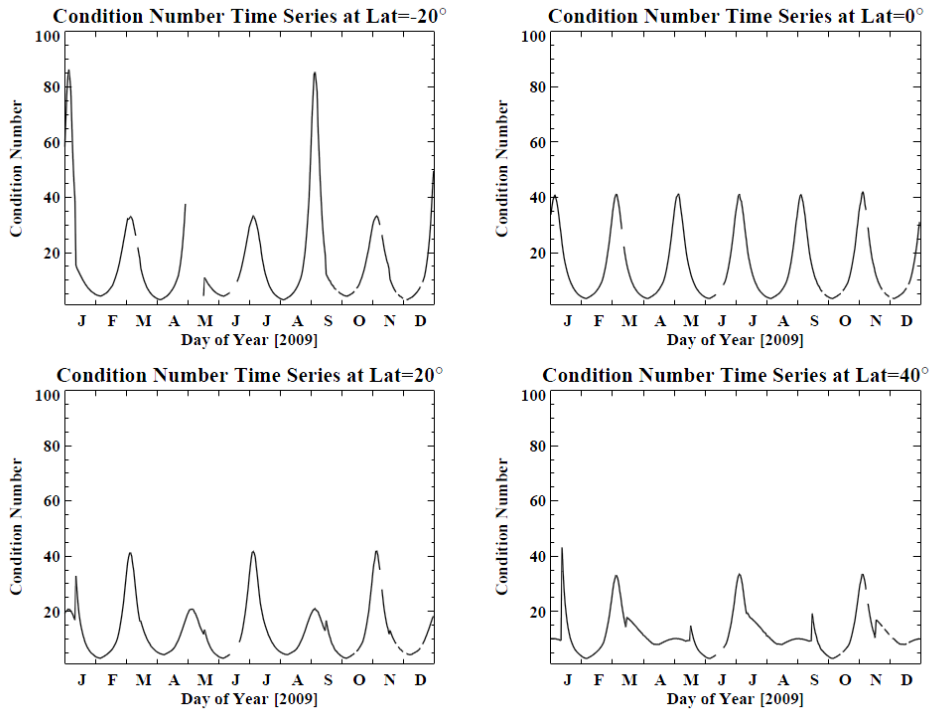

Figure 4.9: Condition number for 2009 at selected latitudes. The condition number is dependent on the TIMED yaw cycle.

High condition numbers arise when measurements are made at nearly identical solar local times. In such situations, information is essentially only given at three or fewer solar local times instead four solar local times. Systems with high condition numbers can almost be considered as linear dependent, which means the system solutions (amplitude and phase) are highly sensitive to small changes to the input (temperature). An example was previously explained in Figure 4.3 where poor sampling allowed the effects of the semidiurnal tide to impact the MDT estimates.

To determine the effect of large condition number systems on the amplitude results, a simulation is performed. For each fit at the equator, the four zonal temperature averages are randomly varied between ± 1 K of the actual value assuming a Gaussian distribution. The daily zonal mean, amplitude and phase for each trial are determined from the random temperature values and the least squares fitting. An example of a simulation is shown in Figure 4.10.

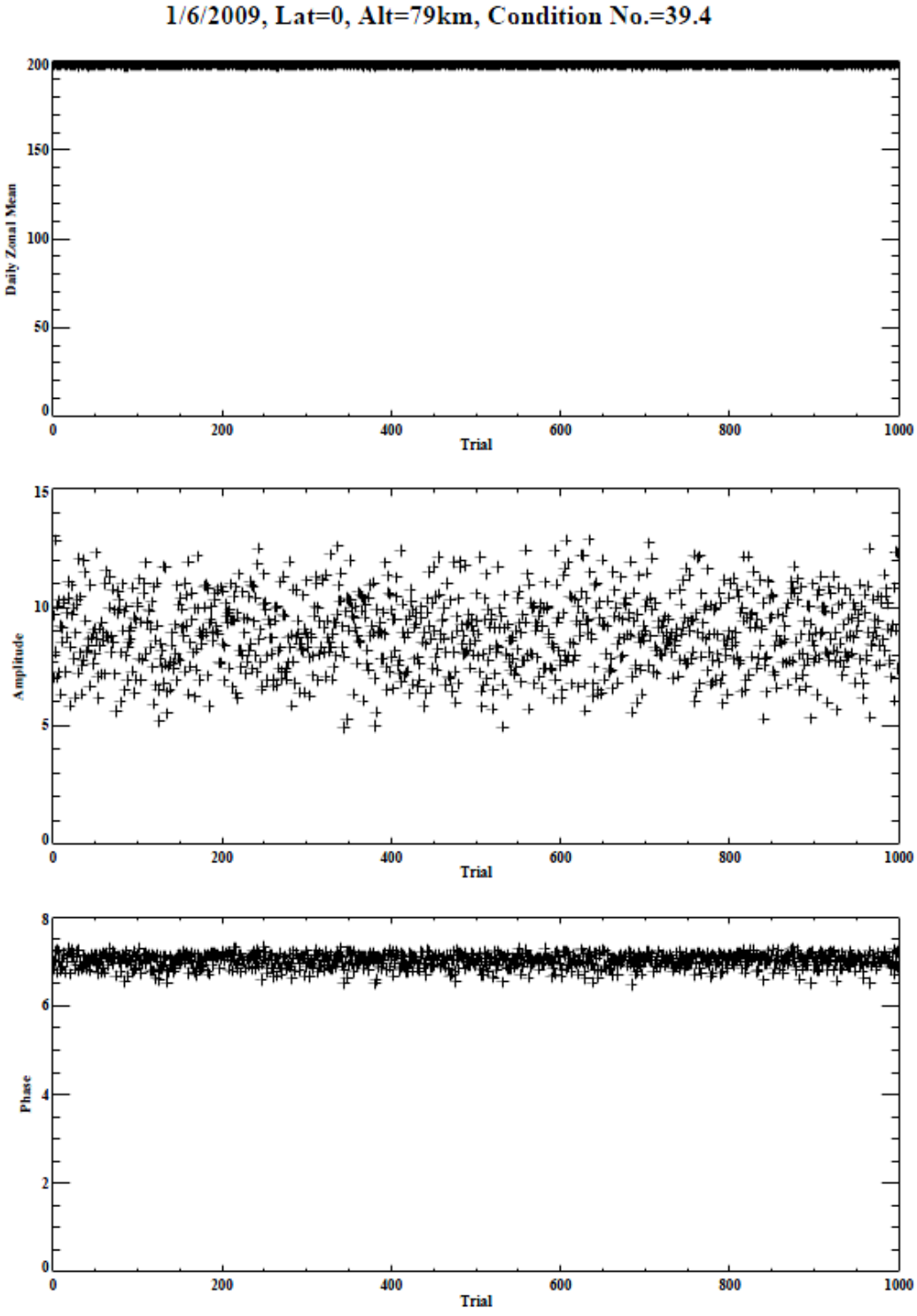

Figure 4.10: Example of a simulation for MDT results. For this case, the four zonal averages were randomly varied between ±1K for 1000 trials assuming a Gaussian distribution. The results for the daily zonal mean, amplitude and phase for the MDT are displayed.

The standard deviation of the amplitudes obtained from the trials is calculated for each fit at the equator in 2009. Figure 4.11 displays the relationship between the standard deviation of the output amplitudes and the condition number of the least squares fit. The simulation results for each case are also displayed by mean amplitude to show that the mean amplitude has little impact on the simulation results.

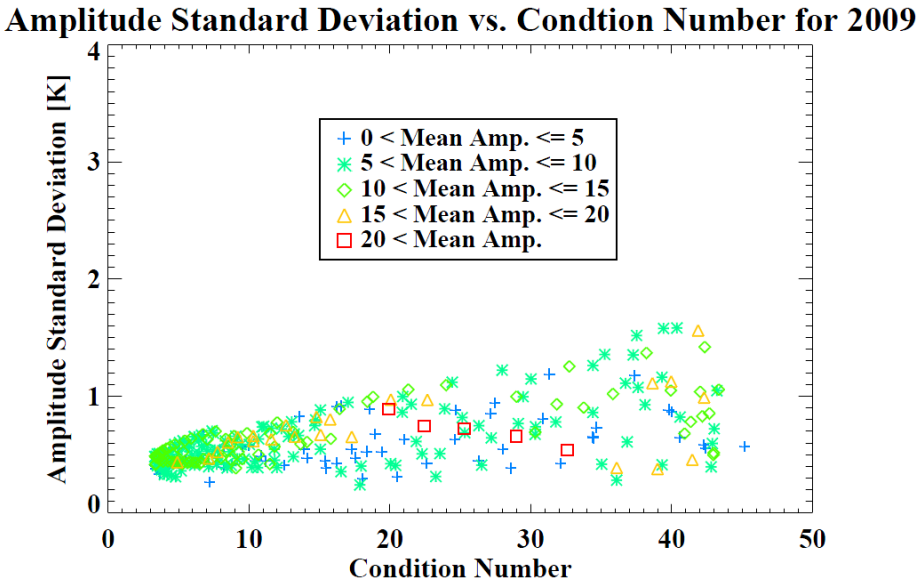

Figure 4.11: Amplitude variability vs. condition number for the simulation. The amplitude standard deviation for each of case at the equator for 2009 are shown in the plot.

The results of the simulation show that small changes in temperature for high condition number systems can lead to more varying amplitude solutions. However, the simulation results also show that high condition number systems do not always result in a wide range of solutions. A clear cutoff condition number, therefore, cannot easily be established. The most important conclusion from the simulation is that the least squares solutions obtained from high condition number systems are not as robust to small changes in temperature. One should be cautious when

interpreting the results obtained from high condition number systems as they may be impacted by small errors in temperature instead of geophysical processes.

4.4 Summary

Estimates of the MDT are obtained by fitting a sinusoid to zonally averaged temperatures at four solar local times. The effects of non-migrating tides and planetary waves are reduced significantly by averaging multiple orbits at constant solar local time. Of the migrating tides, the semidiurnal tide has the most potential to impact the MDT due to its large tidal amplitude in the MLT region. However, the effects of the semidiurnal tide is dramatically reduced by the least squares approach with one degree of freedom if the solar local time is properly sampled.

An important diagnostic is the chi-square value, which is a summation of the square of the residuals. Chi-square value is dependent on imperfections in the model including instrument biases, measurement noise, and effects of un-modeled signals such as tides and waves that are not eliminated. The chi-square value determines the quality of the fit and can be utilized to filter out results of poor quality. In this analysis, solutions that were determined from less than eight orbits of data were generally accompanied by large chi-square values. Thus, these solutions are considered inadequate in solely representing the MDT and not utilized for scientific interpretation. Large measurement biases were also found to strongly correlate with large chi-square values. In order to reduce the error caused by instrument biases, yearly averaged differences between the instruments were applied to the MLS data set. The errors due to measurement error and un-modeled effects that contribute to the chi-square value can dramatically affect the results when the condition number is large due to poor sampling. However, condition number is not used to filter any results and is instead employed to help interpret the validity of the final results in the next chapter.

Chapter 5

FINAL RESULTS AND DISCUSSION

The final results describing the features of the MDT are presented in this chapter to assess the feasibility and scientific validity of the estimation method described in this thesis. Results for 2009 on both a daily and yearly scale are displayed and analyzed to conclude the method's advantages and limitations. A comparison of the results to those of a past study is also performed. Finally, a wavelet analysis is conducted to illustrate the estimated long term and short term variations of the MDT.

5.1 Daily Results

By implementing the method described in Chapter 4, the daily zonal mean, amplitude, and phase of the MDT are estimated for each day, latitude and pressure level between 20 and 85 km. Results for selected days throughout 2009 are displayed in this section and analyzed. Two low condition number cases and one high condition number case are presented. Overall, the three cases presented in this section serve to illustrate the factors that influence the quality of the results

As explained in Chapter 4, a low condition number system is one that is well-sampled in solar local time. The results derived from low condition number systems do not drastically change due to small temperature deviations. Estimates for the MDT and the daily zonal mean

over the observable latitudinal range and the practicable vertical range for two selected days with predominantly low condition numbers are displayed in Figure 5.1 and Figure 5.2.

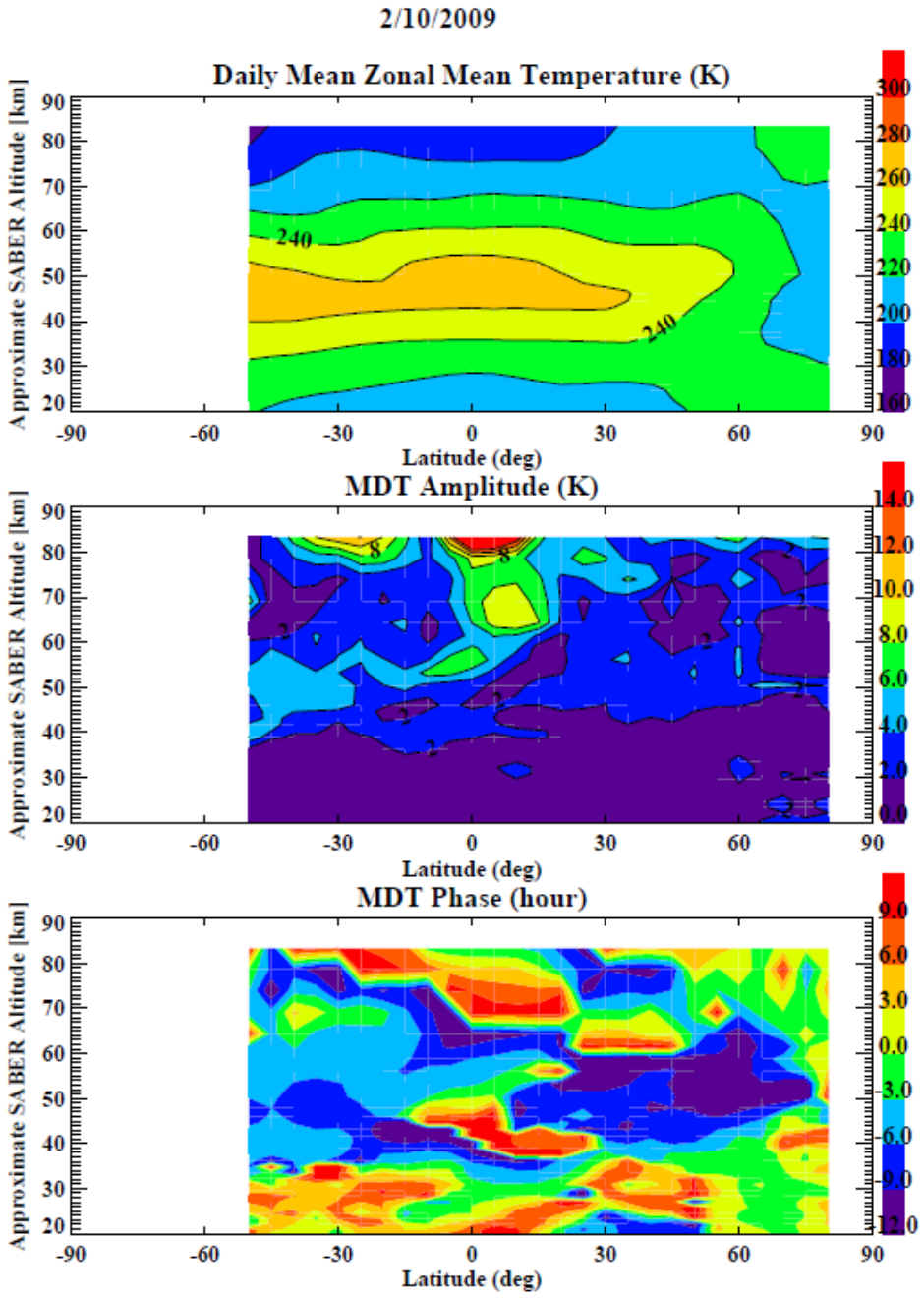

Figure 5.1: 2/10/2009 Results for the daily zonal mean and MDT as a function of amplitude and phase.

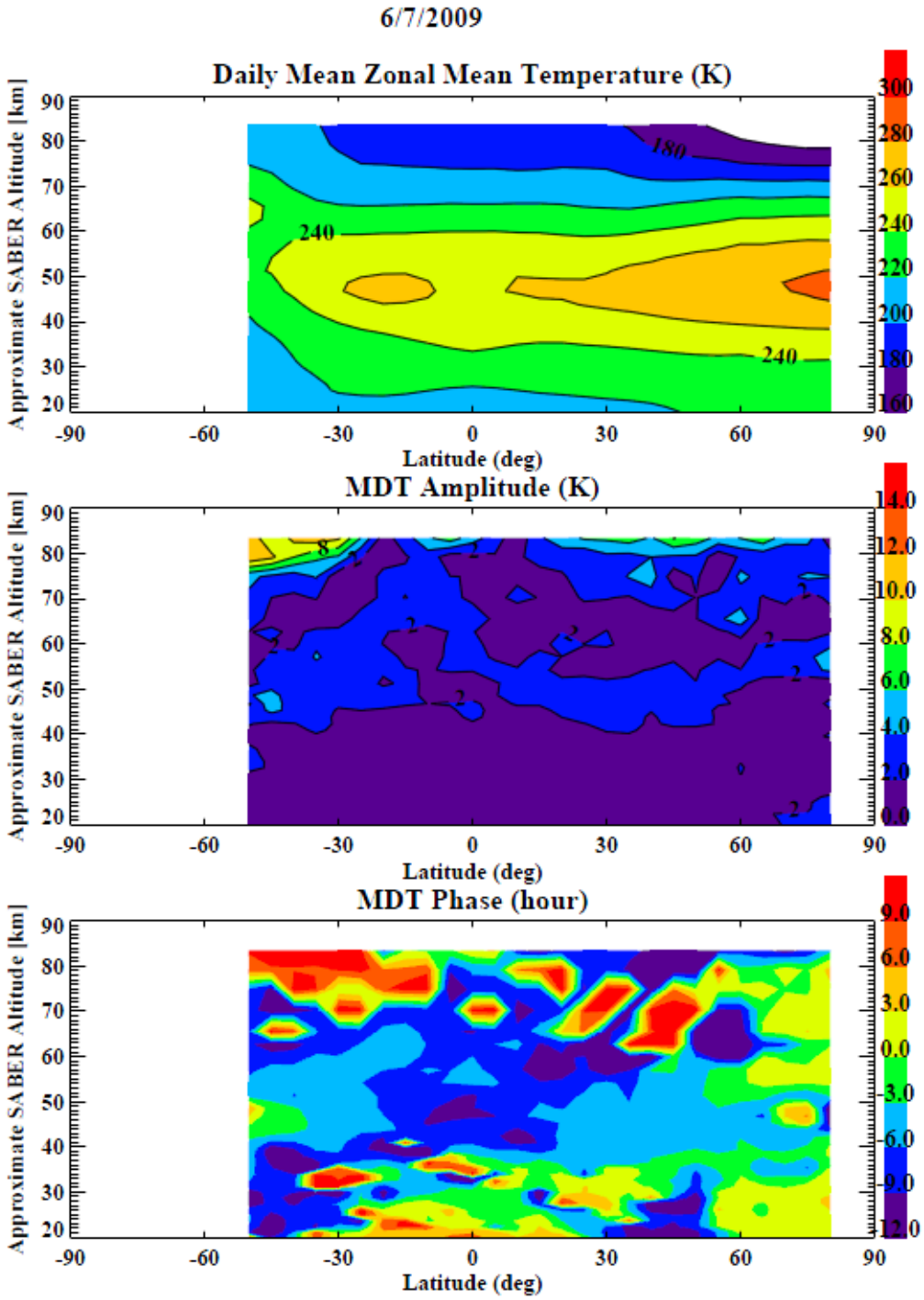

Figure 5.2: 6/7/2009 Results for the daily zonal mean and MDT as a function of altitude and latitude.

The results for the 2/10/2009 case shown in Figure 5.1 resemble the theoretical predictions and past observations. The estimates for the daily zonal mean, representing the background temperature, is displayed in the top plot in the figure. It is recognized from the middle plot of Figure 5.1 that the MDT amplitude generally increases with altitude as expected due to the conservation of energy. The amplitude for this case reaches a maximum value in the upper mesosphere at the equator. It also attains a secondary peak value in the upper mesosphere at -30° latitude. Although the absence of an equally large peak value at 30° deviates from the (1,1) Hough mode predictions for the MDT, observations of the hemispheric asymmetry have been made in the past [*Vincent et al.*, 1988].

There are several regions where the amplitude does not increase with altitude, which might be influenced by un-modeled effects. For a clearer illustration, the MDT results at the equator are shown in Figure 5.3.

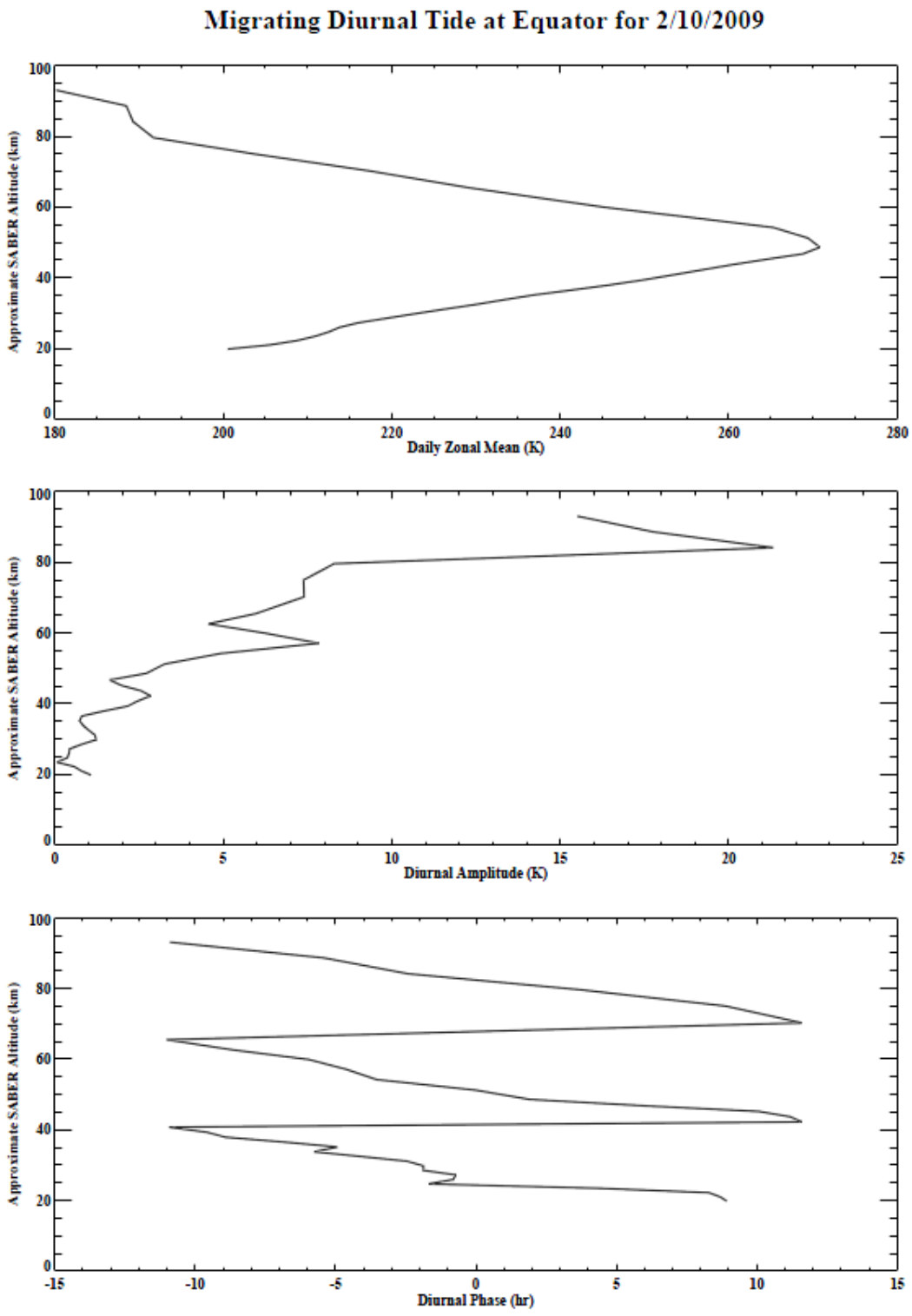

Figure 5.3: Daily zonal mean and MDT results for 2/10/2009 at the equator as a function of altitude. Results are shown above 85 km to display the decreased quality of the results at high altitudes.

The two most apparent regions where amplitude does not increase with altitude is the 55-60 km and the 85-95 km vertical ranges. The effects from migrating tides, non-migrating tides and planetary waves can impact the amplitude results if the MDT is not properly sampled. Although instrument biases were removed, residual differences between the measurements can also affect the accuracy of the results. Instruments biases between 2-4 K in the 55-60 km region and 10-20 K at altitudes above 85 km were estimated in the comparative study presented in Chapter 3. Inability in removing these biases from the MLS data set can influence the estimates.

Results for the MDT phase at the equator shown in the bottom plots of Figure 5.1 and Figure 5.3 are similar to theoretical predictions and observations [*Chapman and Lindzen*, 1970; *Oberheide and Gusev*, 2002; *Mukhtarov et al.*, 2009]. The phase plot in Figure 5.3 exhibits a steady phase progression with height as expected. The vertical wavelength (length of one wave cycle) can be estimated from the phase results. For the 2/10/2009 case, the vertical wavelength is about 25 km, which is large compared to past observations of the MDT (~20-25 km). Vertical wavelength estimates over the course of a year are displayed later in the chapter.

In general, the MDT results for the 6/7/2009 case shown in Figure 5.2 feature smaller amplitudes than the results for the 2/10/2009 case. These results are expected due to the semiannual periodicity of the MDT, characterized by large amplitudes near the equinox and small amplitudes near solstice. The exception is observed at altitudes above 80 km and at latitudes between -50° and -30° where the amplitudes are comparable to the 2/10/2009 case. The exceptions are not surprising since the results for altitudes above 80 km are susceptible to remaining measurement errors. In addition, the anomalous amplitudes might be caused by the inability to eliminate the migrating semidiurnal tide when it is large due to poor sampling. Tidal theory predicts large migrating semidiurnal tides at higher latitudes [*Forbes et al.*, 1995]. Furthermore, the condition number at 50° latitude for this day is above 100, indicating poor

sampling. Thus, sources of error such as the semidiurnal tide and remaining instrument errors can have a large impact on the MDT amplitude.

The phase progression with altitude is not as apparent in the 6/7/2009 case and is most likely a result of smaller amplitudes throughout global structure. Tides with smaller amplitudes are more susceptible to phase errors. To illustrate this, consider the case when the MDT is sampled at the peak, trough, and two zero points as displayed in Figure 5.4. Since the amplitude is small (1 K), only a 2 K error in two points is required to change the phase by 180°. Although this exact case is not likely to occur in the results, it does show that relatively small error can alter the phase of small tides.

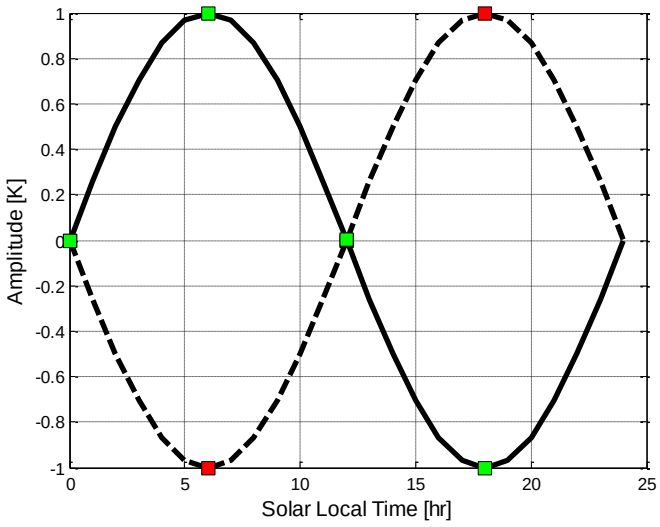

Figure 5.4: Phase change due to error illustration. Green markers represent accurate zonal averages for each phase of the MDT. Red markers represent erroneous zonal averages. The true tide is displayed as a solid line, while the tide derived from erroneous zonal averages is displayed as a dashed line.

The condition number for the 2/10/2009 and 6/7/2009 cases is low throughout most latitudes. However, there are portions of the year where the condition number is high. The

selected day presented in this section contains high condition numbers at most latitudes. The results are displayed in Figure 5.5.

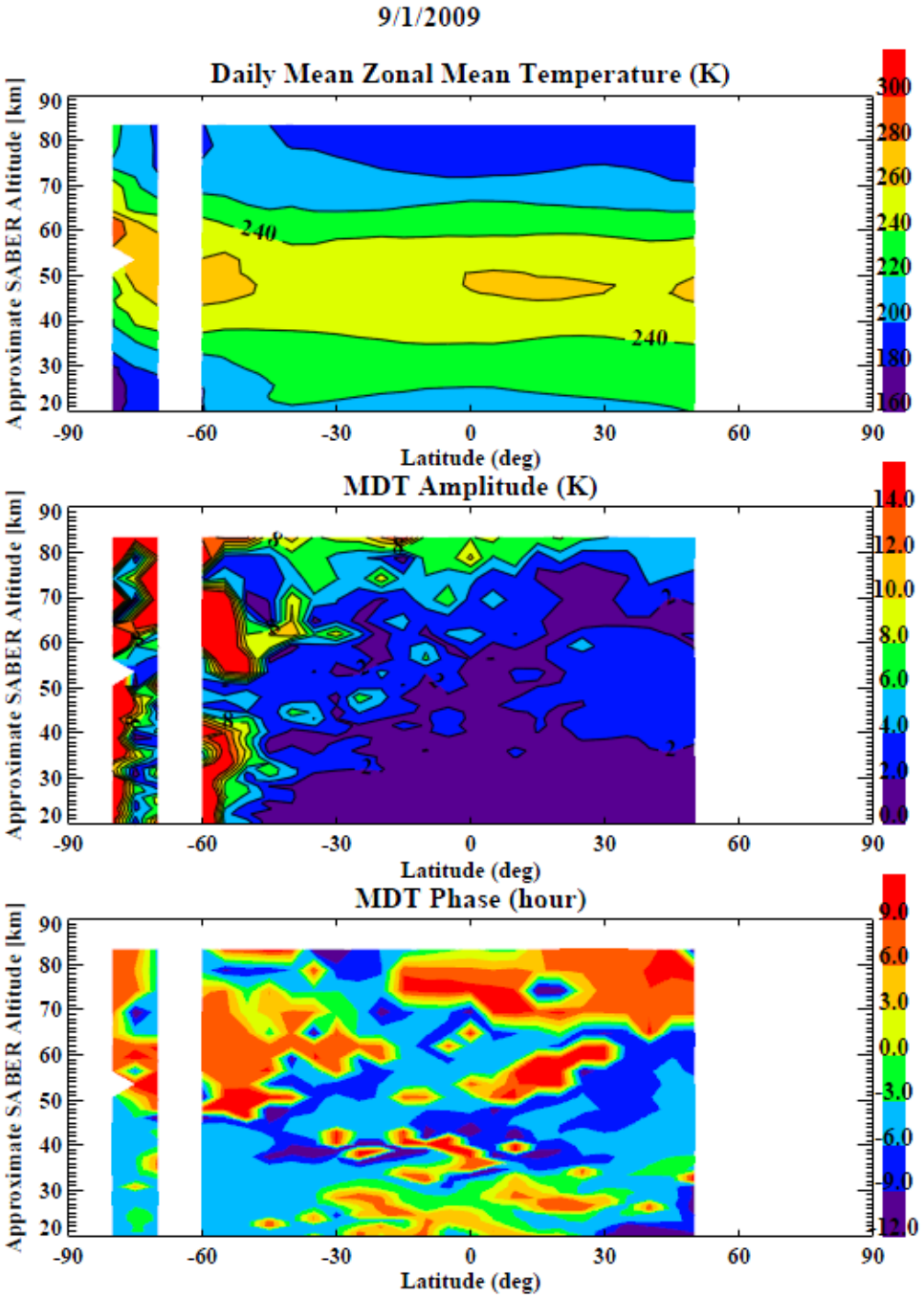

Figure 5.5: Daily zonal mean and MDT results for a bad condition number case. The data gap at -65° and 60° is caused by filtering out results that were derived from 8 orbits of data or less.

From Figure 5.5, the impact of poorly sampled temperatures in local time is apparent at the high latitudes in the southern hemisphere. Amplitudes range from near 0 K to greater than 14 K with no apparent trend with altitude for these latitudes. The condition numbers for this day at the high, southern latitudes exceeded 200 as seen in Figure 5.6 and are the most likely cause for the erroneous results. In contrast, the northern hemisphere contained low condition numbers for this day (Appendix B). Consequently, reasonable results are observed at these latitudes.

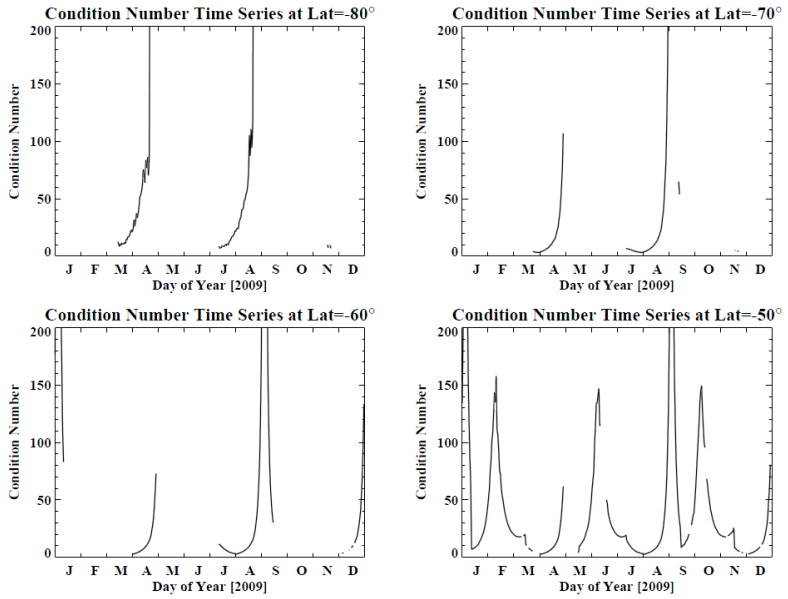

Figure 5.6: Condition number vs. day of year in 2009 for latitudes between -80° and -50°.

5.2 Yearly Results

In this section, the MDT results are displayed over the course of the year to check if the results resemble theory and observation, and also diagnose the impact of certain factors on the results.

5.2.1 Amplitude Results

The median MDT amplitude for selected latitudes between 75 and 85 km is plotted over a year in Figure 5.7 and Figure 5.8. The condition number and median chi-square value between 75 and 85 km are also displayed for each day.

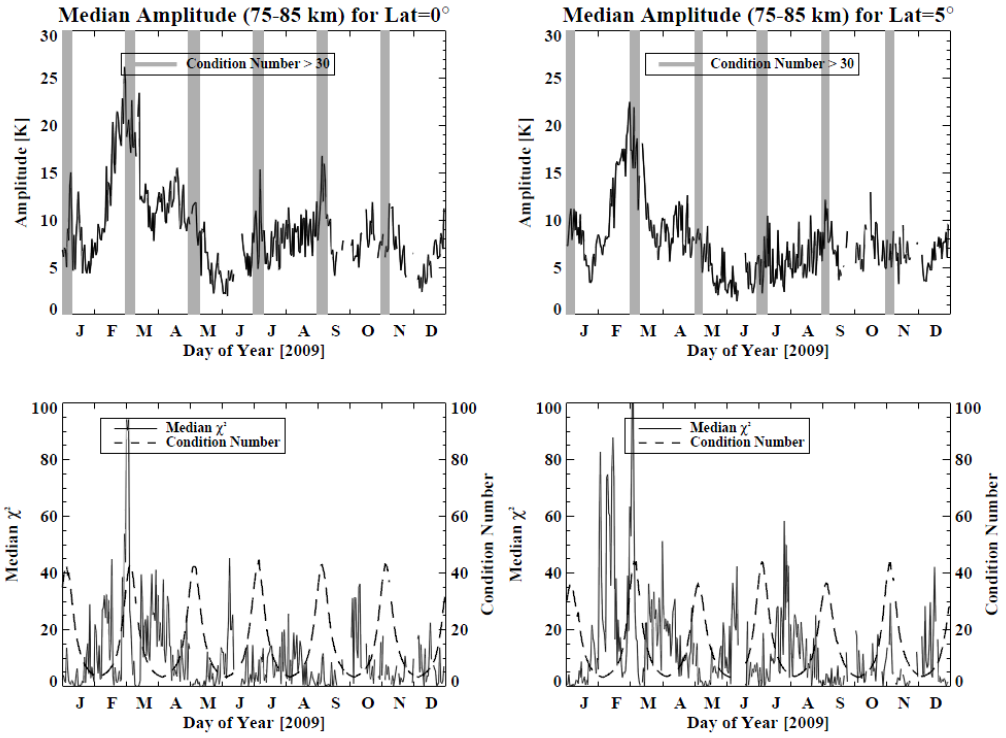

Figure 5.7: 2009 MDT amplitude time series for 0° and 5° latitude. The top plots show the median MDT amplitude between 75 and 85 km for each day in 2009. The bottom plots show the condition number (dashed) and chi-square value (solid) over 2009.

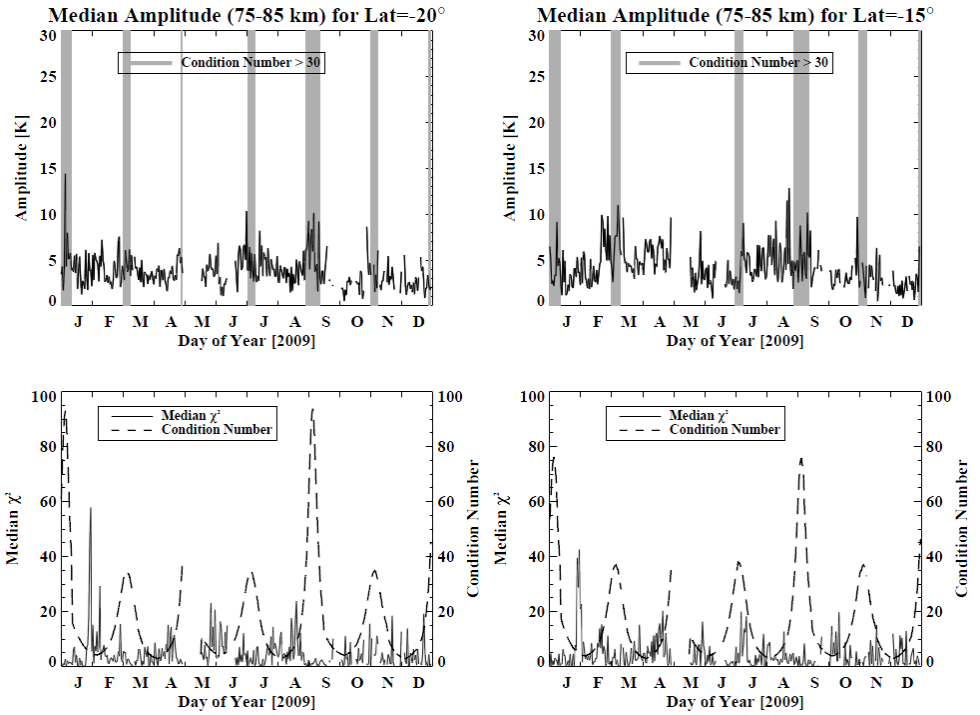

Figure 5.8: 2009 MDT amplitude time series for -20° and -15° latitude. The top plots show the median MDT amplitude between 75 and 85 km for each day in 2009. The bottom plots show the condition number (dashed) and chi-square value (solid) over 2009.

The MDT amplitudes for 2009 show both short term and long term variations, which agrees with the results from past studies. For the 0° and 5° latitude cases, the semiannual oscillation with amplitude peaks near the equinox periods dominates the long term variations. The amplitudes reach maximum values during late February and early March, and minimum values near the solstice periods. Shorter term variations are also apparent. As shown in Figure 5.9, the mean day-to-day variation in the MDT amplitude is 1.84 K. The minimum and maximum amplitude differences between adjacent days are about 0 K and 12 K, respectively. Through a Hough mode analysis of satellite (UARS-HRDI) wind data, *Burrage et al.*, [1995] also observe significant day-to-day changes in the meridional wind of 25 m/s and greater (Figure 2.3). The results presented here provide further evidence that drastic changes in the diurnal

amplitude can exist at certain times of the year and highlight the importance of analyzing the short term variations of the MDT.

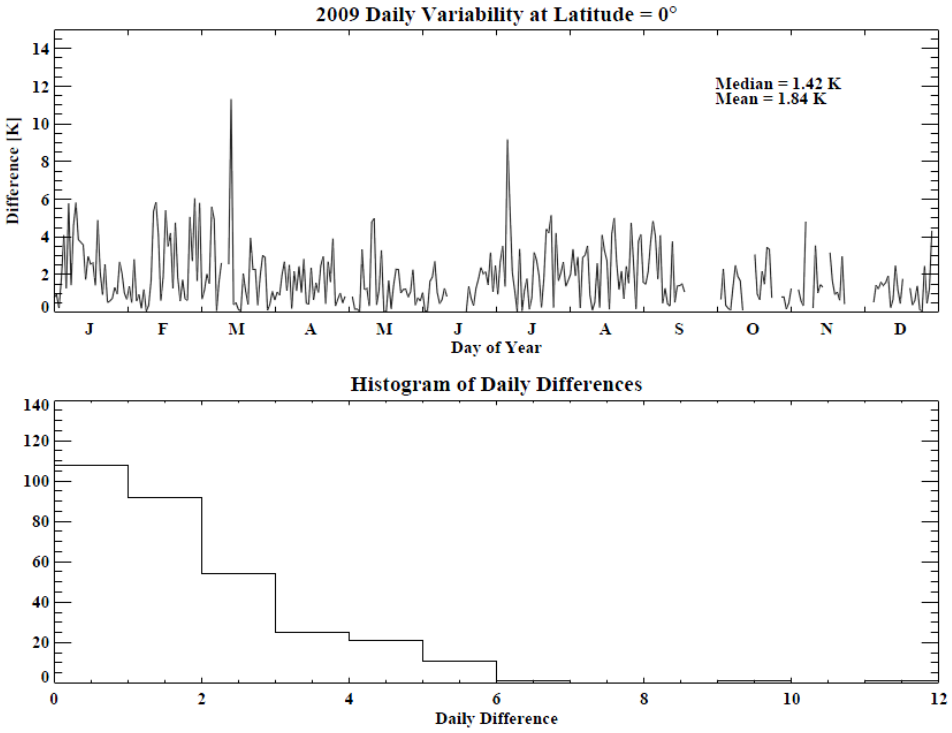

Figure 5.9: MDT daily variability at the equator and the 75-85 km altitude range. The magnitudes of the day-to-day changes in amplitude are shown in the top plot. A histogram of the daily differences are shown in the bottom plot.

The (1,1) Hough mode latitudinal structure can be observed by analyzing all four latitude cases. Amplitudes are largest at the equator and only slightly less in magnitude at 5° latitude. The results are much smaller at -20° and -15° latitude, agreeing with theoretical predictions. Moreover, the results for the -20° latitude case might approximate a "noise floor" for the MDT results. The long term variations that are apparent near the equator are almost non-existent at -20°. This could indicate that the MDT amplitudes for this case are small enough to be dominated

by errors due to measurement error and other un-modeled tides and waves, which constitute the "noise floor" in our approach.

Plotting condition number and median chi-square values is performed to illustrate the effects on the results. Regions of large condition number are shaded in the top portions of Figure 5.7 and Figure 5.8 to warn of potential erroneous results. Condition number seem to significantly impact the results when it is larger than 80. As seen in the -20° latitude case, the amplitudes suspiciously vary by 5-10 K when the condition number is larger than 80. Large variations are not expected because the MDT amplitude is small and most likely below the noise floor at this latitude. The variation during times of high condition number is also significantly larger than the variation throughout the rest of the year. Thus, it is likely that the poor sampling is affecting the results by producing a large range of possible least squares solutions.

The influence of large chi-square values on the amplitude results is not as apparent as the impact of large condition numbers. The largest chi-square values for all cases occur during late January and early February at 5° latitude. These values could be caused by the presence of other tides and waves that are not effectively filtered out or measurement error. However, the impact of the large values on the results is not clear. Although the chi-square values at 0° latitude are much smaller than the values at 5° latitude during the late January-early February time frame, the time structure of the MDT amplitude is almost identical in both cases as predicted by theory. This situation supports the supposition that the amplitude least squares results are robust to error when the condition number is adequately small.

It should be noted that there is a slight, expected correlation between condition number and chi-square value. Because large condition numbers occur when two or more local time samples are almost identical, the residual values between the temperature points and the fitted least squares value will likely be smaller. Therefore, the chi-square values will likely be smaller

when the condition number is large. The main consequence of this correlation is that the chi-square value should not be interpreted as an absolute measure of the error sources. For example, the small chi-square values associated with the large condition numbers during late August is not necessarily an indication of small error, but could be a result of incorrect solutions that fit the data well.

5.2.2 Phase Results

The phase results at 80 km for 2009 are shown in Figure 5.10 for selected latitudes. Regions of high condition number are shaded in blue and red.

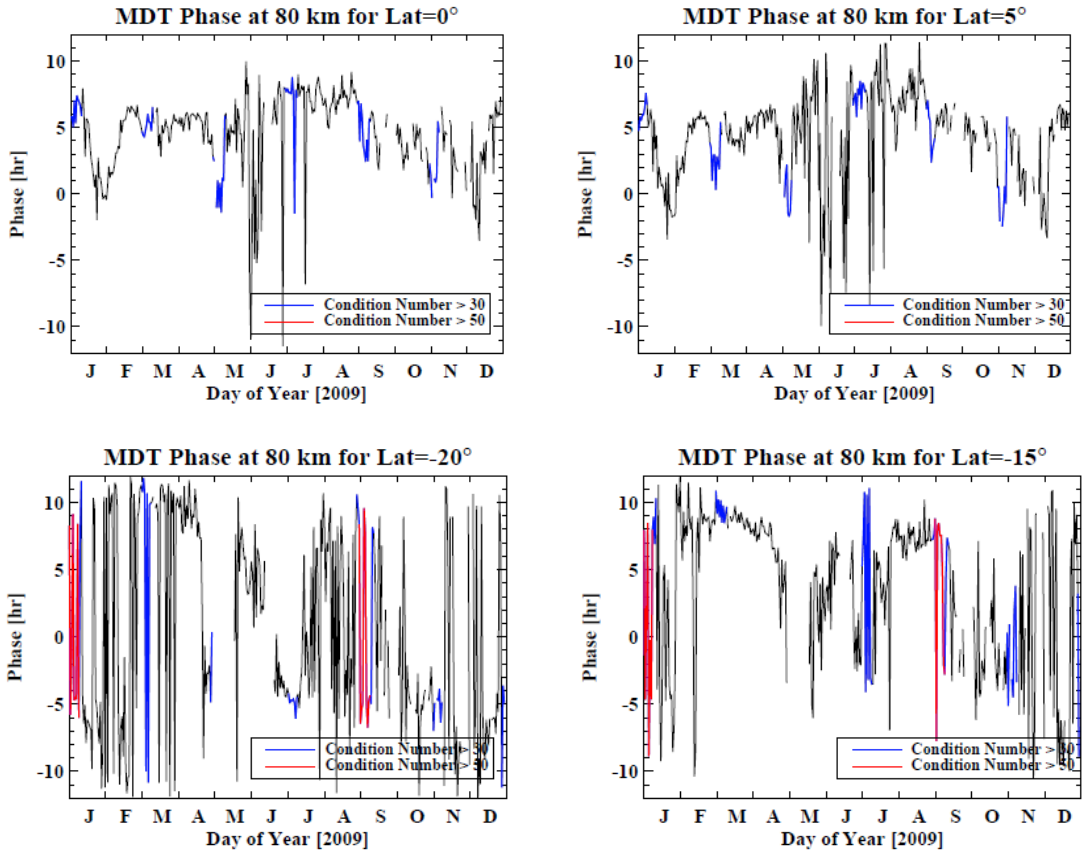

Figure 5.10: 2009 MDT phase time series at 80 km for selected latitudes. Results derived from high condition number systems are highlighted in blue and red.

The 80 km MDT phase results at the equator are relatively consistent about a mean of ~5 hr and exhibit slight short term and long term variations. A study by *Mukhtarov et al.* [2009] employed a least squares method using 60 days of SABER data to estimate the MDT amplitude and phase. *Mukhtarov et al.* [2009] also observed relatively stable phases at a given altitude and latitude over time periods less than a year, which provides confidence that the phase results at the equator are fairly accurate for most of the year. However, there are instances near the summer solstice where the phase results deviate drastically from the mean. Although these phase results could be caused geophysical processes, they are most likely impacted by the small MDT amplitudes during the period. As explained previously, least squares fits for days when the amplitude is small are prone to errors in phase. This claim is supported by the results for the -20° latitude case where the MDT amplitudes are smallest. The phase results vary greatly over short time periods and do not exhibit any consistent mean. It is concluded that phase results are most accurate when the MDT amplitudes are large and are least accurate when the MDT amplitudes are small.

The vertical wavelength can be estimated from the phase results for each day. The process begins by unwrapping the phase for each day and latitude to view the progression as a function of altitude. A line of best fit relating phase and altitude is then determined and utilized to estimate the vertical wavelength between 20 and 85 km. A correlation coefficient (r^2 value) is used to determine the degree of correlation between the unwrapped phase and altitude. Since small r^2 values indicate weak phase progression with altitude and possibly erroneous results, vertical wavelength estimates that were obtained from r^2 values of less than 0.9 were omitted. Moreover, the vertical wavelengths were only computed at the equator over the course of 2009 because the phase results are susceptible to error when the amplitude is small. The vertical

wavelength estimates are shown in the top plot of Figure 5.11 and are accompanied by error bars. Each error bar represents the square root of the χ^2 value for each line of best fit.

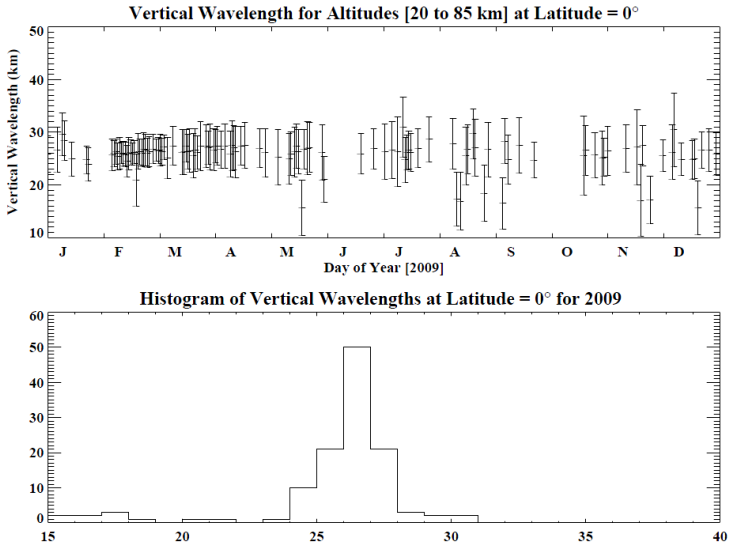

Figure 5.11: Migrating diurnal tide vertical wavelength estimates for 2009 at the equator. The error bars associated with each vertical wavelength estimate is a measure of the residual error from the line of best fit relating the unwrapped phase and altitude.

The vertical wavelength estimates display an approximately symmetric distribution with a mean around 26 km. Although the mean lies slightly outside the ~20-25 km wavelength range that was estimated from past observational studies (see Chapter 2), the results are comparable to the 27.9 km wavelength predicted by the (1,1) Hough mode. The relatively scattered distribution about the mean is mainly caused by some inaccurate phase results and vertical wavelengths that change slightly with altitude. The vertical wavelengths for altitudes below 60 km have a mean of about 23 km. In contrast, the results for the 60-80 km altitude range display a mean that is closer to 30 km (Appendix B). The dependence of vertical wavelength on altitude is likely caused by the presence of other propagating modes of the MDT and a non-isothermal background atmosphere (Chapter 2). Other propagating modes have shorter vertical wavelengths (Table 2.1)

and are stronger at lower altitudes before dissipation. Thus, it should be expected that the vertical wavelength of the MDT is smaller at lower altitudes due to the influence of multiple propagating modes. Additionally, the change in scale height with altitude is positive in the stratosphere and negative in the mesosphere. From equation 2.25, it can be predicted that the vertical wavelength will be smaller in the stratosphere, which agrees with the estimates obtained here.

5.2.3 Comparison to *Mukhtarov et al.* [2009]

Mukhtarov et al. [2009] estimated the MDT from TIMED/SABER temperatures by utilizing a least squares fitting technique to spectrally analyze a two-dimensional space-time data set. A 60-day sliding window was used to sample 24 hours in local time, which produces results that are 60-day running averages. The equatorial MDT amplitude and phase results for this study from 2002-2007 are displayed in Figure 5.12. The leftmost plots show the amplitude results over a six year time range. The average seasonal behavior of the amplitude and phase are shown in the rightmost plots.

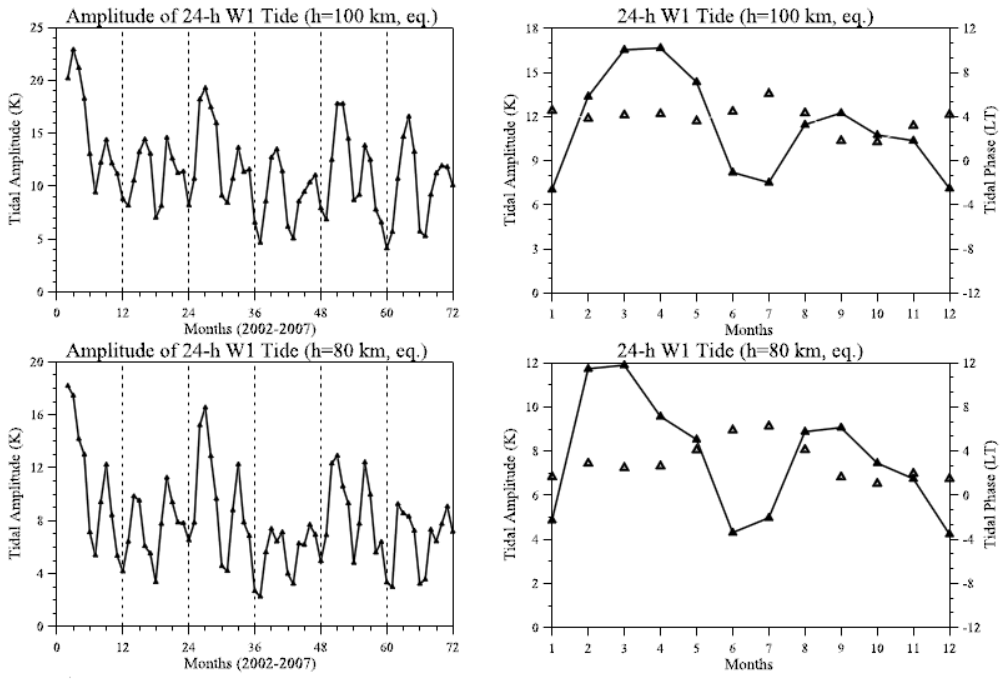

Figure 5.12: *Mukhtarov et al.* [2009] results for MDT. The leftmost plots display the MDT amplitude for every 60 days between 2002 and 2007 at 80 km and 100 km. The rightmost plots display the average amplitudes over this times span. It also displays the average phase as triangles.

For comparison to *Mukhtarov et al* [2009]., the amplitude and phase results from 2005-2007 are generated. Results before 2005 cannot be obtained because the EOS Aura satellite was launched late in 2004. A moving 60-day average is implemented to filter out any high frequency variations. The 60-day mean amplitude and phase results for 2006 are displayed in Figure 5.13. The 60-day mean amplitude results for 2005 and 2007 are shown in Figure 5.14.

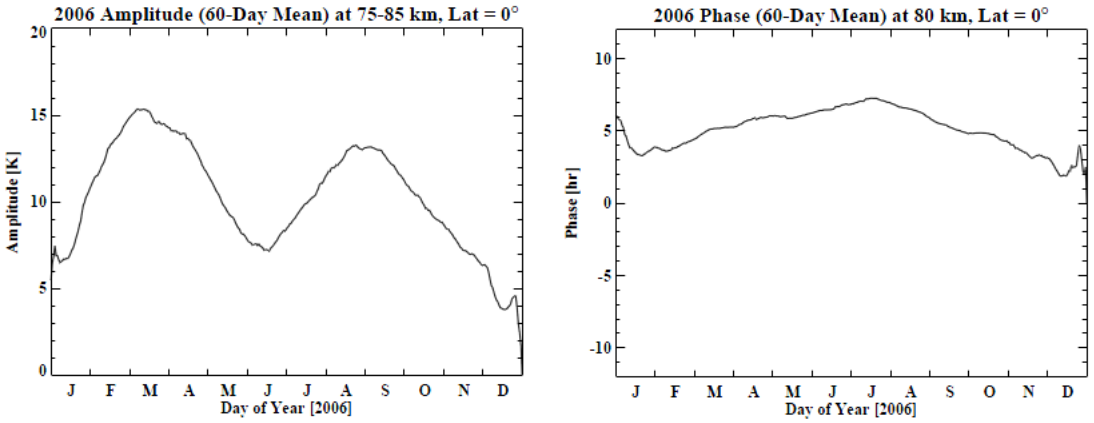

Figure 5.13: 2006 60-day mean amplitude and phase results. The daily estimates for the MDT amplitude and phase were subjected to a running 60-day mean filter for comparison with *Mukhtarov et al.* [2009].

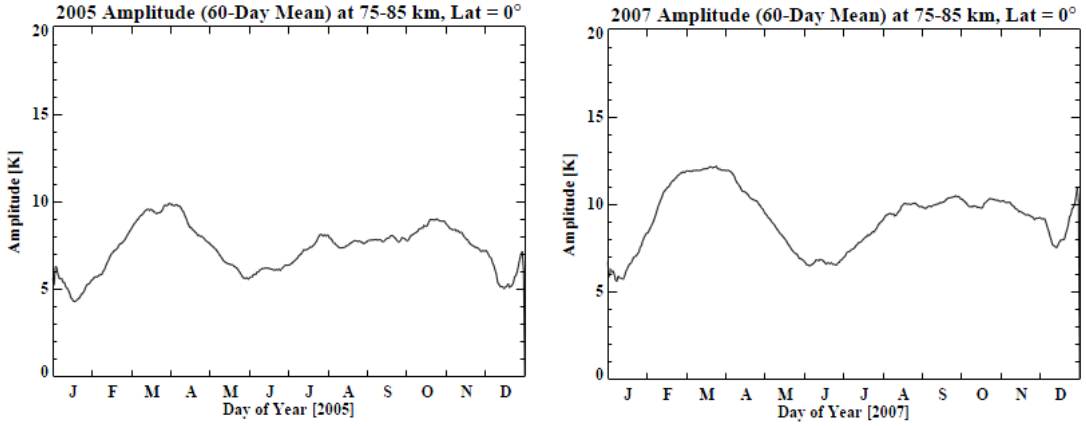

Figure 5.14: 2005 and 2007 60-day mean amplitude results. The daily estimates for these years were also subjected to a running 60-day mean filter for comparison with *Mukhtarov et al.* [2009].

The seasonal amplitude structure displayed in these figures resemble the amplitude trending shown in Figure 5.12, which indicates good agreement between long term variations in the MDT. However, there is a small amplitude bias of about 3 K between the *Mukhtarov et al* [2009] results and the results presented in this study. The bias might be caused by the differences between the two methods. The method of *Mukhtarov et al.* [2009] estimates the amplitudes over 60 days of data and does not take into account phase variation over the time interval. As a result,

any phase variations can manifest as a reduction in the amplitude estimates. Thus, it is not surprising that the amplitude estimates from *Mukhtarov et al.* [2009] are smaller than the estimates obtained in this thesis. Remaining instrument biases in our estimation method might also account for the differences in amplitude. Like the amplitude structures, the 60-day mean phase structure for 2006 is similar to the 2002-2007 average seasonal phase structure shown in Figure 5.12. This provides further evidence that our method provides accurate, long term estimates of the MDT phase at the equator.

5.2.4 Wavelet Analysis of Amplitude

The previous analyses presented in this chapter have shown that the long term variations of the MDT amplitude results are comparable to theory and past observations near the equator and at altitudes and latitudes where the amplitudes are considerably large. The short term variations also seem reasonable when the daily sampling is good (low condition number).

A wavelet analysis decomposes the time series into time-frequency space to determine the dominant modes over the course of a year [*Torrence and Compo*, 1998]. The short and long term variations of the 2009 amplitude time series (75-85 km) are analyzed by performing a wavelet analysis. Before the wavelet analysis is implemented, the mean of the amplitude time series is subtracted from the data and days without any results are set to zero. In addition, data from 2008 to 2010 are used to eliminate edge effects that occur at the beginning and end of the time range. The power spectrum results for the -5° latitude and 0° case are displayed as filled color contours in Figure 5.15 and Figure 5.16. The long period and short period plots are not comparable in magnitude since they are on different scales.

Because missing data can affect the results of the wavelet analysis, a separate mask function is created where days with available data are set equal to zero and days with missing

data are set equal to one. A separate wavelet analysis is performed on the mask function to highlight areas in the time-frequency space that might influence the amplitude wavelet results. The wavelet power is normalized to a maximum of 1 and the minimum contour shown is 0.1 and represented by black contour lines in the following figures.

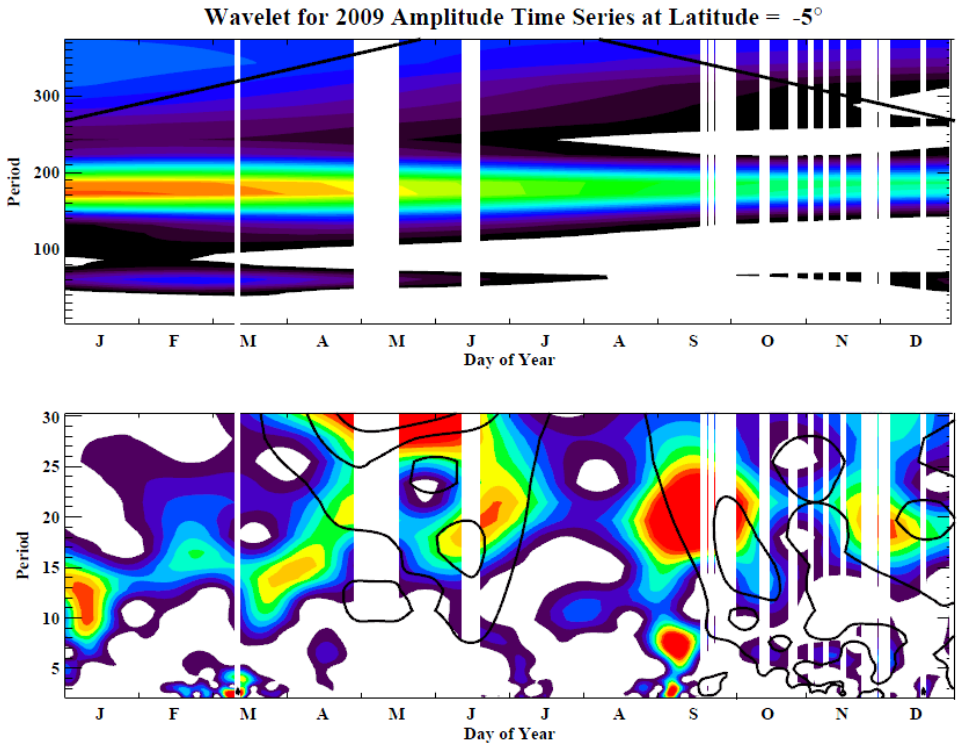

Figure 5.15: Wavelet analysis of 2009 amplitude time series (-5° latitude, 75-85 km). Black contour lines shown in the short period plot represent the wavelet power spectrum of the mask function describing missing data. Contour lines of 10%, 40% and 70% of the maximum value are displayed. The cone-of-influence is shown in the long period plot as a solid black line.

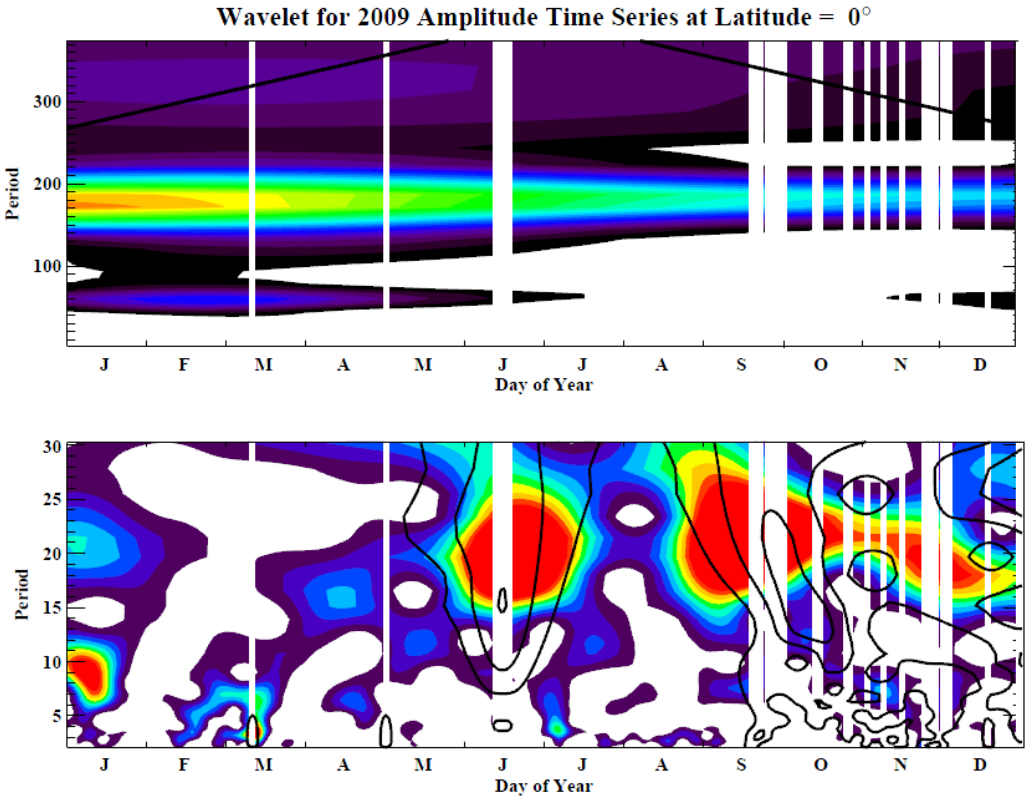

Figure 5.16: Wavelet analysis of 2009 amplitude time series (equator, 75-85 km).

The wavelet analysis displays obvious modes of oscillation that are dominant throughout the year. The semiannual period is the largest mode for both latitudes and is most dominant at the beginning of the year where the amplitudes are largest. A smaller 60-day mode is observed during the first quarter of the year. Smaller variations are also seen at various portions throughout the year. Strong 2-day, 18-day and 23-day periods are apparent in March, June and September respectively. These results might be affected by the missing data during the time periods. A wavelet analysis on the mask function warns that spurious periodicities could be manifested during these times due to missing data. However, there are time spans over the course of the year where there are clear, short term modes of oscillations. For instance, a dominant ~10-day mode is prevalent in January at both latitudes (0° and -5°), while ~2-day and ~8-day modes

are visible in September at -5°. A weaker ~16-day oscillation is apparent at both latitudes in April. Smaller oscillations in areas uninfluenced by missing data are also visible throughout the year. The relatively low condition numbers that exist near the equator and small chi-square values near the time ranges of these oscillations provide confidence that these short term variations are of geophysical origin.

The presence of the aforementioned short term waves and other weaker ones provides some reinforcement to the supposition that the method presented in this thesis has the ability to capture the short term variation of the MDT. The MDT and other tides have been known to fluctuate at periodicities similar to those of other planetary waves existing at the same time [*Chang et al.*, 2011]. Some common planetary waves include the quasi 2-day, 5-day, 10-day, 16-day and 23-day waves [*Xu et al.*, 2007; *Mukhtarov et al.*, 2009]. Indeed, the results obtained here display oscillations similar to those of common planetary waves.

However, the reasons explaining the global structure of the oscillations are not clear. Classical tidal theory predicts that the latitudinal structure is coupled by the Hough modes, which implies variations observed at one latitude should be seen at another on some scale. While there are some instances where the oscillations are prevalent throughout most latitudes (~10-day mode in January), there are other cases where they are not (~2-day mode and ~8-day mode in September at -5°). Moreover, a comparison of amplitudes across latitudes do not display a strict coupling across all latitudes at both long term and short term scales. Further investigation is required to determine why variations in the MDT are occasionally confined at specific latitudes instead of appearing on a global scale.

Chapter 6

CONCLUSIONS

6.1 Summary

A method to explicitly determine the daily features of the migrating diurnal tide (MDT) from two satellite instruments (Aura-MLS and TIMED-SABER) has been presented and analyzed. The main findings and conclusions from this study are summarized by the following.

(1) Before the method was carried out, a comparison between the most recent MLS and SABER data sets was conducted to characterize any potential biases. The comparison revealed that SABER temperatures are warmer than MLS temperatures throughout most altitudes and latitudes except near the 1 hPa pressure level. The magnitude of the bias generally increases with altitude, reaching greater than 10 K in the upper mesosphere-lower thermosphere region. Instrument biases were found to significantly influence the quality of the MDT results and thus, removed from the MLS data set to improve the estimates. Because the biases cannot be effectively removed in the lower thermosphere due to the quality of the MLS measurements, the cutoff altitude range for the results was set to ~85 km.

(2) In addition to instrument biases, an important error source affecting the MDT results is the effect of un-modeled tides and waves. Non-migrating tides and planetary waves are attenuated by the zonal averaging process at constant local time. The ability to attenuate the

effects of non-migrating tides and waves has a dependence on the number of orbits that are averaged for each solar local time. In contrast, the migrating tides are not reduced by zonal averaging. The semidiurnal tide, in particular, is reduced by employing a least squares approach with one degree of freedom if the sampling is evenly sampled in solar local time. In addition, these migrating tides are much smaller than the MDT throughout most of the vertical range (20-85 km) and latitudinal range of interest, which means the effects of the migrating tides are likely be minimal.

(3) The quality of the amplitude and phase results varies over time and latitude mainly due to dynamic solar local time sampling. Results obtained from poor solar local time sampling (large condition numbers) are less robust to small errors. The largest condition numbers occur at times during the year when the satellites are in similar orbit planes and is mostly pronounced at high latitudes.

(4) The quality of the estimates are higher when the MDT is much larger than "noise floor" created by measurement error and un-modeled geophysical effects. The phase results, in particular, are drastically affected by error sources when the MDT amplitude is small.

(5) The long term and short term variations of the MDT amplitude results for the equatorial mesosphere agree fairly well with theory and past observations. However, the observed latitudinal structure of the variations is not understood and requires future investigation.

Overall, the method has been shown to produce reasonable and accurate results when the local time sampling is good and the MDT amplitude is large. Although these conditions vary with time and are not present throughout the entire global structure, there are many cases in the near-equatorial mesosphere region where the method proves feasible and accurate in determining both the long term and short term variations of the MDT.

Bibliography

[1] D.G. Andrews, J. R. Holton, and C. B. Leovy. Middle Atmosphere Dynamics. Academic Press, Inc., Orlando, 1987.

[2] T. Aso. An Overview of the terdiurnal tide observed by polar radars and optics. Adv. Polar Upper Atmos. Res., 17, 167-176, 2003.

[3] M.D. Burrage, M.E. Hagan, W.R. Skinner, D.L. Wu, and P.B. Hays. Long term variability in the solar diurnal tide observed by HRDI and simulated by the GWSM. Geophys. Res. Lett., 22, 2641-2644, doi:10.1029/95/GL02635, 1995.

[4] L.C. Chang. Migrating Tide Variability Induced by Propagating Planetary Waves. Ph.D. thesis, University of Colorado, May 2010.

[5] L.C. Chang, S.E. Palo, and H.-L. Liu. Short term variability in the migrating diurnal tide caused by interactions with the quasi 2 day wave. *J. Geophys. Res.*, 116, doi:10.1029/2010JD014996, 2011.

[6] S. Chapman and R.S. Lindzen. Atmospheric Tides: Thermal And Gravitational. Gordon and Breach, New York, 1970.

[7] V. Deepa, et al. Tidal oscillations in the MLT region over Trivandrum (8°N, 77°E) results from SKiYMET meteor radar observations. ILWS Workshop, Goa, February 19-24, 2006.

[8] J.M. Forbes. Tidal and Planetary Waves. The Upper Mesosphere and Lower Thermosphere: A Review of Experiment and Theory. Geophysical Monograph 87, 1995.

[9] J.M. Forbes and M. E. Hagan. Diurnal propagating tide in the presence of mean winds and dissipation: A numerical investigation, Planet. Space Sci., 36, 579–590, 1988.

[10] J.M. Forbes, M. Kilpatrick, D. Fritts, A.H. Manson, and R.A. Vincent. Zonal mean and tidal dynamics from space: an empirical examination of aliasing and sampling issues. Ann. Geophysicae, 15, 1158-1164, 1997.

[11] J. S. Friedman, X. Zhang, X. Chu, J. M. Forbes. Longitude variations of the solar semidiurnal tides in the mesosphere and lower thermosphere at low latitudes observed from ground and space. J. Geophys. Res., 114, doi:10.1029/2009JD011763, 2009.

[12] GWSM: Global Scale Wave Model. National Center for Atmospheric Research, http://www.hao.ucar.edu/modeling/gswm/gswm.html.

[13] M.E. Hagan, M.D. Burrage, J.M. Forbes, J. Hackney, W.J. Randel, and X. Zhang. QBO effects on the diurnal tide in the upper atmosphere. Earth, Planets and Space, 51, 571–578, 1999.

[14] M.E. Hagan, J. M. Forbes, and F. Vial. A numerical investigation of the propagation of the quasi 2-day wave into the lower thermosphere, J. Geophys. Res., 98, 23,193-23,205, 1993.

[15] M.E. Hagan, J.M. Forbes, and F. Vial. On modeling migrating solar tides, Geophys. Res. Lett., 22, 893–896, doi:10.1029/95GL00783, 1995.

[16] M.E. Hagan and J.M. Forbes. Migrating and nonmigrating tides in the middle and upper atmosphere excited by tropospheric latent heat release. J. Geophys. Res., 4754, doi:10.1029/2001JD001236, 2002.

[17] P.B. Hays, et al. Observations of the diurnal tide from space. J. Atmos. Sci., 51, 3077-3093, 1994.

[18] J.R. Holton. The Dynamic Meteorology of the Stratosphere and Mesosphere, vol. 15 of Meteorlogical Monographs, American Meteorlogical Society, Boston MA, 1975.

[19] F.T. Huang, R. D. McPeters, P. K. Bhartia, H. G. Mayr, S. M. Frith, J. M. Russell III, and M. G. Mlynczak. Temperature diurnal variations (migrating tides) in the stratosphere and lower mesosphere based on measurements from SABER on TIMED. J. Geophys. Res., 115, doi:10.1029/2009JD013698, 2010.

[20] R.S. Lieberman, D. M. Riggin, D. A. Ortland, S. W. Nesbitt, and R. A. Vincent. Variability of mesospheric diurnal tides and tropospheric diurnal heating during 1997–1998. J. Geophys. Res., 112, doi:10.1029/2007JD008578, 2007.

[21] R.S. Lindzen and D. Blake. Lamb waves in the presence of realistic distributions of temperature and dissipation, J. Geophys. Res., 77, 2166-2176, 1972.

[22] N.J. Livesey and W. Van Snyder. EOS MLS Retrieval Processes Algorithm Theoretical Basis. Jet Propulsion Laboratory, July 2004. Retrieved from http://mls.jpl.nasa.gov/data/eos_algorithm_atbd.pdf.

[23] N.J. Livesey, et al. Version 3.3 Level 2 data quality and description document. Jet Propulsion Laboratory, January 2011. Retrieved from http://mls.jpl.nasa.gov/data/v3-3_data_quality_document.pdf.

[24] Y. Jiang. EOS MLS Level 3 Algorithm Theoretical Basis. Jet Propulsion Laboratory, June 2004. Retrieved from http://mls.jpl.nasa.gov/data/eos_l3_atbd.pdf.

[25] A.J. McDonald, R.E. Hibbins, and M.J. Jarvis. Properties of the quasi 16 day wave derived from EOS MLS observations. J. Geophys. Res., 116, doi:10.1029/2010JD014719, 2010.

[26] C. McLandress. Interannual variations of the diurnal tide in the mesosphere induced by a zonal mean wind oscillation in the tropics. Geophys. Res. Lett., 29, 1305, doi:10.1029/2001GL014551, 2002.

[27] H.G. Mayr and J.G. Mengel. Interannual variations of the diurnal tide in the mesosphere generated by the quasi-biennial oscillation. J. Geophys. Res., 110, doi:10.1029/2004JD005055, 2005.

[28] M.G. Mlynczak, B. T. Marshall, F. J. Martin-Torres, J. M. Russell III, R. E. Thompson, E. E. Remsberg, and L. L. Gordley. Sounding of the Atmosphere using Broadband Emission Radiometry observations of daytime mesospheric O2(1D) 1.27 mm emission and derivation of ozone, atomic oxygen, and solar and chemical energy deposition rates. J. Geophys. Res., 112, doi:10.1029/2006JD008355, 2006.

[29] P. Mukhtarov, D. Pancheva, and B. Andonov. Global structure and seasonal and interannual variability of the migrating diurnal tide seen in the SABER/TIMED temperatures between 20 and 120 km. J. Geophys. Res., 114, doi:10.1029/2008JA013759, 2009.

[30] J. Oberheide and O.A. Gusev. Observation of migrating and nonmigrating diurnal tides in the equatorial lower thermosphere. Geophys. Res. Lett., 29, 2167, doi:10.1029/2002GL016213, 2002.

[31] S.E. Palo. Analysis of the equatorial semiannual oscillation and quasi two-day wave in the mesosphere and lower thermosphere using a spectral model and data collected with the Christmas Island radar systems. Proquest Dissertations And Theses 1994, Ph.D. Thesis, University of Colorado at Boulder, 1994.

[32] S.E. Palo. Day-to-Day Variability of the Migrating Diurnal Tide. 37th Scientific Assembly of the Committee on Space Research (COSPAR), Montreal, Canada, July 13, 2008.

[33] D. Pancheva, et. al. Global-scale tidal variability during the PSMOS campaign of June-August 1999: Interaction with planetary waves, J. Atmos. Sol. Terr. Phys., 64, 1865-1895, doi:10.1016/S1364-6826(02)00199-2, 2002.

[34] R.J. Reed, M.J. Oard, and M. Sieminski. A comparison of observed and theoretical diurnal tidal motions between 30 and 60 km. Mon. Wea. Rev., 97, 456-459, 1969.

[35] E.E. Remsberg. Assessment of the quality of the Version 1.07 temperature-versus-pressure profiles of the middle atmosphere from TIMED/SABER. J. Geophys. Res., 113, doi:10.1029/2008JD010013, 2008.

[36] M.J. Schwartz, et al. Validation of the Aura Microwave Limb Sounder temperature and geopotential height measurements. J. Geophys. Res., 113, doi:10.1029/2007JD008783, 2008.

[37] C. Torrence and G.P. Compo. A Practical Guide to Wavelet Analysis. Bulletin of the American Meteorological Society, 79, 61-78, 1998.

[38] T. Tsuda, T., K. Ohnishi, F. Isoda, T. Nakamura, R. A. Vincent, I. M. Reid, S. W. B. Harijono, T. Sribimawati, A. Nuryanto, and H. Wiryosumarto. Coordinated radar observations of atmospheric diurnal tides in equatorial regions. Earth, Planets and Space, 51, 579–592, 1999.

[39] R.A. Vincent, T. Tsuda, and S. Kato. A comparative study of mesospheric solar tides observed at Adelaide and Kyoto. J. Geophys. Res., 93, 699-70, 1988.

[40] J.W. Waters, et al. An Overview of the EOS MLS Experiment. Jet Propulsion Laboratory, September 2004. Retrieved from http://mls.jpl.nasa.gov/data/eos_overview_atbd.pdf.

[41] J. Xu, A. K. Smith, W. Yuan, H.-L. Liu, Q. Wu, M. G. Mlynczak, and J. M. Russell III. Global structure and long term variations of zonal mean temperature observed by TIMED/SABER. J. Geophys. Res., 112, doi:10.1029/2007JD008546, 2007.

[42] J. Xu, A. K. Smith, H.-L. Liu, W. Yuan, Q. Wu, G. Jiang, M. G. Mlynczak, J. M. Russell III, and S. J. Franke. Seasonal and quasi-biennial variations in the migrating diurnal tide observed by Thermosphere, Ionosphere, Mesosphere, Energetics and Dynamics (TIMED). J. Geophys. Res., 114, doi:10.1029/2008JD011298, 2009.

[43] X. Zhang, J.M. Forbes, M.E. Hagan, J.M. Russell III, S.E. Palo, C.J. Mertens, and M.G. Mlynczak. Monthly tidal temperatures 20-120 km from TIMED/SABER. J. Geophys. Res., 111, doi:10.1029/2005JA011504, 2006.

Appendix A

NOMENCLATURE

u is eastward velocity
v is northward velocity
w is upward velocity
Φ is geopotential
N^2 is buoyancy frequency squared
Ω is earth's angular velocity
z is altitude
λ is longitude
θ is latitude
κ is R/c_p
J is heating per unit mass
a is earth's radius
g is acceleration due to gravity
H is constant scale height
t is time

D/Dt is the total derivative = $\frac{\partial}{\partial t} + u\frac{\partial}{\partial x} + v\frac{\partial}{\partial y} + w\frac{\partial}{\partial z}$

Appendix B

ADDITIONAL FIGURES

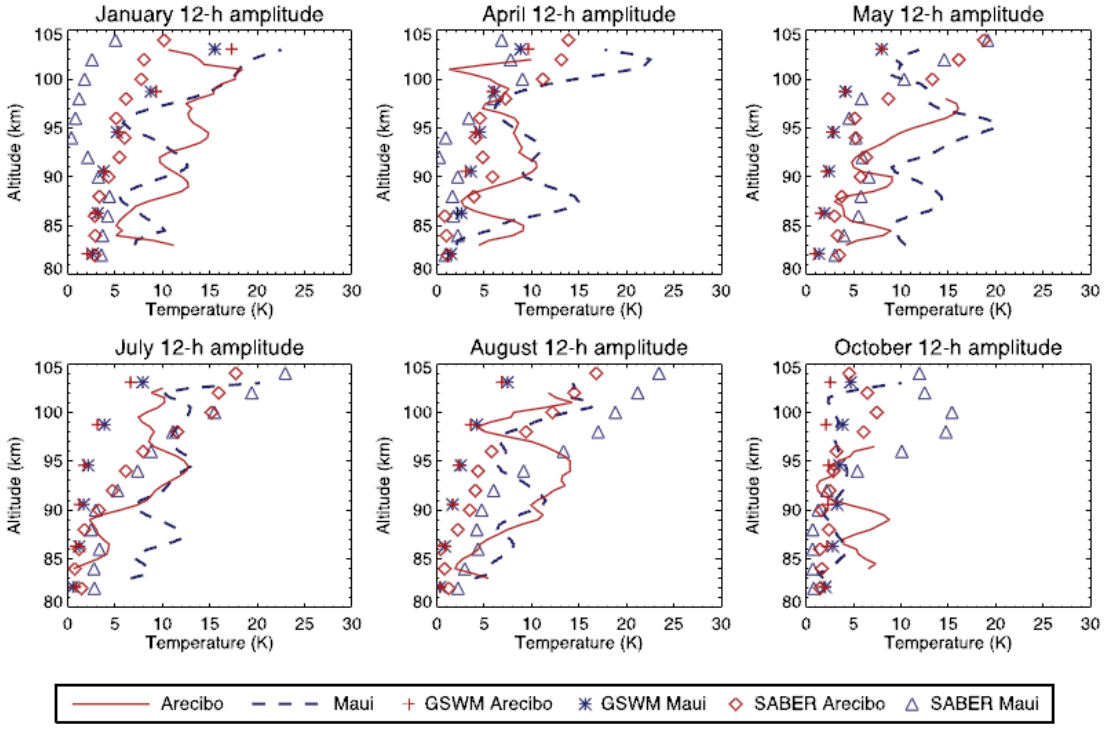

Figure B.1: Semidiurnal tide results from *Friedman et al.* [2007]. The semidiurnal amplitudes are displayed as function of altitude between 80 and 105 km for each month. Results were derived data from 2002 and 2007. Temperatures were measured from several ground-based and space-based instruments.

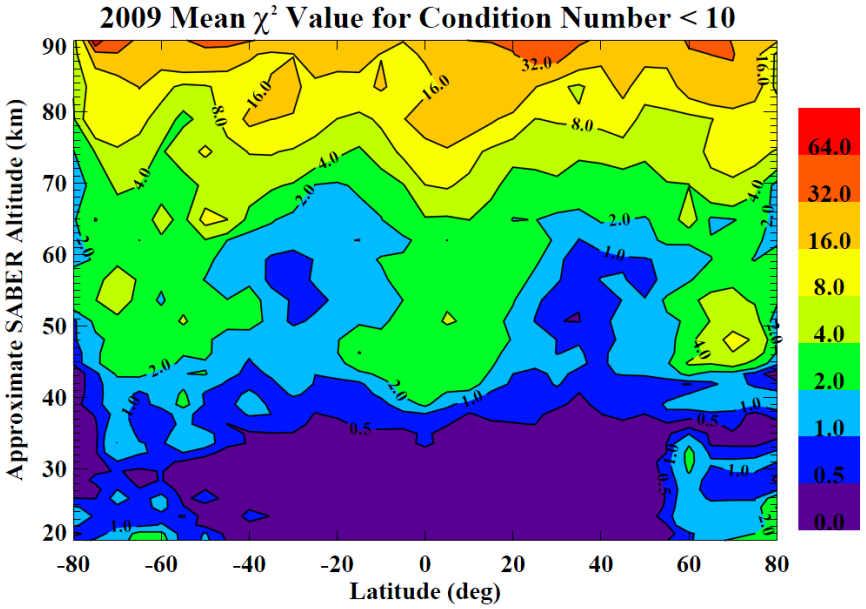

Figure B.2: 2009 mean chi-square value for condition number < 10. Instrument biases have been removed.

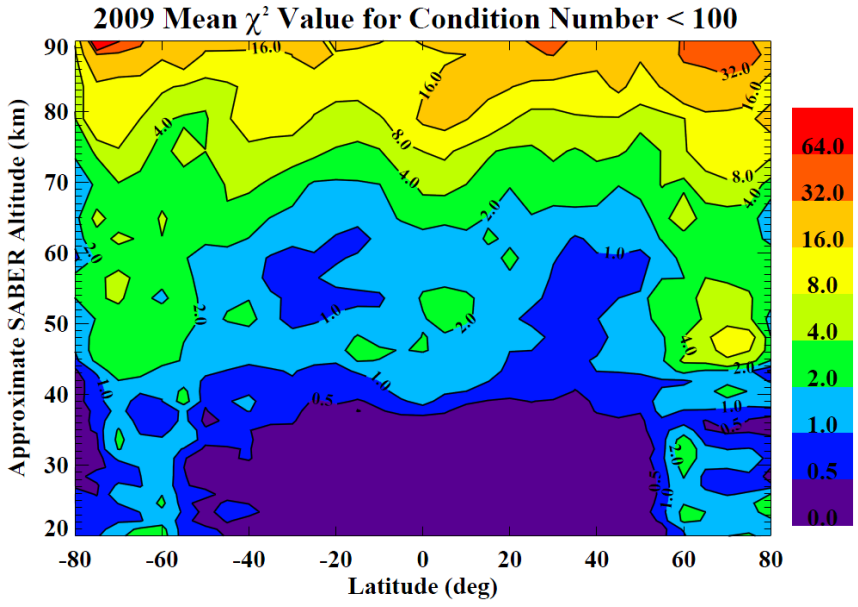

Figure B.3: 2009 mean chi-square value for condition number < 100. Instrument biases have been removed

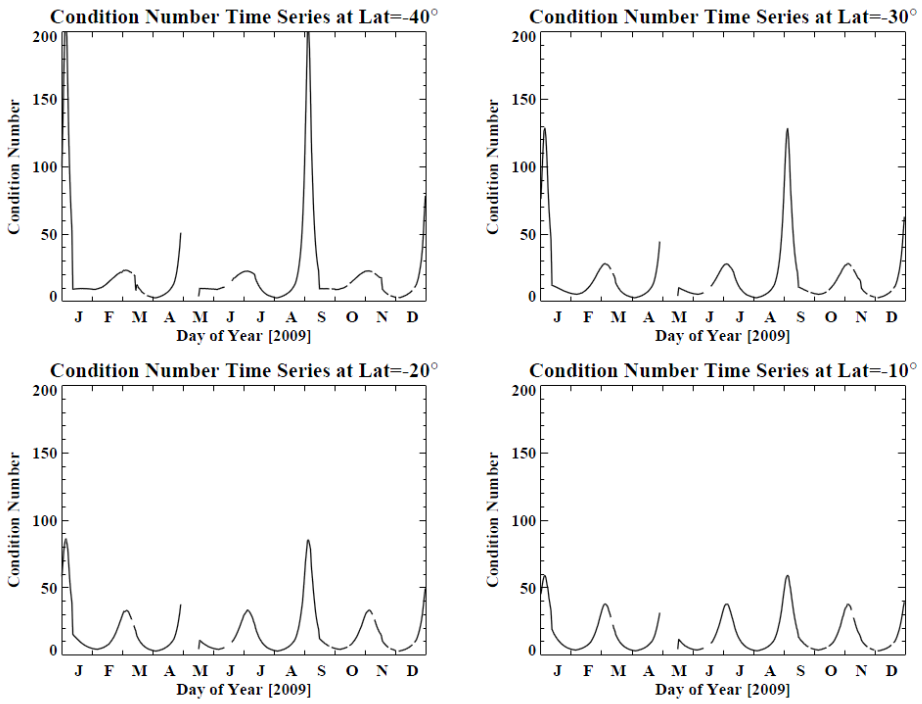

Figure B.4: Condition number time series for latitudes between -40° and -10°.

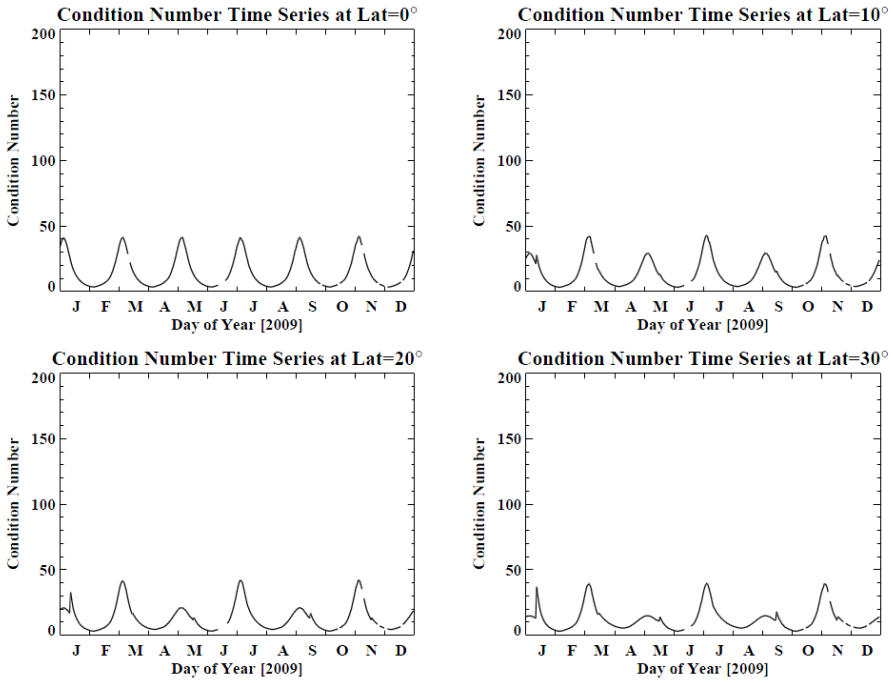

Figure B.5: Condition number time series for latitudes between 0° and 30°.

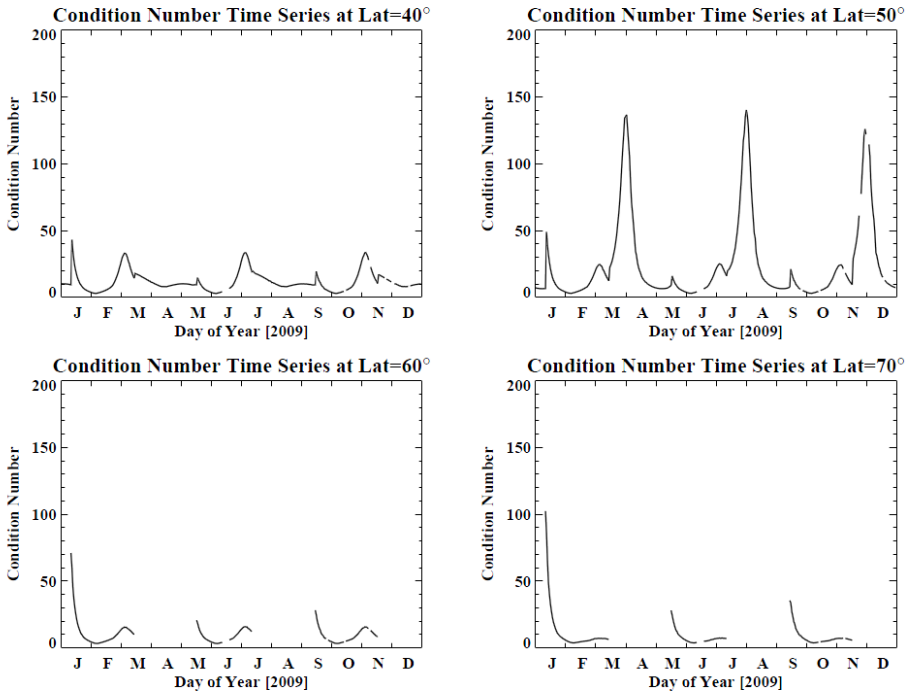

Figure B.6: Condition number time series for latitudes between 40° and 70°.

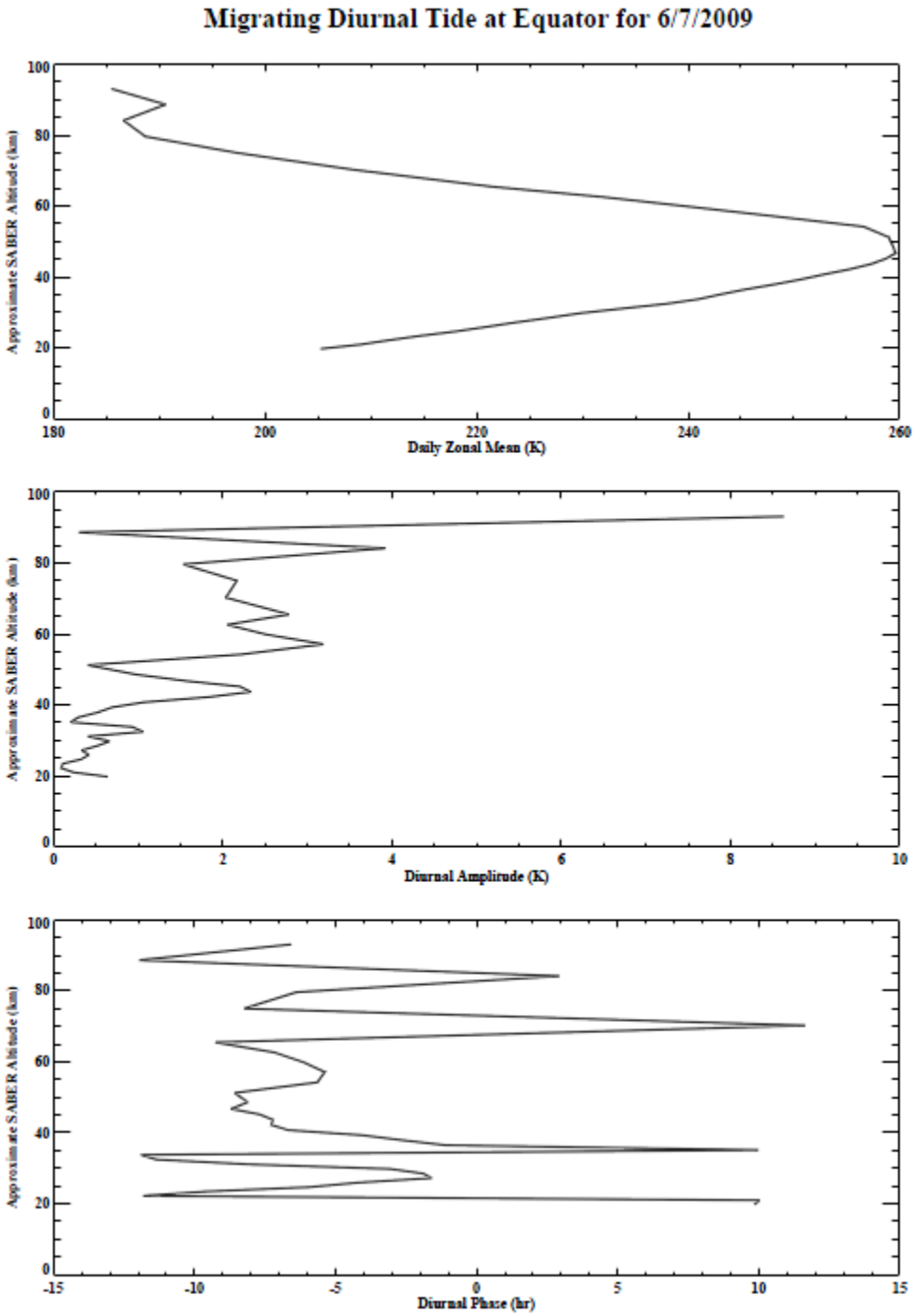

Figure B.7: Daily zonal mean and MDT estimates at the equator for 6/7/2009. The results are displayed as a function of altitude.

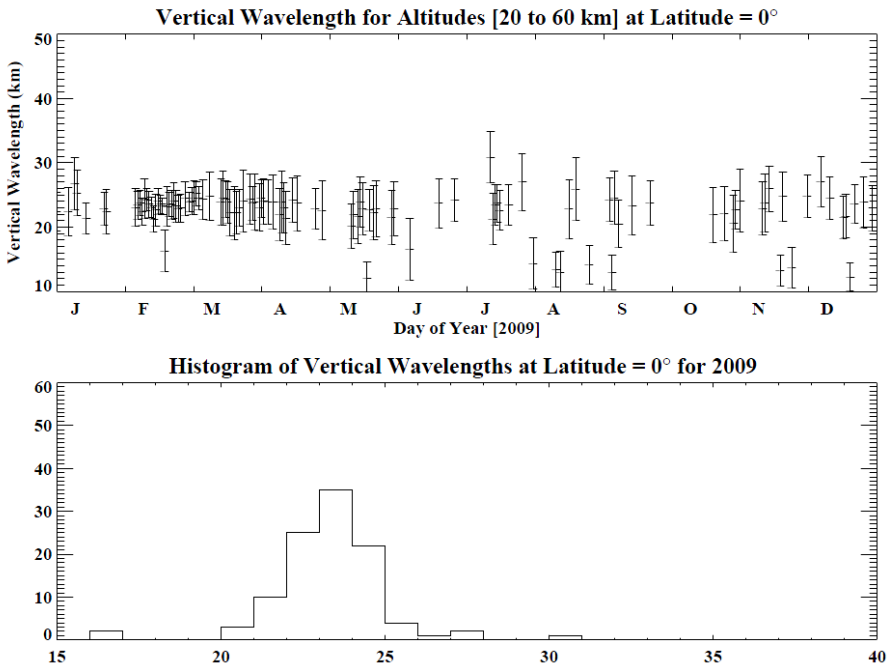

Figure B.8: Vertical wavelength estimates for 2009 at the equator using only phase results between 20 km and 60 km.

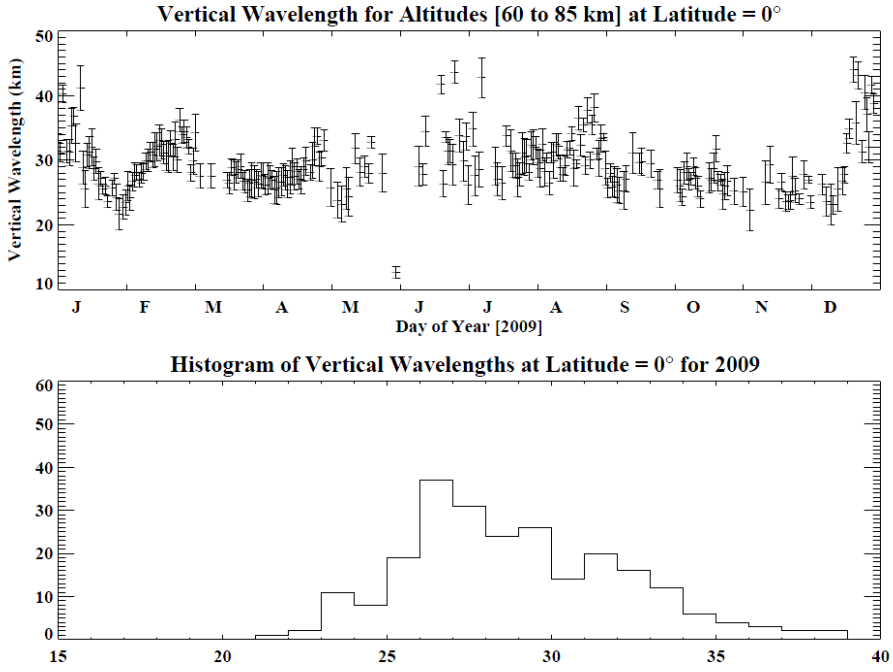

Figure B.9: Vertical wavelength estimates for 2009 at the equator using only phase results between 60 km and 85 km.

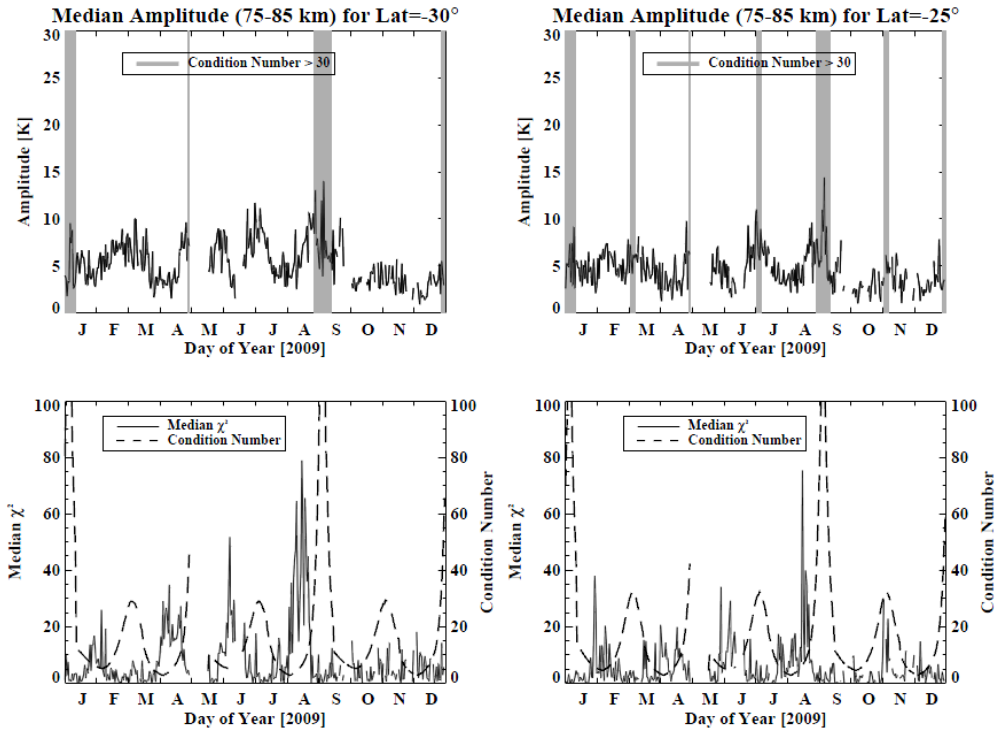

Figure B.10: 2009 median amplitude (~75-85 km) for latitudes -30° and -25°. Condition number and chi-square values are shown in the bottom plots. Shaded areas denote areas where the condition number is greater than 30.

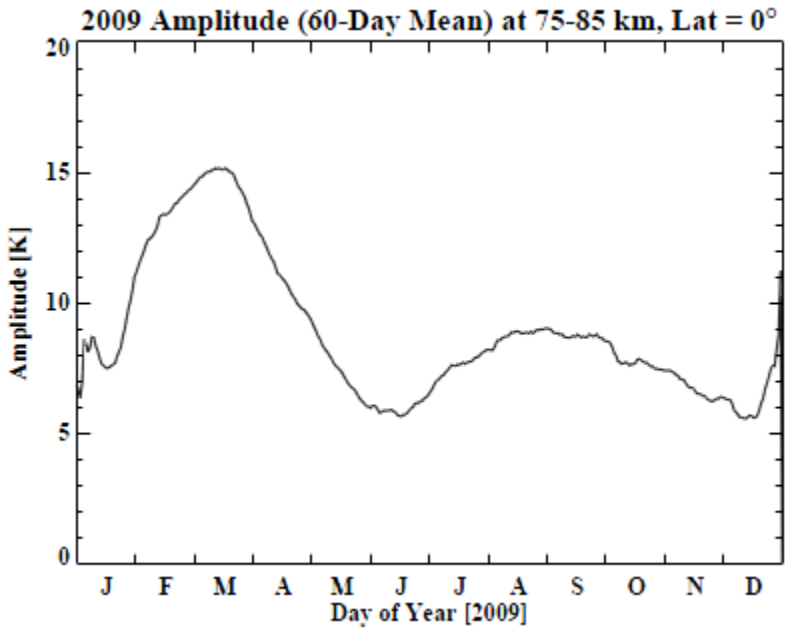

Figure B.11: 2009 amplitude (60-day mean) at ~75-85 km and equator.

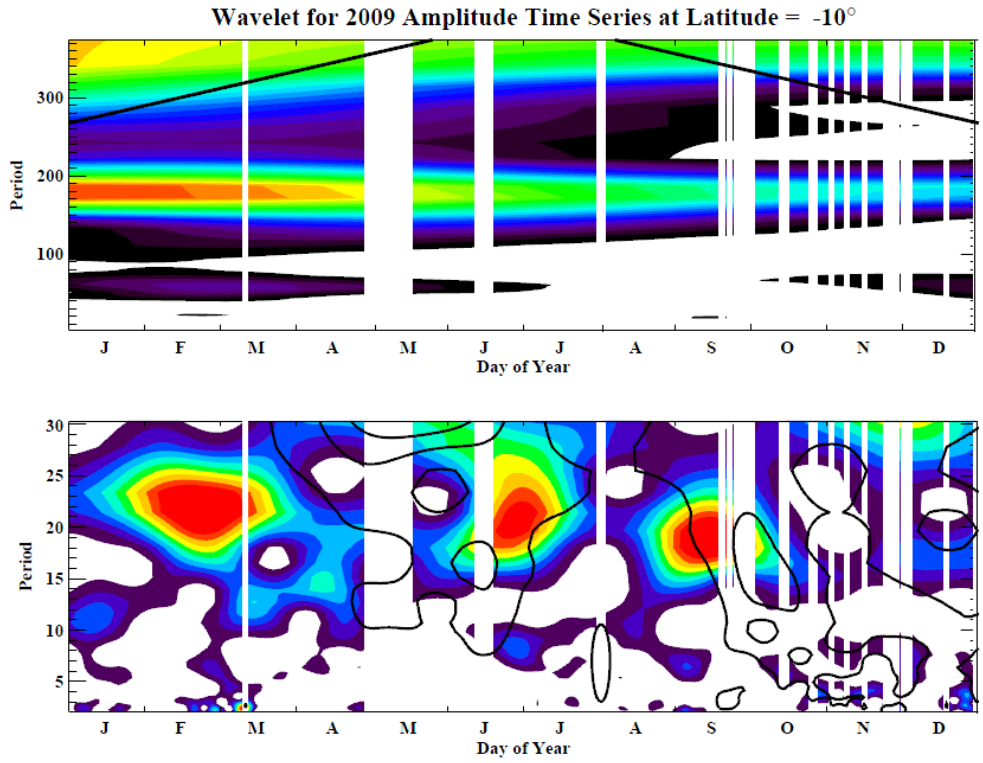

Figure B.12: Wavelet analysis on 2009 amplitude time series (-10°,~75-85 km).

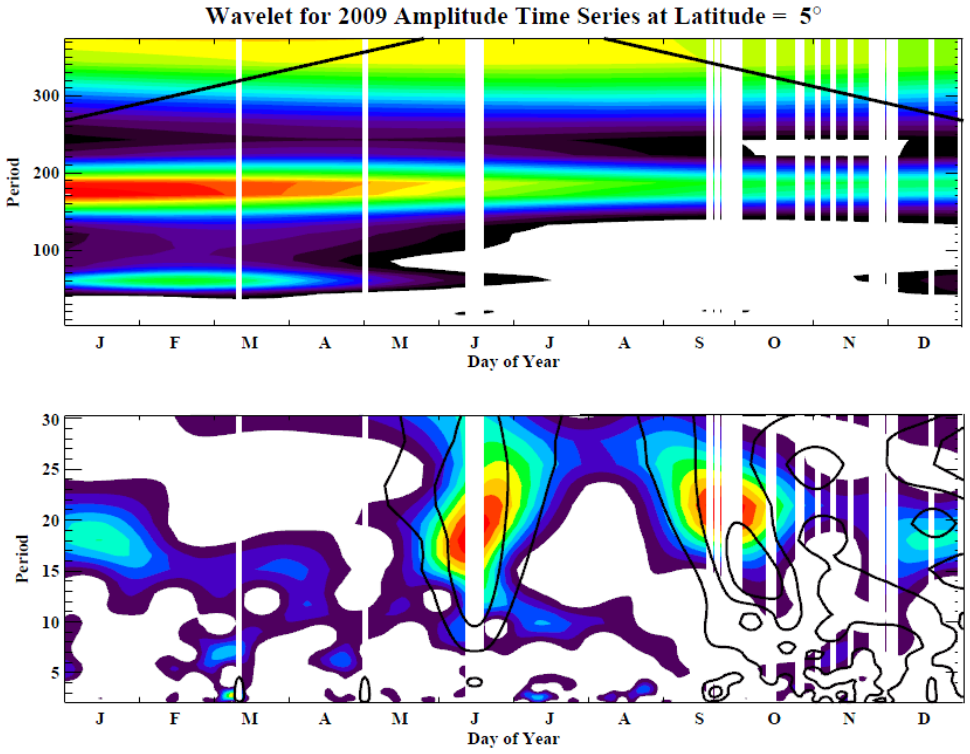

Figure B.13: Wavelet analysis on 2009 amplitude time series (5°,~75-85 km).

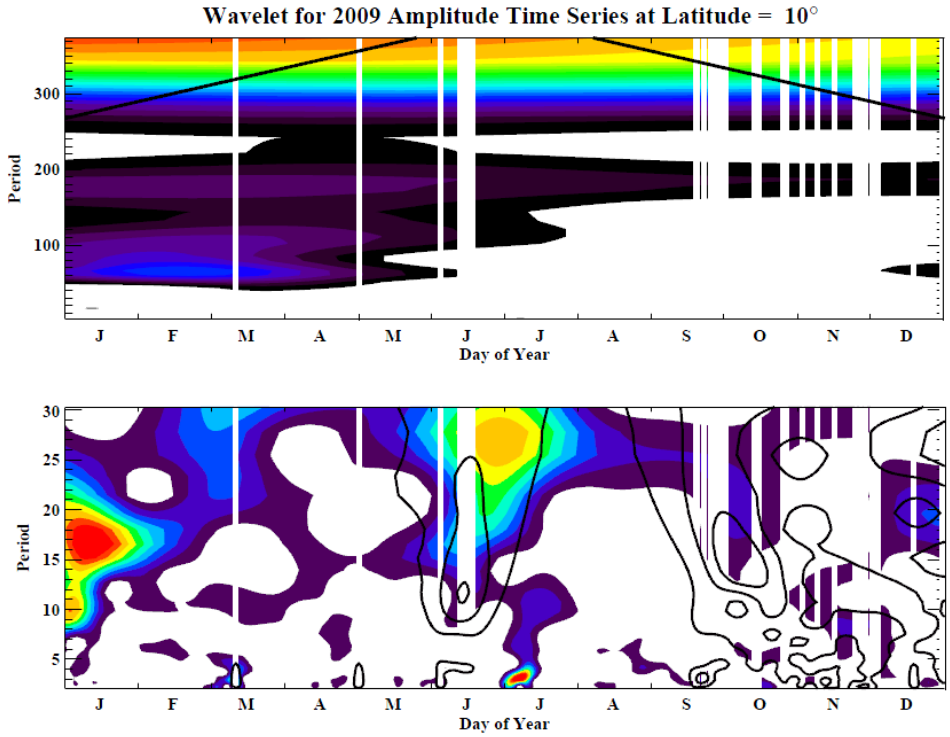

Figure B.14: Wavelet analysis on 2009 amplitude time series (10°,~75-85 km).

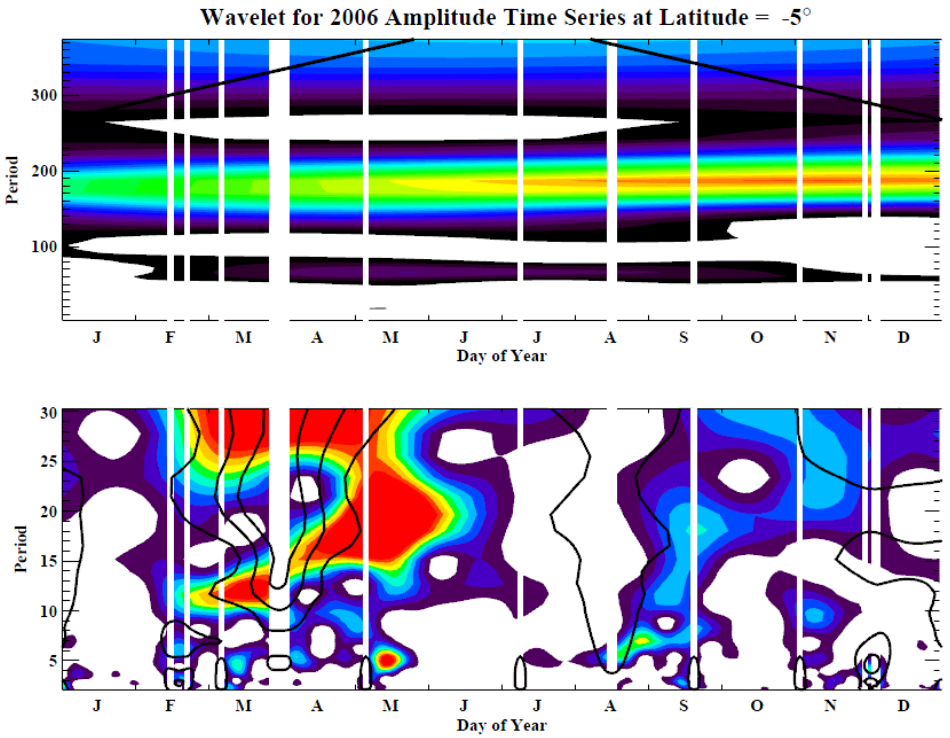

Figure B.15: Wavelet analysis on 2006 amplitude time series (-5°,~75-85 km).

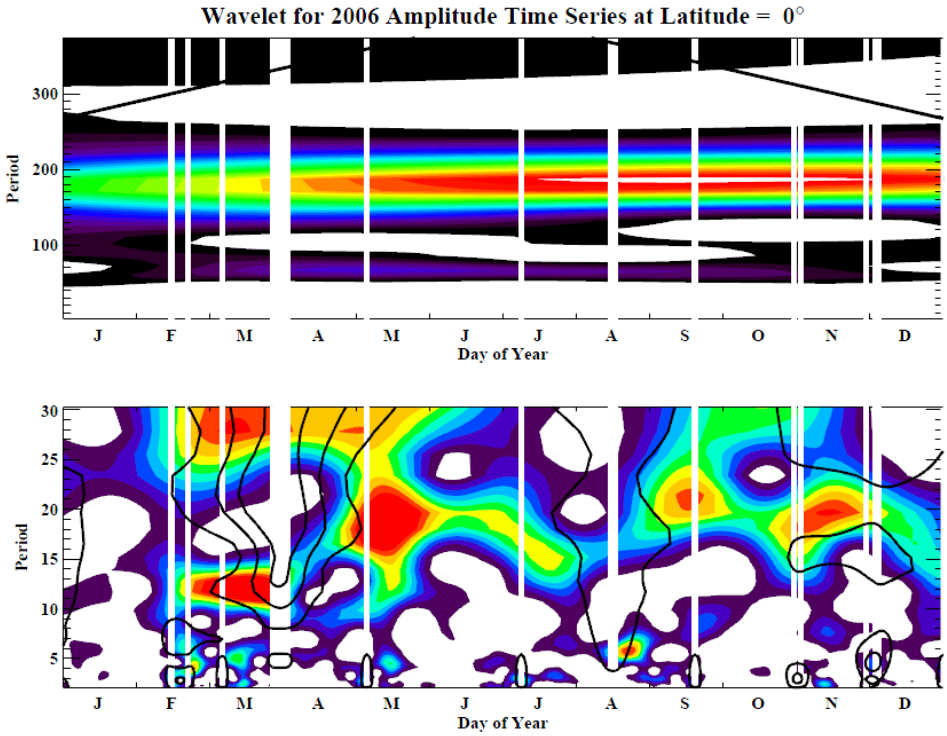

Figure B.16: Wavelet analysis on 2006 amplitude time series (0°,~75-85 km).

Appendix C

SOLUTION FOR Φ' FROM LINEARIZED GOVERNING EQUATIONS

The process for deriving the vertical structure equation and Laplace's Tidal equation is shown here. We start with the linearized governing equations, which assumes a dry, windless, isothermal, and thin atmosphere at rest and perturbation quantities are small.

$$\frac{\partial u'}{\partial t} - 2\Omega sin\theta v' + \frac{1}{acos\theta}\frac{\partial \Phi'}{\partial \lambda} = 0 \quad \text{C.1}$$

$$\frac{\partial v'}{\partial t} + 2\Omega sin\theta u' + \frac{1}{a}\frac{\partial \Phi'}{\partial \theta} = 0 \quad \text{C.2}$$

$$\frac{\partial}{\partial t}\left(\frac{\partial \Phi'}{\partial z}\right) + N^2 w' = \frac{\kappa J'}{H} \quad \text{C.3}$$

$$\frac{1}{acos\theta}\left[\frac{\partial u'}{\partial \lambda} + \frac{\partial}{\partial \theta}(v' cos\theta)\right] + \frac{1}{\rho}\frac{\partial}{\partial z}(\rho w') = 0 \quad \text{C.4}$$

Solutions are assumed to be in the form that is periodic in time and longitude. The sum of the solutions for all wave numbers (s) and frequencies (σ) comprises the perturbation quantity. The form of the solutions are shown as follows:

$$u'(t,\lambda,\theta,z) = \sum_s \sum_\sigma \hat{u}_{\sigma,s}\, e^{[i(s\lambda-\sigma t)]} \quad \text{C.5}$$

$$v'(t,\lambda,\theta,z) = \sum_s \sum_\sigma \hat{v}_{\sigma,s}\, e^{[i(s\lambda-\sigma t)]} \quad \text{C.6}$$

$$w'(t,\lambda,\theta,z) = \sum_s \sum_\sigma \hat{w}_{\sigma,s}\, e^{[i(s\lambda-\sigma t)]} \quad \text{C.7}$$

$$\Phi'(t,\lambda,\theta,z) = \sum_{s}\sum_{\sigma} \hat{\Phi}_{\sigma,s}\, e^{[i(s\lambda-\sigma t)]} \tag{C.8}$$

$$J'(t,\lambda,\theta,z) = \sum_{s}\sum_{\sigma} \hat{J}_{\sigma,s}\, e^{[i(s\lambda-\sigma t)]} \tag{C.9}$$

From this point on, we assume a given s and σ. Since the perturbation has been decomposed into an exponential portion that depends on time and longitude and a remaining portion that depends on latitude and height, the perturbation derivatives with respect to time and longitude may be expressed as:

$$\left\{\frac{\partial u'}{\partial t}, \frac{\partial v'}{\partial t}, \frac{\partial w'}{\partial t}, \frac{\partial \Phi'}{\partial t}, \frac{\partial J'}{\partial t}\right\} = -i\sigma\{u', v', w', \Phi', J'\} \tag{C.10}$$

$$\left\{\frac{\partial u'}{\partial \lambda}, \frac{\partial v'}{\partial \lambda}, \frac{\partial w'}{\partial \lambda}, \frac{\partial \Phi'}{\partial \lambda}, \frac{\partial J'}{\partial \lambda}\right\} = is\{u', v', w', \Phi', J'\} \tag{C.11}$$

The perturbation derivatives are substituted into equations C.1-C.4, resulting in C.12-C.16.

$$-i\sigma u' - fv' + \frac{is\Phi'}{a\cos\theta} = 0 \tag{C.12}$$

where $f = 2\Omega\sin\theta$

$$-i\sigma v' + fu' + \frac{1}{a}\frac{\partial \Phi'}{\partial \theta} = 0 \tag{C.13}$$

$$-i\sigma\left(\frac{\partial \Phi'}{\partial z}\right) + N^2 w' = \frac{\kappa J'}{H} \tag{C.14}$$

$$\frac{1}{a\cos\theta}\left[isu' + \frac{\partial}{\partial \theta}(v'\cos\theta)\right] + \frac{1}{\rho}\frac{\partial}{\partial z}(\rho w') = 0 \tag{C.15}$$

The variable of interest is ϕ' since geopotential is directly related to temperature through the hypsometric equation. Therefore, we want an expression that is only a function of ϕ. To achieve this, the horizontal momentum equations and thermodynamic equation are solved for u', v', and w' in terms of only ϕ.

$$u' = \frac{\sigma}{4\Omega^2 a(f^2 - sin^2\theta)}\left[\frac{s}{cos\theta} + \frac{sin\theta}{f}\frac{d}{d\theta}\right]\Phi' \quad \text{C.16}$$

$$v' = \frac{-i\sigma}{4\Omega^2 a(f^2 - sin^2\theta)}\left[\frac{stan\theta}{f} + \frac{d}{d\theta}\right]\Phi' \quad \text{C.17}$$

$$w' = \frac{1}{N^2}\left[\frac{\kappa J'}{H} + i\sigma\frac{\partial\Phi'}{\partial z}\right] \quad \text{C.18}$$

The expression for u', v' and w' are substituted into the mass continuity equation (C.4) to obtain an expression that is only a function of ϕ.

$$A + B = 0 \quad \text{C.19}$$

$$A = \frac{1}{acos\theta}\left[is\frac{\sigma}{4\Omega^2 a(f^2 - sin^2\theta)}\left[\frac{s}{cos\theta} + \frac{sin\theta}{f}\frac{d}{d\theta}\right]\Phi' + \frac{\partial}{\partial\theta}\left(\frac{-i\sigma}{4\Omega^2 a(f^2 - sin^2\theta)}\left[\frac{stan\theta}{f} + \frac{d}{d\theta}\right]\Phi' cos\theta\right)\right] \quad \text{C.20}$$

$$B = \frac{i\sigma}{N^2}\left[\frac{1}{\rho}\frac{\partial}{\partial z}\left(\rho\frac{\partial}{\partial z}\Phi'\right)\right] + \frac{1}{H\rho}\frac{\partial}{\partial z}(\rho\kappa J') \quad \text{C.21}$$

Separation of variables is now utilized. It is assumed that the remaining perturbation quantities are separable in latitude (θ) and altitude (z).

$$\Phi' = \hat{\Phi}e^{[i(s\lambda - \sigma t)]} = \left[\sum_n \Theta_n(\theta)G_n(z)\right]e^{[i(s\lambda - \sigma t)]} \quad \text{C.22}$$

$$J' = \hat{J}e^{[i(s\lambda - \sigma t)]} = \left[\sum_n \Theta_n(\theta)J_n(z)\right]e^{[i(s\lambda - \sigma t)]} \quad \text{C.23}$$

Substituting C.22 and C.23 into C.19-C.21 results in an expression that is separable in latitude and height.

$$C(\theta)G_n + D(z)\Theta_n = 0 \quad \text{C.24}$$

$$C(\theta) = \frac{1}{acos\theta}\left[is\frac{\sigma}{4\Omega^2 a(f^2 - sin^2\theta)}\left[\frac{s}{cos\theta} + \frac{sin\theta}{f}\frac{d}{d\theta}\right]\Theta_n + \frac{\partial}{\partial\theta}\left(\frac{-i\sigma}{4\Omega^2 a(f^2 - sin^2\theta)}\left[\frac{stan\theta}{f} + \frac{d}{d\theta}\right]\Theta_n cos\theta\right)\right] \quad \text{C.25}$$

$$D(z) = \frac{i\sigma}{N^2}\left[\frac{1}{\rho}\frac{\partial}{\partial z}\left(\rho\frac{\partial}{\partial z}G_n\right)\right] + \frac{1}{H\rho}\frac{\partial}{\partial z}(\rho\kappa J_n) \quad \text{C.26}$$

A separation constant containing a constant h_n is now introduced. By separating the expression into latitude and height, the exponential terms containing longitude and time are canceled out.

$$\frac{\Theta_n}{C(\theta)} = \frac{G_n}{D(z)} = constant = \frac{-i\sigma}{gh_n} \quad \text{C.27}$$

The final expressions for the vertical structure equation (C.28) for altitude and Laplace's tidal equation (C.29) for latitude are obtained after a couple variable manipulations. The vertical structure equation (C.28) is written in terms of the density weighted function of G(z) (G'(z)) and a reduced height, x.

$$\frac{d^2G'_n}{dx^2} + \left[\frac{\kappa H}{h_n} - \frac{1}{4}\right]G'_n = -\frac{\rho^{-1/2}}{i\sigma N}\frac{d}{dx}(\rho J_n) \quad \text{C.28}$$

$$\frac{d}{d\mu}\left[\frac{(1-\mu^2}{(f^2-\mu^2)}\frac{d\Theta_n}{d\mu}\right] - \frac{1}{f^2-\mu^2}\left[-\frac{s}{f}\frac{(f^2+\mu^2)}{(f^2-\mu^2)} + \frac{s^2}{1-\mu^2}\right]\Theta_n + \epsilon\Theta_n \quad \text{C.29}$$

$$= 0$$

where $G = \frac{G_n\rho^{1/2}}{N}$, $x = \frac{z}{H}$, $f = 2\Omega sin\theta$, $\mu = sin\theta$

These equations can now be solved for $G_n'(z)$ and $\Theta_n(\theta)$ by applying the appropriate boundary conditions.